Adaptive Pitch Composite Blades
for Axial-Flow Marine Hydrokinetic Turbines

Ramona Brockman Barber

A dissertation
submitted in partial fulfillment of the
requirements for the degree of

Doctor of Philosophy

University of Washington

2017

Reading Committee:

Michael Motley, Chair

Alberto Aliseda

Brian Polagye

Richard Wiebe

Program Authorized to Offer Degree:
Department of Civil and Environmental Engineering

University of Washington

Abstract

Adaptive Pitch Composite Blades
for Axial-Flow Marine Hydrokinetic Turbines

Ramona Brockman Barber

Chair of the Supervisory Committee:
Assistant Professor Michael Motley
Department of Civil and Environmental Engineering

Marine hydrokinetic (MHK) turbines are quickly becoming a viable and valuable method of generating renewable energy from ocean, tidal, and river currents. Modern MHK turbine blades are typically constructed from fiber reinforced polymer (FRP) composites, which provide superior strength- and stiffness-to-weight ratios and improved fatigue and corrosion resistance compared to traditional metallic alloys. Furthermore, it is possible to hydroelastically tailor the design of an FRP composite blade by manipulating the anisotropic nature of the material, creating a load-dependent adaptive pitch mechanism. With this strategy, the blade geometry is able to passively adjust to the instantaneous inflow, and system performance can be modified over the expected range of operating conditions. Adaptive blade designs have demonstrated the potential to increase performance, reduce hydrodynamic instabilities, and improve structural integrity in aerospace and other marine applications; however, previous research specific to adaptive MHK turbine blades has been preliminary. Further work is needed to better understand and model the behavior of these systems. To that end, the research presented here combines numerical and experimental modeling to develop greater insight into the potential benefits to be gained by the use of adaptive pitch MHK turbine blades.

In this work, a well-validated boundary element method-finite element method solver is used to develop a numerical strategy for predicting the performance and structural response of adaptive turbine blades under a wide range of site-specific operating conditions. The behavior of adaptive MHK turbine blades under normal as well as cavitating conditions is analyzed; results suggest numerous advantages possible with the use of adaptive pitch blades. Following the numerical study, an experimental program is outlined in which a flume-scale turbine system is tested under steady and fluctuating inflow conditions. Loading and performance trends found in the experimental study agree well with numerical predictions. Finally, numerical and experimental results are synthesized into a complete analysis of the potential benefits to be gained with the use of adaptive blades in MHK turbine systems. Future research directions are identified with the goal of further evolving adaptive blade technology.

TABLE OF CONTENTS

LIST OF FIGURES

LIST OF TABLES

ACKNOWLEDGMENTS

DEDICATION

To my parents, for their support
and for always encouraging my curiosity

Chapter 1

INTRODUCTION

1.1 *Motivation*

The consumption of energy around the world is growing rapidly. This has created an increased demand for renewable sources of power, which in turn has generated a driving force for technological advancement. The sun, wind, and oceans all contain vast amounts of energy, and there is a strong emerging market in sustainable methods of extracting that energy. Recently, solar and wind power technologies have been researched and thoroughly developed; however, the oceans remain a relatively untapped energy resource.

Systems that exploit the kinetic energy contained in a fluid flow to do work are not recent technology. Devices such as water wheels have been in use since they were invented in the early Hellenistic period. Hydroelectric dams are widespread around the world. However, taking advantage of the power contained in the ocean requires more complex technology. Ocean energy extraction requires systems that can survive the harsh nature of the offshore marine environment and are robust enough to avoid the need for constant maintenance. Beyond that, the deployment of such systems and the infrastructure for transmitting generated energy to the grid are both significant challenges. Recently, however, the high energy density and reliability of ocean, tidal, and river currents have garnered increased attention, especially as more nations commit to aggressive sustainable energy goals. The hydrokinetic energy resources of the earth theoretically far exceed the current global power demand, and recent studies suggest that marine currents alone have the potential to supply a significant fraction of future electricity needs [17, 23].

Tidal currents are among the most consistent and reliable of the potential energy sources contained in the ocean. While currents in the open ocean typically move at only a few

centimeters per second, when constrained by topography to a narrow channel or strait the same current gains peak velocities of 2 to 3 m/s or more [37]. Better still from the standpoint of power generation, the variability of tidal energy is predictable on average, not stochastic like that of wind, wave, or solar power. The magnitude and direction of tidal current velocities are regular and predictable to a high degree of accuracy. Thus, the kinetic energy of the tides is both extremely potent and able to deliver power predictably to a time table, which eases the integration of tidal energy into existing electricity networks [107]. Yet another advantage is that tidal turbines are similar to wind turbines in operation and design, both extracting energy from the surrounding flow. This provides the nascent technologies of the tidal energy field with decades of applicable research and experimental data to inform new studies.

Though there are many benefits to marine current energy extraction, tidal turbines face significant challenges. Blade design is a critical factor in the implementation of marine hydrokinetic (MHK) turbines, as they must withstand the large, dynamic fluid forces inherent to the maritime environment. A tidal turbine has the potential to capture more energy per year than a wind turbine of the same size due to the higher density of the surrounding flow, but this greater yield comes with an increase in drag and hydrodynamic loading [130]. Maintenance needs are considerably harder to address for underwater turbines purposefully placed in locations of extreme current, and the slender blades are potentially vulnerable to damage by marine debris [5]. An additional concern specific to marine turbines is fluid cavitation, which can cause performance decay, corrosion, vibration, and fatigue [60]. All of these obstacles underline the need for a turbine uniquely suited to its harsh environment and able to operate for long periods of time without maintenance.

Most MHK turbine blades are constructed from fiber reinforced polymer (FRP) composites. Composite materials provide excellent strength-to-weight and stiffness-to-weight ratios, improved fatigue resistance and damping properties, and can be easier to manufacture in complex shapes compared to traditional metallic alloys. Further, the anisotropic nature of these materials can be exploited by hydroelastically tailoring the design to improve performance over the expected operational life, notably in spatially varying or off-design flow conditions. This can create additional complexity in the turbine blade design problem, as

changing the material layup of the composite laminate can change the overall hydrodynamic response of the system; however, through proper design, the intrinsic bend-twist deformation coupling behavior of anisotropic composites can be utilized to develop a passive pitch adaptation, in which elastic deformations are tailored to dynamically vary with the loading condition. MHK turbines often experience highly unsteady and nonuniform inflow profiles due to boundary layer effects, free surface waves, currents, turbulence, and interaction between blades and nearby structures; the effective fluid inflow angle thus varies constantly as the blade rotates in a spatially and temporally varying flow. It can therefore be valuable to take advantage of the intrinsic bend-twist coupling behavior of anisotropic composites to passively adjust the pitch distribution of the blades in order to maintain an effective angle of attack at each blade section. These fluid-structure interaction (FSI) designs have the potential to improve system performance by increasing lifetime energy capture, reducing hydrodynamic instabilities, and improving efficiency, load shedding, cavitation behavior, fatigue life, and structural integrity.

1.2   Previous Work

1.2.1   Aerodynamics

The first research on the structural tailoring of aerodynamic systems was applied to helicopter blades and focused mainly on the reduction of vibration. As manufacturing techniques became more sophisticated and composite materials more common, groups such as Friedmann et al. [39] and Ganguli and Chopra [40, 41] studied the optimization of adaptive rotor blades in terms of performance, vibration, stability and load shedding. Ganguli and Chopra found that aeroelastic tailoring could reduce certain blade loads by up to 60% and vibrations by up to 25% while maintaining stiffness and stability [41]. Soykasap and Hodges found significant improvements in stability during both hover and forward flight using tailored composite blades [104]. Glaz et al. conducted further optimization studies on the potential for vibration reduction and found that it is possible to reduce both high- and low-speed regime vibrations, though the source of the two modes is different [42].

Helicopter rotors and wind turbines operate on similar principals, and it is not surprising

that structural tailoring of rotor blades transferred quickly from one to the other. The concept of adjusting the blade pitch of wind turbines to adapt to incident wind loading is not new; however, the idea of exploiting anisotropic or "biased fiber" materials in the blade skin to create a passive adaptive mechanism in the blades was introduced more recently. In a formative study, Karaolis et al. studied contrasting fiber layup schemes to introduce bend-twist and stretch-twist coupling into wind turbine blades [54]. From research conducted at the National Renewable Energy Lab (NREL) [70–73, 111], Lobitz et al. present successive studies in adaptive pitch blades and suggest that there is much to be gained by using aeroelastic tailoring techniques. They found that passively adaptive blades can experience reduced stresses, vibration, and fatigue loading, and in some circumstances increase energy production substantially. Lee and Flay also experimented with different material layups and concluded that the use of adaptive blades has the ability to reduce fatigue and gravity stresses [62].

Various studies have been performed on the structural aspects of composites for use in aeroelastic tailoring. In another study performed at NREL [45], Griffin examined fiber orientation and fabric architectures in composite materials to determine the strength, stiffness, fabrication costs and magnitude of bend-twist coupling. Goeij et al. also analyzed passive adaptation in composite blades, focusing on the isolation of locations of excess strain. In considering the implications on manufacturing processes, they conclude that more data is needed on the subject of fatigue of hybrid laminates with off-axis fiber orientations [33].

Most recently in the aerodynamic field, adaptive composite blades have been considered for use in large-scale offshore wind turbines. Liu and Gong studied different composite materials and layups in passive adaptation systems. They conclude that adaptive blades can increase the strength and resilience of offshore wind turbines, allowing for the design of systems with diameters greater than 100 m [68]. At the NREL, Ashwill performed studies on both material and geometric bend-twist coupling. These studies indicated that passive pitch control can be invaluable to shed the large turbulent loads experienced by long blades, lowering the cost of energy and making large-scale wind turbines more feasible [3].

1.2.2   Hydrodynamics

Significant advances have been made in the aerospace industry in the field of FSI and advanced materials. Adaptive composites have been used to improve the performance of aerodynamic lifting bodies, harvest flow kinetic energy, and dampen flow-induced vibrations. In many ways, the mechanics of a rotor operating in the marine environment are essentially equivalent to those of a rotor in the air. Thus, advances made to helicopter and wind turbine blade technology can often inform improvements to analogous marine technologies. However, many of the strategies employed for aerospace applications cannot be easily transferred to maritime applications because of the differences between the fluid properties of air and water. Marine structures experience much higher loading than those operating in air, as seawater is more than 800 times more dense than air. Viscous drag and added mass effects can also be much more significant in marine conditions. In this respect, the load-shedding attributes of passive pitch control have the potential to provide an even greater benefit to marine rotors.

Additionally, the use of adaptive blades has even more to offer to marine propellers and turbines than to their aerodynamic counterparts because of the susceptibility of hydrodynamic systems to the effects of cavitation. Every marine structure that experiences a high relative velocity to the incident flow is at risk of cavitation. In accordance with Bernoulli's principle, an increase in the velocity of a fluid will cause a decrease in hydrostatic pressure. If the fluid is in a liquid state, any decrease in pressure beyond the vapor pressure of the fluid will force the liquid to boil, forming a multitude of small bubbles. This boiling effect is called cavitation because the bubbles that form will be carried along the stream to higher pressure areas and collapse, creating a cavity in the flow that is equalized by the surrounding liquid rushing in from all sides. The flows coming from different directions meet in the center of the cavity and produce a local area of extremely high pressure. This happens on a very small scale thousands of times per second, and where the high pressure areas impact a structure such as a rotor blade they contribute to large load fluctuations, pitting, corrosion, vibration, noise, performance decay, and accelerated fatigue [24, 47, 60, 116]. Gowing et al. conducted preliminary studies which indicated that the use of bend-twist coupled composite

material could reduce cavitation on hydrofoils [43].

The higher fluid loading, complex FSI response, spatially and temporally varying inflow, susceptibility to cavitation, and harsh sea environment present many challenges to the design of marine turbine and propeller blades. However, there are many arenas in which the exploitation of FSI effects to create passive adaptive adjustment can improve the performance and structural integrity of marine rotors.

Marine Propellers

In marine and ocean engineering, investigations into passive pitch adjustment have until recently focused mostly on propulsion systems. Lee and Lin conducted a series of investigations into the design and optimization of composite marine propellers. They found that flexible composite propellers could be tailored to be more efficient over a wider range of speeds when compared to traditional metallic alloy blades [65–67]. Young et al. also conducted numerous numerical and experimental studies to determine the effects of composite bend-twist coupling on the performance and cavitation of marine propellers. In [120], Young and Kinnas present a numerical boundary element method code for the analysis of unsteady sheet cavitation on supercavitating and surface-piercing propellers, an extension of the solver for partially cavitating hydrofoils put forward by Kinnas and Fine in [57]. That code is further expanded and validated in [117, 118] and [126] to a boundary element method-finite element method iterating solver to include high-speed cavitating metallic propellers with small elastic deformations. In [124] and [125], Young et al. examine the effects of material anisotropy in marine propellers in steady and unsteady flow environments. The code mentioned above is expanded to include the large nonlinear elastic deformations inherent to flexible composite blades. Numerical and experimental results show that adaptive composite propellers can provide improved cavitation performance and increased energy efficiency over their rigid counterparts when operating at off-design conditions or in spatially varying flows.

Research has also been focused on the structural properties of composite blades. Though composites offer higher strength-to-weight and stiffness-to-weight ratios and reduced life-

cycle costs compared to metallic blades, composite manufacturing processes are not yet streamlined and variations in materials are common [31]. Further, there are still many unknowns in the complicated loading profile and development of material degradation due to seawater [32]. In [85, 88] and [127], Young and Motley investigate the influence of material and loading uncertainties of composites in marine environments on the hydroelastic response, safe operating envelope, shock loading, and overall reliability of composite marine propellers. Motley and Young also investigate lifetime performance and issues relating to the scaling of composite materials in [84, 86, 87]. Scaling by Mach number is determined to be the most accurate strategy for predicting stress distributions, because an equivalent material and layering scheme can be used in the model and full-scale propellers, though it does not fully capture differences due to viscous effects. Even with the uncertainties inherent to modern composites, the benefits are found to have the potential to far outweigh the drawbacks in passively adaptive blade technology. However, the extremes of the loading environment may make adaptive composites less practical for propulsion; this remains a design challenge [128].

Marine Hydrokinetic Turbines

Developments in MHK turbine design can be strongly informed by advancements in the closely related fields of wind turbines and marine propellers; however, the technologies are not directly transferable. While tidal turbines are subject to many of the same loading and operating conditions as marine propellers, the variability in blade geometry and system constraints creates differences in optimal designs and requires turbine-specific design and analysis programs. Similarly, marine turbine design can borrow heavily from the wind turbine industry, but tidal turbines cannot be analyzed in the same manner as wind turbines due to the added mass and other dynamic effects of the much denser fluid [108]. Codes designed for the analysis of MHK turbines must also be capable of predicting the presence of cavitation and modeling different stall characteristics than those of rotors operating in air [14].

In that light, there have recently been many numerical and experimental validation stud-

8

ies to determine the best techniques for modeling the performance and structural response of MHK turbines. In [13], Barltrop et al. use blade element-momentum and linear wave theories to model the effect of wave-current interactions on the bending moments at the root of MHK turbine blades. These complicated interactions are specific to marine environments and thus these studies have no precedent in the field of wind turbines. Blade element-momentum theory is also used to solve for performance by Grogan et al. [46] and Bahaj and Batten et al. [4, 15, 16]. Nicholls-Lee and Turnock research different levels of numerical intensity in computational fluid dynamics (CFD) codes to determine the balance between the computationally expensive solutions needed to capture details of the fluid behavior and faster, more optimization-oriented approaches in [95] and [97]. Full CFD codes are used by Kim et al. in [56] to determine the loading experienced in extreme operating conditions, and a finite element method (FEM) code is applied to determine structural response. In [103], Sale et al. develop and validate a methodology for the design of non-adaptive composite turbine blades also using FEM and a comprehensive structural optimization algorithm. Young et al. present an iterative boundary element method-finite element method code for modeling MHK turbine blades in [129] and [130], expanded from the code developed for modeling marine propellers mentioned previously.

In the evaluation of the performance and structural response of MHK turbines, several aspects have been isolated as target areas where improvement is necessary before commercial tidal energy can be a viable option. One of these focus points is turbulence, which was a factor in the failure of several early marine turbine pilot programs. The complex flow fields of the marine environment typically contain turbulence at a large array of length and time scales [110]. Previous studies have found that the performance, blade loads, and fatigue life of hydrokinetic turbines can depend strongly on a variety of turbulence parameters. Blackmore et al. found that both turbulence intensity and turbulent length scale can have large impacts on blade and rotor loads and turbine performance characteristics [20, 21]. Preliminary sensitivity analyses conducted by Milne et al. found that the longitudinal turbulence intensity is a dominant parameter influencing blade root fatigue and maximum loads [77]. This has lead to a push for better current resource and turbulence assessment in potential tidal energy project locations [23, 26, 102]. Equally, there has been a demand

for efficient marine turbine design that can operate in conditions of greater turbulent forces and withstand the associated increased fatigue loading [109].

Cavitation susceptibility is another limiting criterion in modern marine turbine design, as cavitation contributes to pitting, corrosion, vibration, and fatigue of marine structures [5, 112]. Additionally, the vibration caused by cavitation dramatically increases noise generation, a particular concern of turbine systems located in or near sensitive marine mammal habitats. Reducing cavitation susceptibility would allow marine turbines to operate at more efficient tip speed ratios, as the size and speed of the rotor are presently limited by the pressure reduction caused by the speed of the blade tips. Furthermore, a reduction in cavitation would allow the installation of turbine arrays in shallower waters where the ambient pressure in the fluid is lower. This would expand the number of possible sites for tidal power generation and decrease the cost of installation and implementation, as cables could be shorter and the systems would be more accessible for maintenance. In general, cavitation resistant blades would be more robust, experiencing less vibration, pitting, and fatigue loading. Additionally, a decrease in cavitation susceptibility could reduce the limits on depth, maximum rotational speed, and overall blade size that are in place for non-adaptive blades.

Recently, the design of bend-twist coupled composite blades has been proposed to increase the performance and structural integrity of MHK turbines. Tidal turbines stand to benefit from composite materials and passive pitch control mechanisms in many of the same ways as marine propellers and wind turbines. The higher stiffness- and strength-to-weight ratios of composites and their resistance to corrosion are all valuable properties to the durability of MHK turbines [78]. In [18], Beyene and Peffley investigate geometrically adaptive composite blades and find flexible turbine blades to be more efficient than standard rigid blades. Nicholls-Lee et al. develop an iterative solving process for bend-twist coupled marine turbine blades and found that they produced a higher power output over a wider range of tip speed ratios when compared to a rigid metallic blade [94, 96, 98]. However, their model produced unrealistically large blade deformations and did not consider site-specific parameters. Murray et al. have also explored the creation of a low-order methodology for the design of adaptive composite blades [89, 90].

Previous work by this author begun an examination of the capabilities of passive pitch

control of marine hydrokinetic (MHK) turbine blades under both instantaneous and long-term variable amplitude loading with consideration for practical design and operational constraints [6]. Potential performance improvements include increased power generation, reduced hydrodynamic instabilities, and improvements in efficiency, load shedding, and structural performance. It was shown that the orientation of the composite fibers in an adaptive blade could be tailored to create turbine blades that adapt in various ways to the local fluid flow. Passively controlled blades that pitch to feather were shown to decrease angle of attack and therefore energy capture when compared to a reference blade with no adaptive pitch mechanism, while blades designed to pitch to stall increased angle of attack and energy capture. From the structural analysis of the turbine blades, both passively controlled systems resulted in higher unsteady stress profiles than the reference blade model, due to the increased flexibility of the blades and the off-axis orientation of the fibers.

Practical restrictions such as maximum rotational speed or generated power imposed on these turbine systems in [6] were shown to create tradeoffs and limits on performance improvements. Those blades that increased power production were also shown to experience higher blade loads and increase the required range for active control, while blades that decreased power production were shown to experience lower blade loads and decreased active control requirements. Because of these tradeoffs, further research is necessary to fully explore the benefits and behaviors of passively adaptive blades.

Little experimental work has been accomplished thus far in the nascent field of adaptive marine turbine blades. In [18], isotropic flexible blades were tested for use on an axial turbine in an oscillating water column device. The work is specifically focused on low Reynolds number flow regimes such as could be applicable to wave, wind and tidal energy conversion systems. The study compared a rigid urethane blade to two urethane blades of increasing flexibility, all at model scale. Though the material used is isotropic, meaning it was not possible to tailor the twisting deformation of the blades, the geometry of the blades created some inherent bend-twist coupling. The results are presented as a function of Reynolds number, concluding that the flexible blades operated at a higher efficiency than the rigid blade, especially at low flow or part-load conditions. Additionally, Murray et al. have recently completed a small-scale experimental study as a verification of their low-order

design tool [91]. They found benefits to both loading and performance with a pre-twisted adaptive composite blade strategy, with higher torque at low inflow velocities and reduced power and thrust at maximum flow speed relative to a similar rigid blade.

In a more complete experimental program, [52, 105, 106] outline the testing regime of the full scale variable speed, fixed pitch horizontal axis turbine developed by the German company SCHOTTEL. The composite turbine blades are designed to be passively adaptive to reduce thrust in overspeed conditions. In [105], a towing test is presented as an intermediary step between laboratory testing and offshore installation. The experimental rig was mounted to the bow of a harbor tug, allowing control over the flow condition; however the tests were performed in still water conditions and thus cannot account for the effects of turbulence or velocity shear. The study presents power and thrust coefficients as a function of tip speed ratio for a range of inflow velocities, effectively accounting for the rate dependence of an adaptive system. Results indicate that both power and thrust coefficients are reduced at higher flow velocities. Because these velocities are above the rated speed of the system, the reduction in power coefficient in that range is beneficial. The passively adaptive blade was shown to reduce thrust by approximately 50% compared to a rigid blade design in overspeed conditions. In reference [52], the same turbine is mounted to a moored barge for a stationary test conducted over 48 days during daytime flood tides. This more closely matched real tidal conditions including turbulence and velocity shear; however the tidal regime at the test site did not exceed design flow speeds, and therefore the benefits of the passively adaptive blades were not realized. The moored and towing tests presented in [105] and [52] were compared in [106]. Though there were substantial differences in the flow conditions of each test, little impact was observed on the power output of the turbine. There was a significant disparity of the thrust observed between the two tests however, with much higher thrust measured in the moored rig test. It is suggested that this discrepancy is due to the difference in the configuration of the load cells in each case. Most significantly, the experiments show that the flow characteristics in a tidal environment contain both larger magnitude and higher frequency velocity fluctuations, emphasizing the importance of experiments conducted in realistic tidal settings.

1.3 Research Objectives

While the performance characteristics predicted for adaptive turbine blades are promising, further work is needed to fully understand and model the behavior of these systems. To that end, this research program was formed with the following objectives:

1. To develop a numerical strategy to predict the performance and structural response of adaptive composite MHK tidal turbine blades to normal and extreme site-specific loading conditions,

2. To further explore the potential of adaptive composite blades with flume-scale experimental tests under steady and turbulent inflow conditions,

3. To assess potential benefits to be gained with the use of adaptive blades in MHK turbine systems, and

4. To identify additional research areas necessary for further evolving adaptive blade technology.

The work presented here elaborates and expands on research and conclusions which have been published previously in journal contributions and conference proceedings, namely in references [7–12, 82, 83, 128].

Chapter 2

METHODOLOGY: TURBINE BLADE DESIGN

Numerous factors go into the design of marine turbine blades. Though many considerations are equally important to any marine turbine system, there are several that are particularly relevant or unique to adaptive blade design. This chapter examines those factors in detail, include a discussion on the manner in which they are integrated into the blade model used for numerical analysis in this research, and outline the method used in this work for assessing the value of various blade designs.

2.1   Control Mechanisms

Traditional horizontal axis wind and marine hydrokinetic turbines fall into one of four main categories: fixed speed-fixed pitch, variable speed-fixed pitch, fixed speed-variable pitch, and variable speed-variable pitch. These categories correspond to different methods and levels of control that affect the performance and power generation of the turbine. Because the output of each turbine is necessarily limited to the rated (maximum) power or torque of the attached generator, some sort of control scheme is generally desirable in order to reduce the load on blades and generator in extreme operating conditions. Controls are also used for various other reasons, including the prevention of cavitation along the blades and, in some locations, minimizing interaction with sensitive marine mammal species.

A discussion of control requires working knowledge of the terminology involved. The angle of attack of a hydrofoil, α, is the angle between the chord line, a line running from the leading edge to the trailing edge of the foil, and the relative fluid velocity. The angle of attack at a point r along the blade radius, $\alpha(r)$, is a function of the blade pitch, $\phi(r)$, and the effective fluid inflow as pictured in Figure 2.1.
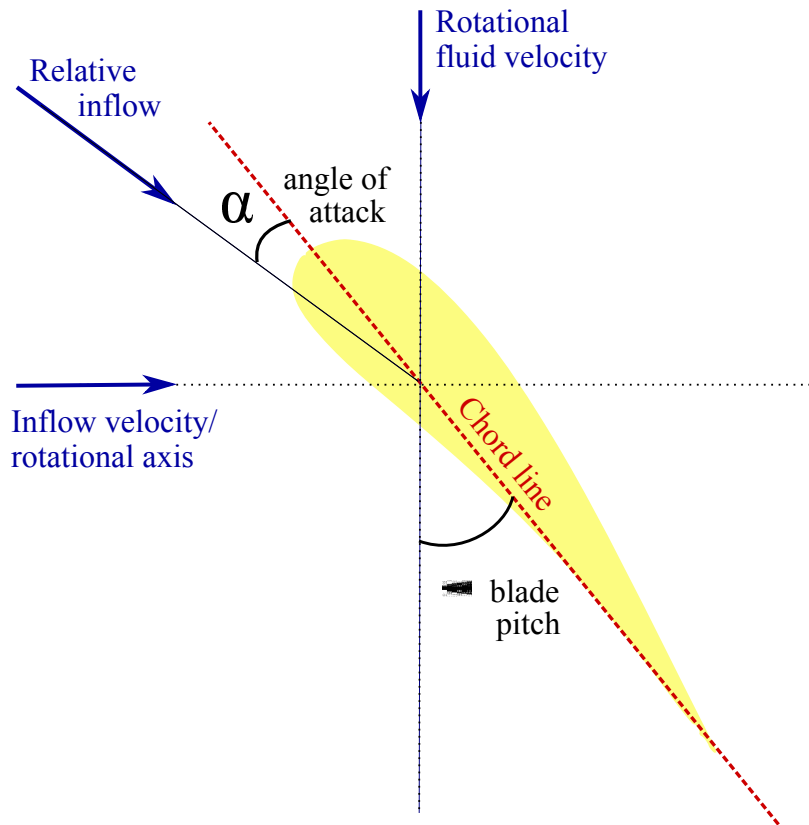
Figure 2.1: Relative angles $\alpha\left(r\right)$, $\phi\left(r\right)$, and $\beta\left(r\right)$.

2.1.1 Active Control

Active control generally falls into two categories: active pitch control, in which mechanical actuators in the hub of each turbine blade adjust the blade pitch for the flow conditions, and active speed control, in which generator torque on the turbine shaft is regulated to manage rotational speed. Active control used to vary the pitch of the blades is generally enforced by adjusting the angle of attack of each blade relative to the fluid inflow. This strategy can be used to decrease generated lift above rated power, therefore slowing the rotation of the turbine, often referred to as an aerodynamic or hydrodynamic braking system. In extreme circumstances, the turbine can be stopped by adjusting the blades such that the leading edge of each blade points directly into the oncoming flow and no lift is generated. On the other hand, controlling the speed of the turbine rotation uses opposite means to

achieve the same effect. These variable speed turbines apply generator torque to the rotor shaft in order to regulate the tip speed ratio. Above rated power, variable speed control can effectively increase the angle of attack and cause the flow over the blades to stall. Fluid stall occurs when the angle of attack of the blade becomes too large and the flow over the blade detaches from the top of the foil and forms turbulent eddies, and creates a reduction in generated lift which further reduces rotor speed. Stall-controlled turbines are difficult to stop completely without imposing extreme loads on the generator, and forcing fluid stall increases the hydrodynamic loading on the blades significantly [113]. However, variable speed turbines have the benefit that a single brake mechanism in the generator is, in most cases, easier to construct and maintain than an active pitch mechanism acting in the hub of each blade. Even simpler, fixed speed-fixed pitch turbines are the easiest of the design varieties to manufacture, requiring fewest active control mechanisms. Generally, a fixed speed-fixed pitch turbine will have the ability to decouple the rotating shaft from the generator driver, allowing the turbine to spin freely in overload conditions to avoid damage to the generator; however, this can result in extremely large blade loads at high velocities. On the opposite end of the spectrum, variable speed-variable pitch systems are the most complex to design, containing both mechanical and aero- or hydrodynamic braking systems, but have the ability to reduce blade loading significantly, optimize performance, or maintain rated power over a range of inflow velocities.

On average, variable speed-variable pitch turbines have the potential to generate the most power; however the associated higher initial costs and higher maintenance needs required by the active control systems can result in a higher cost per unit of electricity generated compared to simpler system designs [115]. Relative to wind turbines, active control mechanisms in MHK devices can be more costly and more difficult to control effectively. Most of the proportionally larger cost lies in the challenges of designing mechanisms for and conducting maintenance in the submarine environment. The difficulty in efficient control is due to lower maximum pitching rates and the fact that the active systems cannot react instantaneously to changes in the inflow [114].

16

2.1.2 Passive Control

In contrast to active control mechanisms, passively controlled rotor blades are able to rapidly adjust to changing flow conditions. This creates the possibility of specifically designing blade geometries that will alter system performance by way of load-dependent deformations. Passive adaptation does not require an active driver to change the blade pitch but instead creates a nearly instantaneous structural response that is difficult to achieve with an active mechanism because of the high flow variation and excitation frequencies in water. One method of passive control exploits the coupled bend-twist characteristics of composite materials. In general terms, the anisotropic nature of the composite fibers in the blade define a material strong axis that can be rotationally offset from the longitudinal axis of the blade by a specified amount. In effect, this creates a load-dependent deformation mechanism in which an applied shear load, for example, will result in twisting as well as bending deformations even in the absence of a torsional load.

The adaptive pitch mechanism is created via careful design of fiber reinforced polymer (FRP) composite material. FRP composites are typically manufactured as layers of sheets of directional fibers embedded within a resin matrix. The layers are known as lamina, which taken together comprise the overall composite laminate. The strength and stiffness of the fibers give FRP composites superior structural strength and stiffness properties compared to metallic alloys, while the resin matrix allows for stress transfer between the individual fibers as well as between laminate layers. Because carbon fibers especially have an effectively zero coefficient of thermal expansion and a high resistance to corrosion, the are well-suited to applications in harsh marine environments.

Structurally, each carbon FRP composite lamina is inherently orthotropic, as the carbon fibers are aligned unidirectionally within a lamina; however, due to the endless possible configurations, the resulting laminate can be designed to have any directional properties. Quasi-isotropic FRP laminates are especially common and are frequently used in aerospace, automotive and recreational applications. Currently, most MHK turbine blades are constructed from quasi-isotropic laminates. Other configurations, however, can be used to create a coupled structural response, where the deformations of the laminate can be cou-

pled between extension and bending, extension and twisting, or bending and twisting. In the instance of marine turbine blades, the most useful of the three possible coupled responses is bend-twist coupling, as the blades experience almost entirely transverse loading.

The degree of coupling between these responses can vary based on the relative angles of the fibers of each lamina that comprise the laminate. As a demonstration, Figure 2.2 shows the result of increasing the unidirectional fiber angles in otherwise identical bend-twist coupled composite spars loaded with equal masses. As the fiber angle is further offset from the longitudinal axis of the spar, bending stiffness is reduced while induced twist increases.

Using an anisotropic composite laminate as described above, it is possible to exploit the bend-twist coupled behavior of a tailored composite to create an adaptive pitch mechanism that provides a load control strategy for the turbine system. Thus, when a turbine blade is loaded transversely by the fluid flow incident to the system and starts to bend out of the plane of rotation, that bending deformation can be coupled with a twisting deformation that will change the pitch angle along the span of the blade. Because the magnitude of the deformation is load-dependent, it is possible to design a blade that will adapt to changing flow conditions via a nearly instantaneous structural response.

There are two strategies to passive pitch control: a blade can be designed to either capture excess loads from the fluctuating fluid flow in order to generate additional power with a pitch to stall mechanism, or to shed load increases with a pitch to feather design, minimizing fatigue and failure potential while maintaining a steady power output. An adaptive turbine blade can be designed to pitch to feather (decreased angle of attack) or pitch to stall (increased angle of attack), depending on composite laminate layup sequence. It is important to note that though the blades designed to increase angle of attack are termed "pitch to stall", they do not necessarily experience fluid stall in normal operation due to the load-dependent nature of the deformation. The name refers to the fact that an increased angle of attack pitches an airfoil *towards* stall. Because the inflow angle is constant for a given operating speed, in order to decrease the angle of attack a pitch to feather blade must increase the pitch angle of the blade, while a pitch to stall blade will increase the angle of attack by decreasing the pitch angle of the blade. Figure 2.3 shows a schematic of the two passive geometry options.

18

Figure 2.2: Bend-twist coupled spars of varying fiber angle under equal load.

(a) The passively adaptive bend-twist response   (b) Pitch to feather vs. pitch to stall
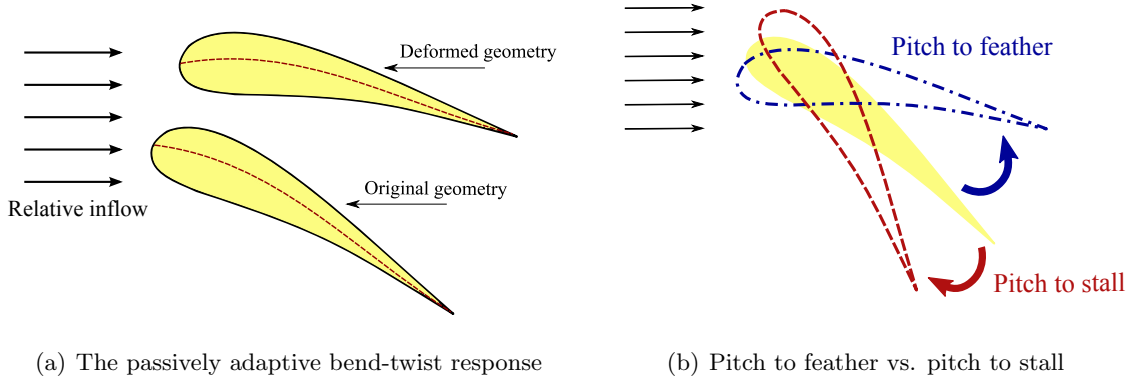
Figure 2.3: A schematic of passive pitch deformation.

2.2 System Assessment

In order to have a meaningful conversation about the performance and structural response of adaptive blades, metrics for assessment must be determined. Typically, marine turbine performance is characterized by two main parameters: the coefficients of power and thrust. The power coefficient, C_P, is a non-dimensional ratio of the power (P) extracted by the turbine to the total kinetic energy flux available to the rotor. Similarly, the thrust coefficient, C_T, represents the thrust (T) on the rotor normalized by the axial momentum flux available to the rotor. The coefficients are defined as follows:

$$C_P = \frac{P}{\frac{1}{2}\rho U^3 A_T} \tag{2.1}$$

$$C_T = \frac{T}{\frac{1}{2}\rho U^2 A_T} \tag{2.2}$$

where ρ is the fluid density and A_T the swept area of the turbine. These two quantities give a relative picture of the expected power generation of the system and the amount of loading it sees. Thus, relatively higher values of C_P and lower values of C_T are ideal.

In most studies, the turbine rotor is assumed to be rigid and attention is focused on the above performance characteristics and details of the wake. No body is entirely rigid, however, and stress and strain deformations affect performance as well as determine the fatigue behavior and ultimate failure of the system. This is especially true for adaptive turbine blades, as the structure and material are designed to interact with the flow and affect performance; additionally, the load-dependent deformations can create higher stresses in the body than those found in non-adaptive blades [82]. Thus, beyond power and thrust coefficients it is important to fully examine the stresses and strains in the system. This is especially relevant as many previous numerical studies of marine turbine blades have predicted unusually large deformations without showing the accompanying stress profiles that would demonstrate sufficient structural robustness [46, 53, 93, 94].

It is not adequate to solely examine the performance and structural response of adaptive turbine blades, however. The work presented here is generally interested in relative metrics, *i.e.* how the use of an adaptive material scheme might be able to improve the performance and response of a traditional marine turbine system. To facilitate that discussion, results of adaptive blade analyses are presented with results from the same analysis for a non-adaptive reference blade.

2.3   Rate Dependence

To determine performance of any hydrokinetic marine turbine, typically rotor performance parameters power (C_P) and thrust (C_T) coefficients are examined. Previously in the literature on wind and marine turbines and propellers, power and thrust coefficients have been presented as a function of tip speed ratio ($\lambda = \omega R/U$) for turbines or advance coefficient ($J = \pi/\lambda$) for propellers, where ω is the rotor angular velocity, R the radius and U the inflow velocity. Both of these parameters represent the ratio of the inflow fluid velocity to the linear tip speed of the rotor. This allows for non-dimensionality on both axes and the ability to draw comparisons between studies and experiments over different ranges of inflow velocity or rotational speed; i.e, fast moving rotors in fast flows can easily be compared to slower moving rotors in slow flows because the tip speed ratio will be similar or the same. This kind of comparison does not fully capture Reynolds number effects, which compare in-

ertial forces to viscous forces and depend on relative length, velocity, density and viscosity; however, as most full-scale rotors operate in flow regimes where lift and drag are independent of Reynolds number, it is a reasonable simplification to make for realistic operating ranges and adequately represents the dependence of these performance parameters. This valuable simplification allows a turbine or propeller blade to be optimized for performance at a single design point, significantly reducing the computational requirements of design and optimization.

The performance of adaptive rotors, on the other hand, is governed by the material and geometry design and is strongly influenced by load-dependent deformations. Thus, performance is not dependent solely on the ratio but on the magnitudes of the inflow velocity and rotational speed of the rotor and the corresponding total dimensional blade loads. As shown in Figure 2.4, if λ is changed only as a function of rotational velocity (ω, or in this case n, in rpm) with a fixed inflow velocity (U), the adaptive turbine will perform differently than if the rotational speed is held constant while the inflow velocity varies. As such, it is critical to be able to predict and consider the deformation responses over the full range of expected site-dependent, practical operating conditions to achieve an accurate prediction of turbine performance. Each turbine is operating in a unique environment with a defined inflow velocity range and limitations on rotational speed specific to the generator system of the turbine. These parameters must be taken into account in order to create a complete representation of the structural response of an adaptive blade and thus the performance of the turbine.

The potential benefits of the use of adaptive materials for passive control on MHK devices have been preliminarily explored, but practical limitations and design considerations have not been properly considered. Many of the predicted performance improvements found by using adaptive propeller blades were shown to be overstated when applied in practical design [86], as the comparisons were not made based on comparable loading conditions. While conceptual performance improvements can be shown, care must be taken to make fair comparisons based on operational requirements and constraints such as limits on the power generated or rotational speed of the turbine. Accurate comparisons between adaptive pitch turbines or propellers can only be made by analyzing performance as a function of
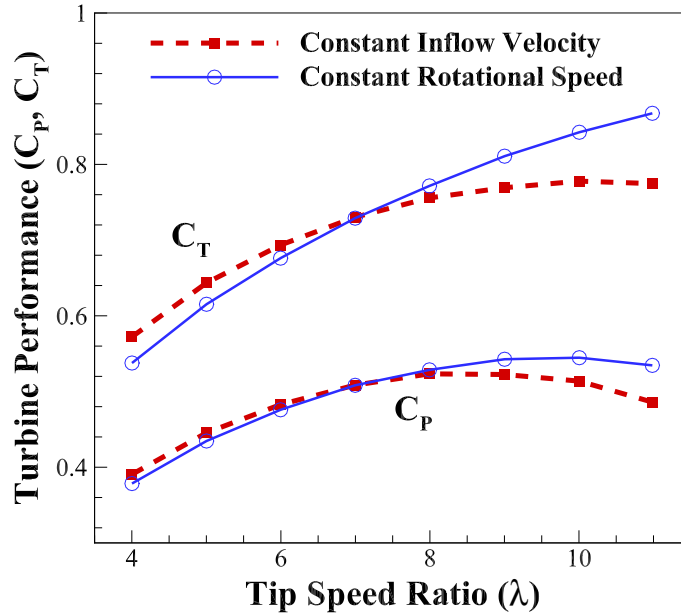
Figure 2.4: Predicted performance of an adaptive turbine in open water flow considering changing tip speed ratio as a function of U or ω only.

inflow velocity. This requires a comprehensive understanding of the local flow environment and of the possible interactions between the blades and these flows.

2.4   Site-Specific Design

Because of the importance of velocity profile characteristics in adaptive turbine design, it is essential to inform numerical simulations with realistic inflow data. The state of technology at present indicates that only areas with peak currents of 2 m/s or more are viable sites for tidal turbine implementation. While 2 m/s (3.9 kts) is a very strong current relative to most tidal locations, some sites experience currents that exceed 5 m/s. As thrust increases with the square of velocity and power with velocity cubed, the difference between the extreme loads and available power experienced at a 2 m/s site and a 5 m/s site suggests that optimal technology and design may be highly dependent on location [25, 38]. In that light, this work uses data from a local tidal energy study to inform velocity ranges and inflow profiles. Researchers at the University of Washington have been collecting baseline

data to inform the design, siting, and permitting of a potential pilot scale tidal energy array in Admiralty Inlet in Puget Sound, WA [102]. As an example, a four-day sample from a 104-day stationary survey (December 2012-April 2013) using a bottom-mounted acoustic Doppler current profiler is shown in Figure 2.5. The associated average annual distribution of the depth-averaged inflow velocity, based on a probability distribution of the full 104-day sample, is shown in Figure 2.6.

While the velocity and direction of tidal flows are vastly more predictable than wind [115], local variations in the flow profile for any given tidal cycle are to be expected due to local bathymetry and boundary effects caused by the sea floor and water surface [107]. An example of this phenomenon can easily be seen in Figure 2.5. The predictable bi-directional nature of the average inflow is evident, with an approximate 180 degree change in the flow direction, and variations such as boundary effects from the seabed and water surface can be seen as well. Figure 2.5 demonstrates the highly dynamic nature of the instantaneous velocity profile, a profile difficult and impractical to model. For numerical simulations, boundary layer effects can be approximated with a power-law estimate of the flow velocity across the water column, as shown in Figure 2.7. Here, a 1/7th-power law is applied, where the fluid velocity, U, at a specific height above the sea floor, h, can be defined as

$$U\left(h\right) = U_{avg}\left(\frac{h}{h_0}\right)^{1/7} \tag{2.3}$$

where U_{avg} is the mean inflow velocity in the turbine's plane of rotation and h_0 is the distance from the center of the hub to the sea floor. It is important to note that the power law is a general approximation for the mean profile and the model will likely not hold for any instantaneous profile depending on the location of the turbine in the water column and its position in the tidal cycle. Near the seabed especially, vertical shear can become a significant component of the total force on the blade. While the accuracy of the power-law estimate is a function of location in the water column, it is adequate to provide a rough profile estimate that includes a representation of the variable amplitude loading that an MHK turbine blade will experience, allowing for the consideration of potential blade fatigue
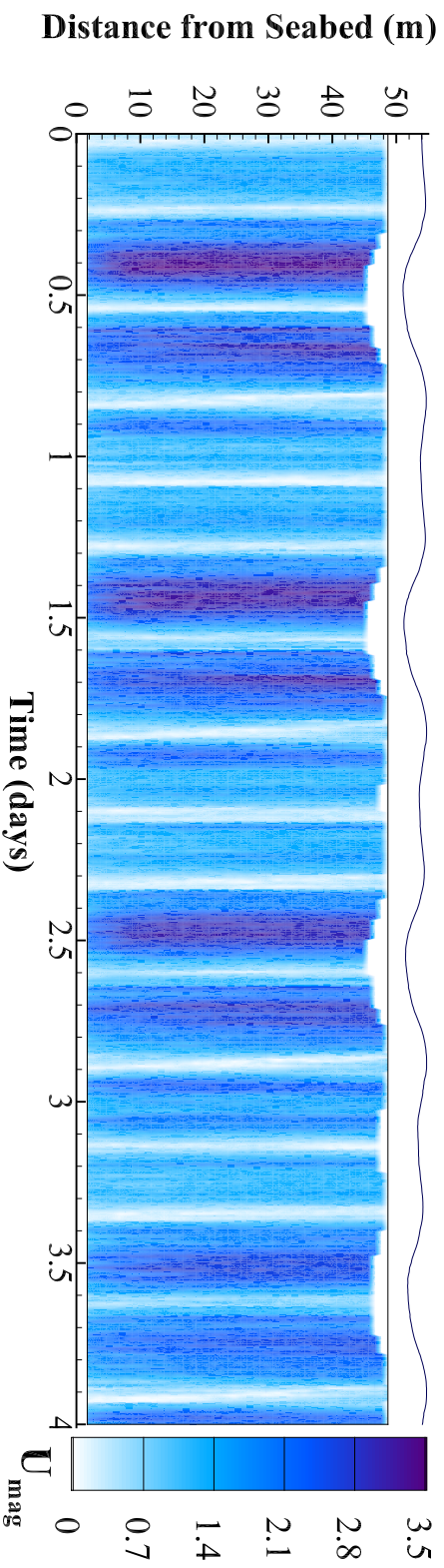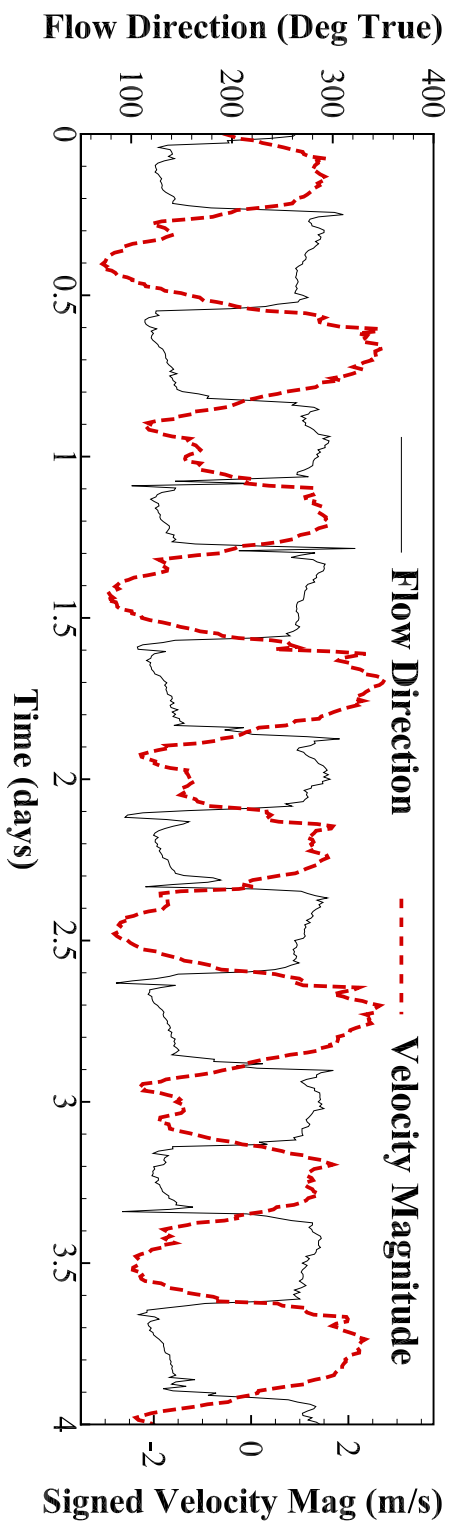
Figure 2.5: Top: Measured flow direction and depth-averaged velocity magnitude data from Admiralty Inlet, WA; Bottom: Measured velocity magnitude over depth from Admiralty Inlet, WA.
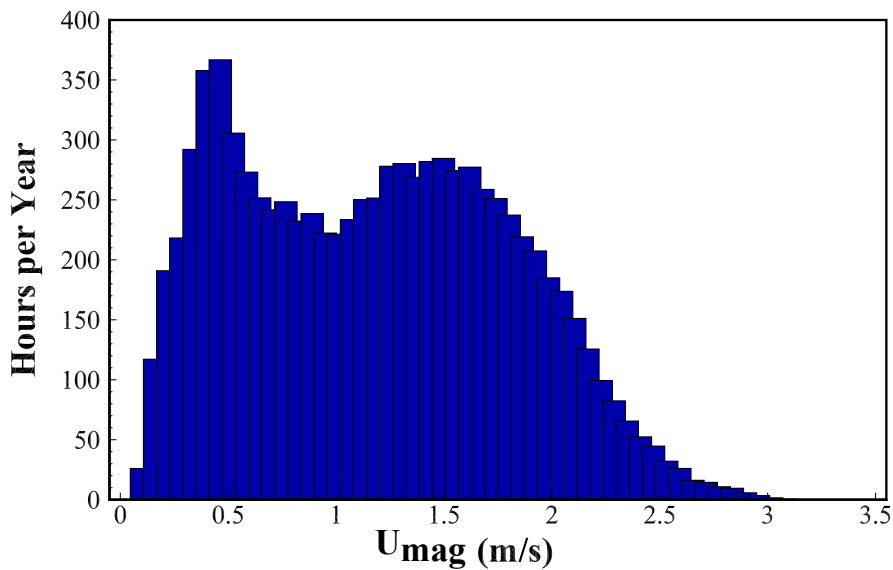
Figure 2.6: Average annual distribution of depth-averaged inflow velocities measured at Admiralty Inlet, WA (associated with data shown in Figure 2.5).

or other structural instabilities.

Marine turbines experience highly nonuniform inflow profiles because of boundary layers, free surface waves, currents, turbulence, and interaction between blades and nearby structures; thus, the effective fluid inflow angle on each blade varies constantly as it rotates in a spatially and temporally varying flow. Due to the constant and nearly instantaneous pitch adaptation inherent to passive control systems, they are ideal for these highly unsteady loading environments where fixed geometries can become suboptimal in off-design conditions, as the intrinsic bend-twist coupling behavior of anisotropic composites will passively adjust the pitch distribution of a blade in order to maintain an effective angle of attack at each blade section.
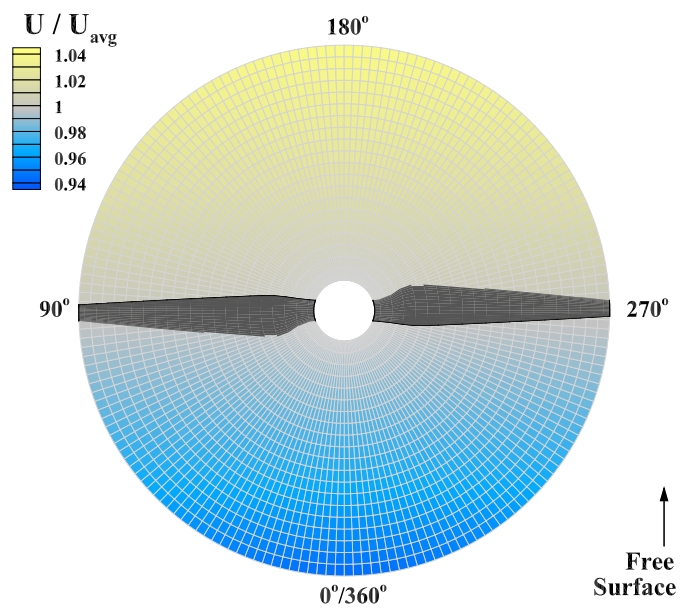
Figure 2.7: Schematic of an axial-flow turbine with a spatially varying effective inflow approximated with a 1/7th-power law.

Chapter 3

METHODOLOGY: FLUID-STRUCTURE INTERACTION MODELING

In modeling the complex and often non-linear effects of fluid-structure interactions, the selection of an appropriate numerical tool is paramount. In most applications, turbine blade deformations are assumed to be negligible and the geometry is treated as rigid; this enables the use of nondimensional parameters to characterize operating conditions and greatly simplifies the design process. The performance of an adaptive blade, however, is governed by the material and geometry design and is strongly influenced by the load-dependent deformations. Because of this, an iterative fluid-structure analysis process is necessary to predict the blade geometry at any given condition. Additionally, due to the fact that the performance of an adaptive blade depends on the total dimensional blade loading, it is important to consider the magnitudes of both the inflow velocity and rotational frequency, not solely their ratio. Thus, the full range of expected operating conditions must be studied in order to achieve a complete representation of rotor performance, as discussed in Section 2.3.

The need for an iterative analysis process combined with the increase in operational parameters necessary to consider for the design of an adaptive blade significantly increases the computational requirements of the problem. It is therefore necessary to find a balance between desired model fidelity and available computational resource in order to facilitate the design of passively adaptive turbine blades. This section will provide a brief discussion of different commonly used fluid analysis techniques followed by an in-depth description of the method used for this work.

3.1 FSI Modeling Techniques: Fluid Analysis Methods

3.1.1 Blade Element Momentum Theory

Blade element momentum theory (BEMT) is one of the oldest and simplest methods applied to the problem of a foil rotating in a fluid.[1] BEMT is in fact a product of two different theories: blade element theory and momentum theory, first combined by Betz and Glauert in 1935. In blade element theory, the blade is divided into a number of independently operating 2-dimensional sections whose aerodynamic forces can be summed along the length of the blade to determine the total moments and forces on the rotating body [81]. Blade element theory calculates the forces on each section based on the local incident flow angles and thus requires previous knowledge of lift and drag characteristics for the foil in question. These can be determined empirically or numerically and can, depending on the foil and the flow regime, be highly dependent on Reynolds number. On the other side, momentum theory is based on an assumption that replaces the rotor with an actuator disk of equal diameter and infinitesimal thickness. Momentum theory equates the drop in pressure across the plane of the disk to the thrust or drag force on the rotor disk. With a complementary assumption about the turbine efficiency, average axial and rotational velocities induced by the rotor can be calculated [28].

Together, blade element and momentum theories create a fast, iterative method to determine both the induced velocities created near the rotor and the aerodynamic forces acting on the rotor. However, there are limitations associated with the simplicity of the BEMT method. In particular, BEMT assumes completely static conditions in which the flow field is always in equilibrium. This precludes the use of classical BEMT with more realistic nonuniform or transient inflow models, as well as limiting the usefulness of the method near stall conditions [16, 98]. Additionally, because momentum theory is applied in the plane of the rotor, BEMT cannot account for large out-of-plane deformations in the blades; meanwhile the 2-dimensional assumption of the blade element theory neglects spanwise flow and there-

---

[1]It is important to note that blade element momentum theory is referred to as both BEM and BEMT throughout the literature. Here the acronym BEMT will be used exclusively to refer to blade element momentum theory, reserving BEM for the reference of the boundary element method further discussed in Section 3.1.3.

fore spanwise pressure variation [81]. Taken together, these simplifications make BEMT less accurate for rotors under heavy loads with significant spanwise pressure gradients – a condition which aptly describes most marine turbines. BEMT is also known to over-predict thrust and under-predict torque compared to more robust techniques [44].

Many numerical or empirically-based corrections have been applied in BEMT codes to counter the known weaknesses of the method. Tip- and hub-loss models are used to alter the induced velocities in order to account for the effect of vortex shedding at the respective ends of the blade [81]. Additionally, empirical corrections can be used for high induction flow and near-stall conditions [89]. In spite of the limitations of the method, BEMT is widely used as a preliminary design tool and has been repeatedly verified to a level of accuracy acceptable for many purposes [4, 15, 16, 64, 74].

BEMT is generally coupled with a finite element method (FEM) solver by applying the lift and drag forces calculated for each individual blade element to discrete nodes in an FEM model of the blade, often at the aerodynamic center of the blades. This predicts spanwise loading of the blade, but gives no indication of chordwise loadings or pressure distribution [16]. Due to the simplicity of the output blade loading, at times BEMT is coupled with a more basic beam model to streamline the computational process [97]. Though the abilities of BEMT are limited, the strength of the method lies in its simplicity. The code can be executed very quickly and lends itself easily to the many iterations needed for optimization or FSI modeling. At early stages in the design process, BEMT is a valuable tool; however, a more complete solver is needed to resolve 3-dimensional flow details and pressure distributions on the blade [18, 44]. These details are particularly important in advanced analyses for systems that may be susceptible to cavitation, as BEMT is not able to predict the onset of cavitation except with the use of empirical relationships.

3.1.2 Lifting Line and Lifting Surface Methods

The lifting line and lifting surface methods were developed to gain further insight into the rotating foil problem. In the lifting line method, the rotor blade is represented by a spanwise distribution of its section properties, allowing the blade to be modeled as a line

of bound circulation that varies radially [48]. The lifting line method includes the addition of tip vortices, which improves the analysis of the near field flow, but is limited by the 1-dimensional representation of each blade section.

The lifting surface method is a further extension of the lifting line method. In this method, the line of the blade becomes an infinitely thin plane situated along the blade camber line. This plane contains a similar distribution of vorticity, but additional sources and sinks are distributed in the spanwise and chordal directions to approximate the surface pressure field of the blade [101]. The lifting surface method results in a more detailed model than BEMT and lifting line methods and it is able to approximate pressure distributions along the blade in steady and unsteady flow conditions, allowing for the prediction of cavitation initiation [58, 59, 67]. However, it does not account for the thickness of a blade; this is a significant drawback especially in the study of marine propellers and turbines, which are typically designed with smaller aspect ratios and greater blade thicknesses relative to other rotors [36]. Because of this, use of the lifting surface method has largely been replaced with the more complete and only slightly more complex boundary element method, though lifting line and lifting surface methods are still used as preliminary design tools [75]. For completeness, more details of the lifting surface formulation can be found in [55].

3.1.3 Boundary Element Method

Boundary element method (BEM) is a 3-dimensional panel method which models the surface of a rotor and its trailing vortex sheet. More computationally expensive than the BEMT and lifting surface methods, BEM gained popularity with the increase in computing power available in the early 1960s [80]. Like the lifting surface method, BEM is a potential flow method; however, BEM models the entire surface of the blade, fully accounting for the thickness of the foil. BEM applies the governing Laplace equation as integral identities along the boundary surface, which is divided into small panels. Sources, sinks, vortices and doublet elements are superimposed linearly along the surface; their strengths are assigned in a way that satisfies the boundary conditions on the body, across the wake and in the far field [80]. Similarly, BEM models the trailing vortex sheet with similar panels, realizing

further details of the flow in the wake region. Because the method models the 3-dimensional lifting surface in full by segmenting the boundary into small panel elements, it is able to conform to any complex geometry. Unlike its predecessors, BEM is particularly effective in capturing flow details at the blade leading edge and tip and accounting for the effect of nonlinear thickness-loading coupling [130].

Though BEM requires more computational expense than BEMT, it still involves only around 1% of the effort needed for full CFD simulations [35]. This is because the fluid equations are solved only on the boundary, across the near wake and in the far field instead of throughout the entire domain. With the increased effort comes an improvement in modeling ability; because of its formulation, BEM can easily handle complex geometries, nonuniform and transient inflow profiles, and significant out-of-plane deformations. Because BEM is a potential flow method, it cannot account directly for frictional drag; however, the flexibility of the method allows for the incorporation of models to account for rotational and viscous flow effects such as wake roll-up, separation and stall [51]. Commonly, BEM codes are coupled with a boundary layer solver to include the effect of viscosity. The boundary layer method iterates through taking the surface pressure distribution from the potential flow solver, calculating boundary layer characteristics, and modifying the surface boundary conditions for the next loop [80]. In other cases, an empirical skin calculation is used to estimate viscous effects [94]. Because BEM computes the pressure distribution on the blade, it can be used to predict cavitation. BEM can also be modified to account for supercavitating and surface piercing conditions [119–122].

BEM is particularly well suited to FSI modeling because it solves for the full pressure distribution along the surface of the blade, which provides highly detailed input for structural models. Added mass and damping effects can be superimposed onto structural mass and damping matrices in an FEM model in order to fully account for FSI effects. Added mass has been found to be particularly important for adaptive foils and blades due to the large effect on natural frequencies [118, 130]. BEM has been verified and widely used in modeling adaptive marine propellers and turbines in steady and spatially varying flow, for both subcavitating and cavitating regimes [12, 22, 63, 82–84, 86, 118, 125].

32

3.1.4   Computational Fluid Dynamics Methods

Though fast, inviscid methods such as BEM are very useful under many conditions, they are unable to detect tip vortices, cavitation collapse, and other viscous features in the flow field. These features have the potential to lead to flow-induced vibrations and hydroelastic instabilities such as flutter or divergence, which can severely affect the structural response and longevity of a turbine blade [128]. Additionally, they have a significant impact on the wake of the system. A detailed understanding of the wake is essential in many applications, including siting, array configuration, and environmental impact assessment. To that end, a number of high-fidelity computational fluid dynamics (CFD) approaches have been developed, including Reynolds Averaged Navier-Stokes (RANS), Large Eddy Simulation (LES), Detached Eddy Simulation (DES), and Direct Numerical Simulation (DNS). Generally, these methods use finite volume algorithms to solve for the fluid behavior throughout the computational domain [79]. The choice of algorithm is situational; each method approaches the problem of turbulence differently and is therefore suitable for different applications.

The simplest in theory, Direct Numerical Simulation (DNS) is also the most complex. As the name suggests, DNS solves the Navier Stokes equations directly. In this method a turbulence model is not needed, as turbulent behavior is resolved on every scale; however this can be extremely costly for complex problems. On the other end of the spectrum, a Reynolds Averaged Navier-Stokes (RANS) method uses time-averaged equations to model fluid flow. RANS methods represent the effect of turbulence in the flow with various stress models that can, depending on complexity, account for flow history effects such as convection and diffusion [95]. Large Eddy Simulation (LES) falls in between DNS and RANS methods in depth, in that large eddies in the flow are represented explicitly but the effect small-scale eddies is applied implicitly across the model. However, LES models can break down in some near-boundary situations, and hybrid techniques RANS-LES such as Detached Eddy Simulation (DES) have been developed for those scenarios. These methods have gained in practicality with modern advances in computing capabilities, yet they continue to be highly numerically intense. Additionally, the accuracy of these simulations depends strongly on grid resolution and meshing technique, making them costly in terms of both mesh

building and computations [61]. Because of the complexity of the problem, RANS codes are used most commonly in marine turbine modeling as they are slightly less computationally expensive [95], though as costs decrease other methods are becoming more widely used.

Unlike potential flow methods, viscous methods can account directly for rotational and viscous flow effects such as wake roll-up, separation, boundary layers, and stall. The selection of turbulence solver and addition of various cavitation models can be combined to simulate a multitude of complex problems. These high-fidelity modeling techniques are able to confirm system performance over a wide range of complex operating conditions, including regimes in which potential flow assumptions are no longer valid. Thus, viscous FSI methods are needed to fully capture dynamic interactions between the flow and blade/foil deformations and the associated hydroelastic instabilities and material failure issues, especially at off-design conditions.

3.2   Research Modeling Approach

In order to accurately predict the response of adaptive turbine, modeling of the FSI effects that cause load-dependent deformation of the blade is essential. Because of the complexity of the loading and deformation response of an adaptive blade, a simplistic analysis tool (*i.e.*, Blade Element Momentum Theory, Lifting Line/Lifting Surface methods) is not sufficient; however, a viscous CFD simulation for every step of the procedure would be costly to the point of infeasibility. It is therefore necessary to find a balance between model fidelity and computational expense in order to facilitate the design and analysis of passively adaptive turbine blades. To this end, turbine blades in this work are modeled with a previously developed, fully coupled boundary element method-finite element method (BEM-FEM) solver. At the start of the research presented in this work, this method had been fully validated for use with rigid and adaptive marine propellers [57, 58, 117, 119, 120, 126] and preliminarily validated with the limited experimental results available for rigid turbine blades [130]; adaptive turbine blades had not been experimentally tested at that time.

The BEM-FEM solver begins with the undeformed blade geometry and a velocity profile in the plane of blade rotation. The BEM code uses that information to solve for the hydrodynamic loading on the blade, which is then passed to the FEM code to determine

blade deformation. The geometry is updated and returned to the BEM code to find the new corresponding loading profile. This process iterates until reasonable convergence is reached. A complete description of the formulation and implementation of the solvers can be found in [57, 117, 118]; a detailed overview is presented in the sections below.

3.2.1 Fluid Modeling

The BEM solver of the coupled BEM-FEM pair is a low-order, 3-D potential-based boundary element code called HE-PROPCAV [123]. PROPCAV was originally developed for the analysis of fully-wetted marine propellers in steady flow, and has been extended to model marine turbine blades and to consider the effects of non-axisymmetric flow, surface piercing, free surface effects, sheet cavitation, supercavitation, and mid-chord cavitation on both sides of the blade surface [55, 58, 119, 120, 130]. The effects of viscosity are represented in PROPCAV with the application of a uniform friction coefficient applied at the wetted blade surfaces [28].

A potential flow code, PROPCAV solves the incompressible Euler equations in a blade-fixed rotating coordinate system. The turbine (and thus the coordinate system) is assumed to be rotating at at constant angular velocity ω. The effective inflow velocity, $\mathbf{U_e}$, is taken as the sum of the inflow in the absence of the turbine and the vortical interaction between the turbine and the inflow, or the total velocity minus the turbine-induced velocity from potential flow theory, and is defined in the non-rotating coordinate system. At a given location, $\mathbf{x} = (x, y, z)$, in the blade-fixed, rotating coordinate system the total velocity, $\mathbf{U_t}$, is expressed as the vector sum of the inflow velocity directly upstream of the turbine, $\mathbf{U_{in}}$, and the perturbation velocity potential, $\nabla \mathbf{\Phi}$, corresponding to the turbine-induced flow field, both expressed in blade-fixed coordinates. The inflow velocity, $\mathbf{U_{in}}$, can be further decomposed into the effective wake velocity and the blade rotational velocity as shown below.

$$\mathbf{U_t} = \mathbf{U_{in}} + \nabla \mathbf{\Phi} \tag{3.1}$$

$$\mathbf{U_{in}} = \mathbf{U_e} - \mathbf{\Omega} \times \mathbf{x} \tag{3.2}$$

where $\boldsymbol{\Omega}$ is the turbine rotational speed vector $[0, 0, \omega]^T$. The perturbation flow can be assumed to be incompressible, inviscid and irrotational.

The momentum equation with respect to the rotating blade-fixed coordinate system can be expressed

$$D\mathbf{U_t}/Dt = -\nabla P/\rho + \mathbf{g} - \boldsymbol{\Omega} \times (\boldsymbol{\Omega} \times \mathbf{x}) - 2\boldsymbol{\Omega} \times \mathbf{U_t} \qquad (3.3)$$

where P is the hydrodynamic pressure, ρ is the fluid density, and $\mathbf{g}$ is the gravitational acceleration. The last two terms are the centrifugal acceleration $(-\boldsymbol{\Omega} \times (\boldsymbol{\Omega} \times \mathbf{x}))$ and the Coriolis acceleration, or conservation of angular momentum $(-2\boldsymbol{\Omega} \times \mathbf{V_t})$, respectively.

By integrating the inviscid incompressible momentum equation between two points along a streamline and applying the continuity equation $\nabla \cdot \mathbf{U_t} = 0$, the following equation for the absolute total pressure P_t can be derived [117]

$$P_t - P_0 = \rho \left[\frac{1}{2}|\mathbf{U_{in}}|^2 - \frac{\partial \boldsymbol{\Phi}}{\partial t} - \frac{1}{2}|\mathbf{U_t}|^2 \right] \qquad (3.4)$$

where P_0 is the absolute hydrostatic pressure at $\mathbf{x}$.

The fluid problem therefore is to solve for the perturbation velocity potential $\boldsymbol{\Phi}$, which is governed by the Laplace equation $\nabla^2 \boldsymbol{\Phi} = 0$. To consider FSI effects, $\boldsymbol{\Phi}$ can be linearly decomposed as follows

$$\boldsymbol{\Phi} = \phi + \varphi \qquad (3.5)$$

where ϕ is the part of the perturbation potential due to large rigid blade deformations and φ is the part due to the much smaller elastic blade deformations. The decomposition of $\boldsymbol{\Phi}$ allows the total pressure, P_t, to be similarly decomposed into rigid blade (P_r) and elastic blade (P_v) components as follows.

36

$$P_t - P_0 = P_r + P_v \tag{3.6}$$

$$P_r = \rho \left[\frac{1}{2} |\mathbf{U_{in}}|^2 - \frac{\partial \phi}{\partial t} - \frac{1}{2} |\mathbf{U_{tr}}|^2 \right] \tag{3.7}$$

$$P_v = \rho \left[-\frac{\partial \varphi}{\partial t} - \mathbf{U_{in}} \cdot \nabla \varphi \right] \tag{3.8}$$

As both ϕ and φ are governed by the Laplace equation, they can be reduced to boundary value problems. PROPCAV solves for ϕ and φ using a 3-D BEM approach and applying kinematic and dynamic boundary conditions as described in [130]. P_r and P_v are then passed to the FEM solver to determine blade deformation.

3.2.2 Structural Modeling

The commercial FEM solver ABAQUS [1] is used for the dynamic structural analysis of the blade. In the blade-fixed coordinate system, the discrete equation of motion can be expressed as

$$[\mathbf{M}]\{\ddot{\mathbf{u}}\} + [\mathbf{C}]\{\dot{\mathbf{u}}\} + [\mathbf{K}]\{\mathbf{u}\} = \{\mathbf{F_{ce}}\} + \{\mathbf{F_{co}}\} + \{\mathbf{F_h}\} \tag{3.9}$$

where $\{\ddot{\mathbf{u}}\}$, $\{\dot{\mathbf{u}}\}$, and $\{\mathbf{u}\}$ are the structural nodal acceleration, velocity, and displacement vectors, respectively; $[\mathbf{M}]$, $[\mathbf{C}]$, and $[\mathbf{K}]$ are the structural mass, damping, and stiffness matrices; $\{\mathbf{F_{ce}}\}$ is the centrifugal force, $\{\mathbf{F_{co}}\}$ is the Coriolis force, and $\{\mathbf{F_h}\}$ is the total hydrodynamic force. Like the total pressure, the hydrodynamic force can be decomposed into rigid ($\{\mathbf{F_r}\}$) and elastic ($\{\mathbf{F_v}\}$) components, by multiplying the rigid and elastic pressures by the element shape functions and integrating over the blade surface, as follows.

$$\{\mathbf{F_h}\} = \{\mathbf{F_r}\} + \{\mathbf{F_v}\} \tag{3.10}$$

$$\{\mathbf{F_r}\} = \int [\mathbf{N}]^T \{\mathbf{P_r}\} d\mathbf{S} \tag{3.11}$$

$$\{\mathbf{F_v}\} = \int [\mathbf{N}]^T \{\mathbf{P_v}\} d\mathbf{S} \tag{3.12}$$

The hydrodynamic force from elastic blade deformations, $\{\mathbf{F_v}\}$, can be computed from Eq. (3.8) and Eq. (3.12) and written as follows [117, 118],

$$\{\mathbf{F_v}\} = -[\mathbf{M_H}]\{\ddot{\mathbf{u}}\} - [\mathbf{C_H}]\{\dot{\mathbf{u}}\} \tag{3.13}$$

where the $[\mathbf{M_H}]$ and $[\mathbf{C_H}]$ matrices represent the hydrodynamic added mass and damping inherent to a structure moving through a dense fluid. $\{\mathbf{F_v}\}$ can be added to the left hand side of the discrete dynamic equation of motion to produce the equation in its final form

$$([\mathbf{M}] + [\mathbf{M_H}])\{\ddot{\mathbf{u}}\} + ([\mathbf{C}] + [\mathbf{C_H}])\{\dot{\mathbf{u}}\} + [\mathbf{K}]\{\mathbf{u}\} = \{\mathbf{F_{ce}}\} + \{\mathbf{F_{co}}\} + \{\mathbf{F_r}\} \tag{3.14}$$

User-defined sub-routines are employed in ABAQUS to obtain $[\mathbf{M_H}]$, $[\mathbf{C_H}]$, and $\{\mathbf{F_r}\}$ from P_r and P_v as provided by the BEM solver. The effects of large, nonlinear blade deformations are considered by iterating between the fluid and solid solvers until the solution reaches reasonable convergence. Detailed formulations of the solution algorithm, governing equations, and boundary conditions can be found in [117, 118].

3.3 Numerical Blade Model Parameters

3.3.1 Material Selection

Because the intrinsic bend-twist deformation coupling behavior of an adaptive blade is a function of the anisotropic nature of composites, material selection is integral to the design process. Variables such as fiber type, matrix material, and the corresponding stiffness and strength parameters can drastically affect the performance of an adaptive blade. The material properties (Young's modulus (E), shear modulus (G), and Poisson's ratio (ν)) and ultimate stress parameters (X, Y, S) of the chosen material, Hexcel IM7-8552, are detailed in Table 3.1 [27]. In Table 3.1, the the 1-axis (or X-direction) is defined as parallel to the fibers, the 2-axis (Y-direction) as perpendicular to the fibers within each laminate layer, and the 3-axis (Z-direction) as normal to the laminate.

The angle at which the fibers of each individual laminate layer are oriented defines both the direction in which the blade will pitch as well as the magnitude of blade deformation;

38

Table 3.1: Material Properties of Hexcel IM7-8552 [27].

$E_1 = 171.42$ GPa	$X_T = 2326.2$ MPa
$E_2 = E_3 = 9.08$ GPa	$X_C = 1200.1$ MPa
$G_{12} = G_{13} = 5.29$ GPa	$Y_T = Z_T = 160.2$ MPa
$G_{23} = 3.13$ GPa	$Y_C = Z_C = 199.8$ MPa
$\nu_{12} = \nu_{13} = 0.32$	$S_{XY} = S_{XZ} = 92.3$ MPa
$\nu_{23} = 0.45$	$S_{YZ} = 75.3$ MPa

thus, the laminate stacking sequence is a critical design parameter for passive pitch adaptation. In practice, composite blades are composed of tens to hundreds of very fine laminate layers. Each lamina can be defined by a primary fiber angle θ from the radial axis of the blade. However, modeling each individual layer is impractical due to the high degree of computational expense, and provides a more detailed analysis than is appropriate for this stage of research. It has been shown that a multi-layered structure can be modeled using an equivalent unidirectional fiber angle, θ_{eq}, which can be found such that the effective stiffness and degree of bend-twist coupling is approximately equal to that of the full structure [69, 85, 86, 118]. The unidirectional fiber angle model need only have enough layers in the through thickness to provide the necessary mesh density for convergence, making computation vastly more efficient. The θ_{eq} of a multi-layered structure can be found by means of a composite plate analysis; in general, there are many different laminate layup sequences that will result in similar load-deformation behavior and passive adaptation and can be modeled with the same θ_{eq}. While this is appropriate to determine the load-deformation characteristics and trends in the stress profile for these linear-elastic structures, detailed analysis of various multilayer models is necessary after optimization to verify structural integrity and blade performance. In designing the blade models used for this work, the anisotropic properties of the composite were oriented within the material elements using an equivalent fiber angle θ_{eq} model to produce passively controlled pitch to feather and pitch to stall blades.

3.3.2   Blade Model

The Department of Energy (DOE) Reference Model turbine RM1, a two-bladed, axial-flow variable speed-variable pitch turbine pictured in Figure 3.1, was used for a baseline system for the numerical portion of this work. The turbine has a diameter of 20 meters and the center of the hub is located 30 meters from the sea floor and approximately 20 meters below the surface. The reference blade geometry was developed from an optimized model presented in [19]; the geometry is shown in Figure 3.2. The turbine geometry was designed for a variable speed-variable pitch system with a rated (maximum) power output of 550 kW and maximum rotational speed of 11.5 rpm. Below rated power, the tip speed ratio is held constant at the optimal operating point $\lambda = 7$; beyond that point, active pitch control is used to maintain rated power. The geometry of the turbine blades is defined by the NACA $63_1 - 424$ airfoil, which was selected due to its relatively high minimum pressure coefficient and thus provides the blade with significant resistance to cavitation. The shape of the airfoil is also known to delay stall [19].

For the BEM-FEM solver used in this work, the FEM model of the blade is made up of quadratic 3-D solid elements. Reduced integration is employed to eliminate the shear-lock failures associated with first-order elements, which causes the model to become unrealistically stiff in shear. The bulk of the model is comprised of 20-node reduced-integration volumetric brick elements representing the body of the blade, with 15-node reduced-integration tetrahedral elements along the leading and trailing edges of the blade to accommodate the narrowing geometry [117, 124]. The nodes at the root of the blade are fixed, representing the rigid connection between the blades and the hub. The carbon fiber laminate is modeled as an orthotropic, linear elastic material with the properties defined in Table 3.1 above.
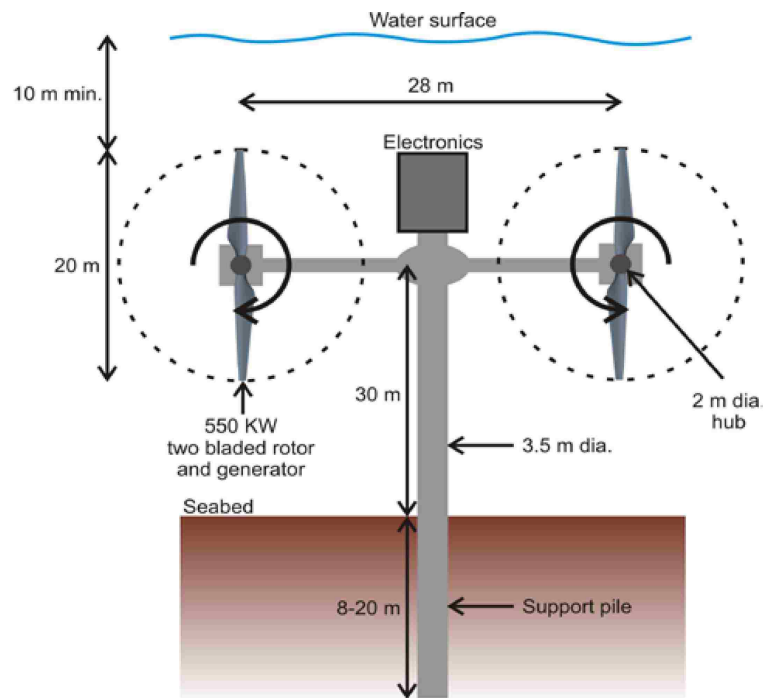
Figure 3.1: DOE Reference Model 1 [19].
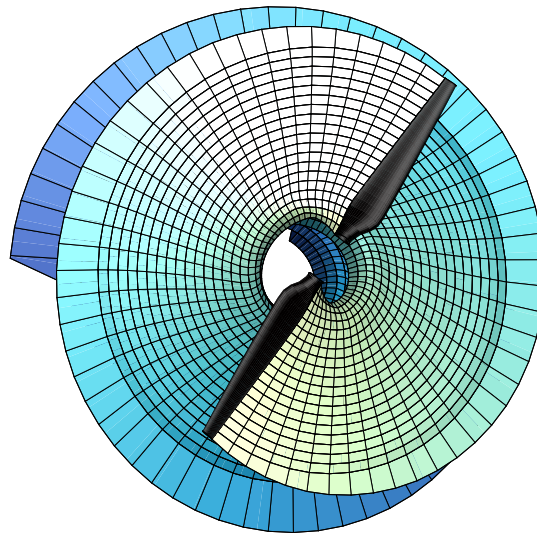
Figure 3.2: Turbine geometry and wake considered in this work.

Chapter 4

PERFORMANCE AND RESPONSE IN A NONUNIFORM FLOW

To begin the discussion of results, a thorough description of the predicted performance and response of a marine turbine under normal operating conditions is presented. The fluid inflow for the FSI analysis is informed by the nonuniform velocity profile discussed in Section 2.4; the blades operate at a constant tip speed ratio of 7, as that was determined optimal in the design of the geometry in [19] (discussed in Section 3.3.2). For this chapter, system limits on power and rotational speed are not incorporated; a full discussion of the interaction between those limitations and passive control systems can be found in [6].

4.1 System Performance

Any evaluation of a marine turbine must begin by examining the coefficients of power and thrust (C_P and C_T), as these parameters provide a valuable, nondimensional metric for assessing the performance of a marine turbine system. Typically, C_P and C_T are presented as a function of tip speed ratio (λ); however, as discussed in Section 2.3, the load-dependent nature of an adaptive blade requires a deeper analysis. The results presented in this section cover the analysis of two sets of three adaptive blades each designed respectively to pitch to feather ($\theta_{eq} > 0$) or pitch to stall ($\theta_{eq} < 0$) in varying degree, compared with a non-adaptive ($\theta_{eq} = 0$) reference blade.

Figure 4.1 shows the evolution of the power coefficient of various adaptive blades with increasing velocity. As designed, the power coefficients of the pitch to stall blades increase with velocity, while those of the feathering blades tend to decrease. This trend intensifies with increasing magnitude of the equivalent fiber angle θ_{eq}, and the non-adaptive reference blade, at $\theta_{eq} = 0$, shows very little change. A corresponding pattern can be observed in the thrust coefficients, shown in Figure 4.2. The blades that increase power production will also experience an increase in thrust, and vice versa.

Figure 4.1: Predicted power coefficient as a function of velocity with a constant $\lambda = 7$ for six adaptive blades compared to a non-adaptive reference blade.

The main mechanism behind the change in power and thrust coefficients is shown in Figure 4.3. This figure shows the change in pitch experienced at each blade tip as the inflow velocity increases. As discussed in [6], the blades designed to pitch to feather increase blade pitch and therefore decrease angle of attack, effectively reducing lift and drag and the corresponding power and thrust coefficients. It is interesting to note that the non-adaptive blade experiences a slight positive pitch change also. This is due to the flexibility inherent in the material and the bias of the geometry, and emphasizes the importance of including structural modeling in a marine turbine analysis. Conversely, the pitch to stall blades decrease blade pitch and increase angle of attack, increasing lift and drag and therefore power and thrust. This also explains the increasing rate of pitch change shown for the adaptive pitch to stall blades; as the velocity and thrust increase, the blade changes pitch in a way that causes additional thrust, adding to the pitch change and corresponding performance metrics. This self-reinforcing behavior can be problematic at higher speeds
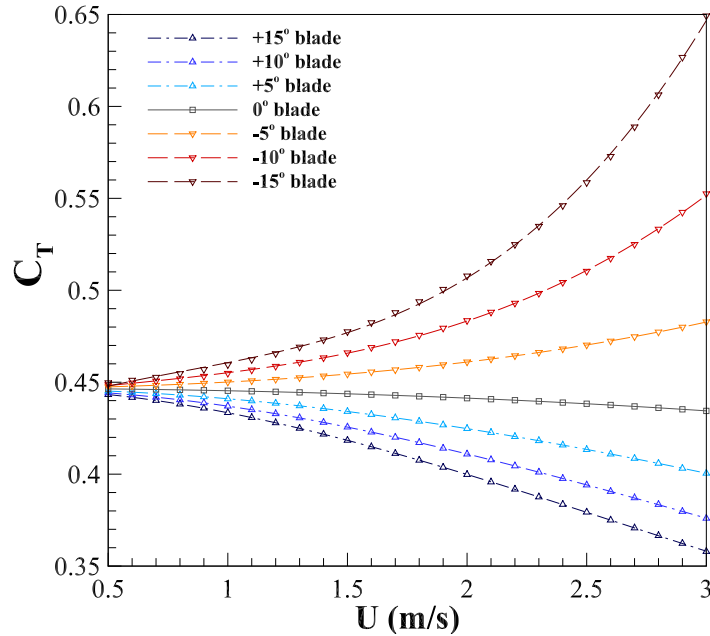
Figure 4.2: Predicted thrust coefficient as a function of velocity with a constant $\lambda = 7$ for six adaptive blades compared to a non-adaptive reference blade.

and larger deformations where static or dynamic divergence can become an issue; this concern is discussed in later chapters. Additionally, it is important to note that increasing the effective angle of attack will at some point cause flow separation and fluid stall; this behavior is not captured in a potential flow method such as the BEM used here and could limit the seemingly positive benefits of the pitch to stall design.

Figures 4.1-4.3 underline the load-dependent nature of an adaptive system; as the velocity and therefore the total dimensional load on the system increases, the blade geometry changes, and this affects the performance. This can also be seen at a smaller level in the performance and deformation behavior of a blade rotating through a nonuniform inflow profile. The above figures show the average performance metrics; in fact, the power and thrust coefficients on each blade in the turbine system change as it revolves.

For clarity, the number of blade models shown in the following figures has been reduced. As evidenced in Figs. 4.1-4.3, the magnitude of the equivalent fiber angle in the adaptive

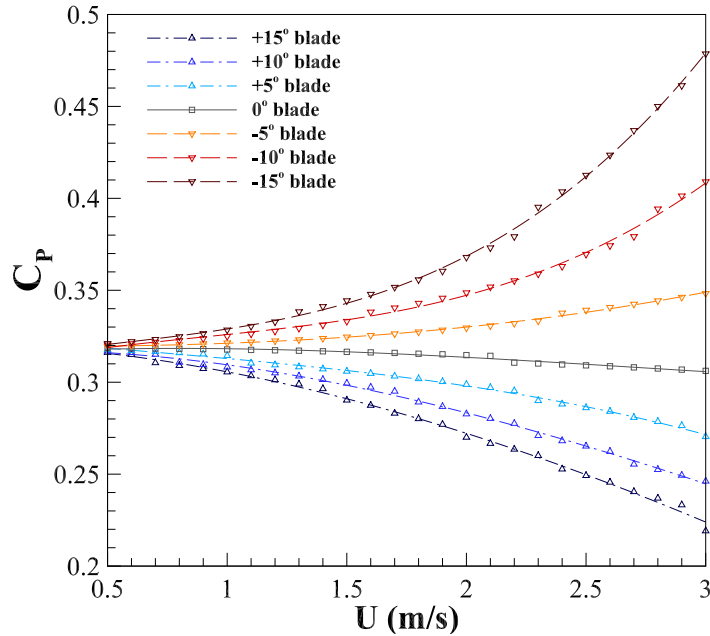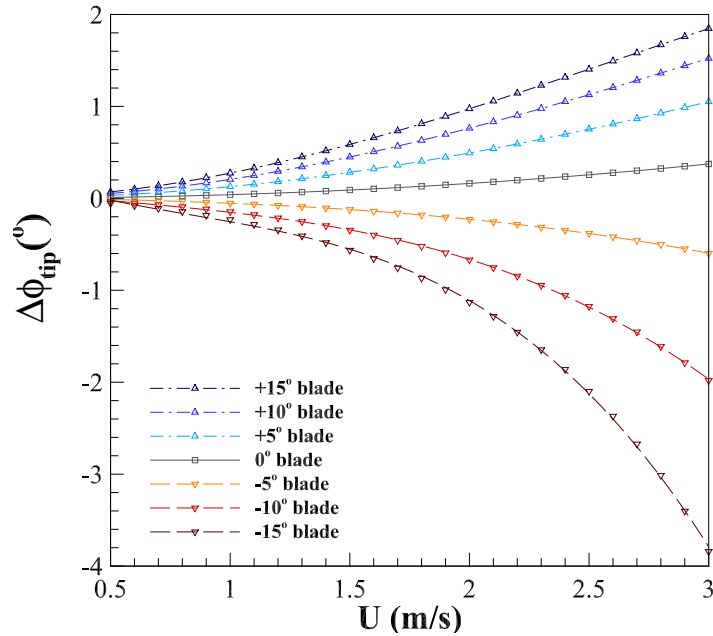Figure 4.3: Predicted change in pitch at the blade tip as a function of velocity with a constant $\lambda = 7$ for six adaptive blades compared to a non-adaptive reference blade.

blades changes the strength of the adaptive response, while the sign of θ_{eq} controls the behavior trend. Therefore, the moderately adaptive blade in each set has been chosen to represent the behavior of pitch to feather and pitch to stall blades in general in the figures below.

Figure 4.4 shows the change in the power (Figure 4.4(a)) and thrust (Figure 4.4(b)) coefficients on one blade of a turbine as it rotates at $U = 2.0$ m/s and $\lambda = 7$. At a blade angle of $0°$, the blade is pointing towards the sea floor; at $180°$ it is at the apex of the rotation, closest to the free surface. The sinusoidal aspect of the performance metrics is expected as the blade moves from a region of higher velocity ($U > U_{avg}$) at the peak of the rotation to the lower velocity area ($U < U_{avg}$) at the base of the rotation, as illustrated in Figure 2.7.

The relationship between loading and bend-twist deformation can be seen in Figure 4.5. This figure shows the displacement (bending, Figure 4.5(a)) and the change in pitch (twist,
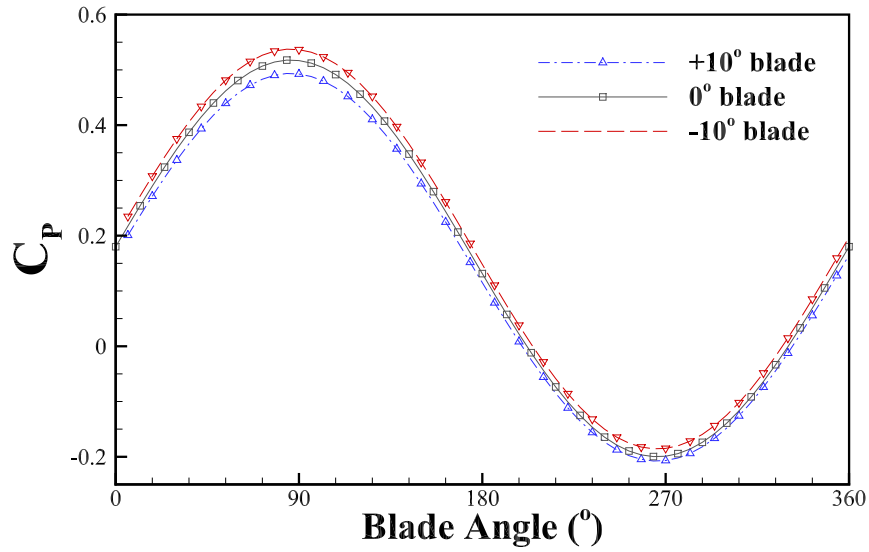
(a) Predicted power coefficients
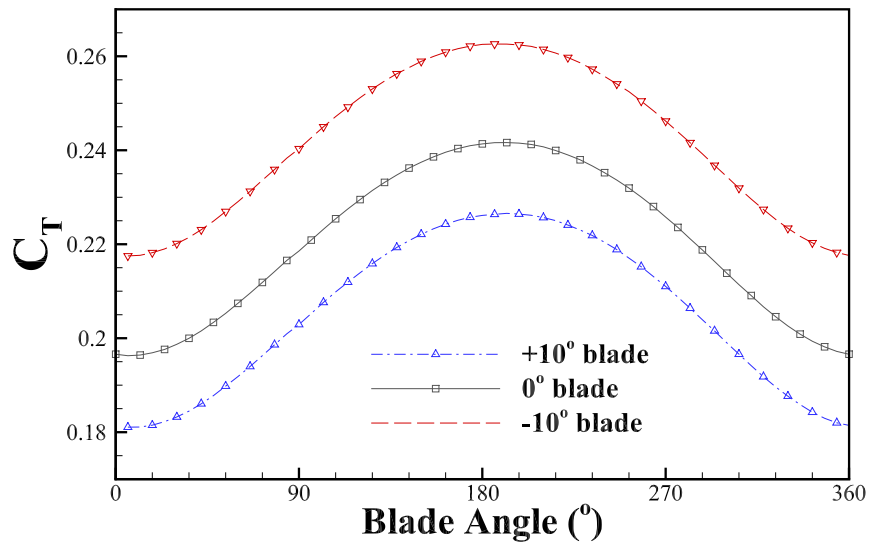
(b) Predicted thrust coefficients

Figure 4.4: Predicted performance coefficients of two adaptive blades and a reference blade over one revolution at $U = 2.0$ m/s and $\lambda = 7$.

Figure 4.5(b)) at the blade tip through a full revolution. At the location of highest thrust, blade angle 180°, the deformations are largest, and they both decrease with the thrust coefficient as the blade moves into the lower velocity region closer to the sea floor. Because of the flexibility and additional twist in the adaptive blades, both passively controlled models experience a larger maximum tip deflection at every point in the rotation than the reference blade. As expected, the change in tip pitch in the adaptive blades increases in magnitude with increasing thrust, following the direction established by the adaptive layup.

4.2 System Response

While power and thrust are essential metrics for judging the performance and viability of a marine turbine system, it is equally important to look at the structural response of a blade. The load-dependent bend-twist deformations affect performance, as discussed above, but also stresses in the body. These stresses can lead to failure of a blade and therefore the turbine, as a failure in one blade will create an imbalance of forces that will quickly propagate throughout the system. Additionally, a closer look at stresses in an adaptive blade can yield further information about the nature and capabilities of the passive pitch response. To that effect, this section examines the stresses in two adaptive blades compared to a non-adaptive reference blade. As above, the moderately adaptive blade in each set is used to demonstrate the behavior of passive pitch blades in general.

Figure 4.6 shows the predicted bending stresses (σ_1) in the three blades at $U = 2.0$ m/s and $\lambda = 7$. Blades are shown at the positions of highest and lowest stresses, *i.e.* with the turbine in the vertical position with one blade pointing towards the free surface and the other towards the sea floor. Both the pressure (upstream) and suction (downstream) sides of the blades are shown. The stresses in this direction are generally the highest, due to the cantilever-type support of a turbine blade; this was true of the results of this analysis. Therefore, in order to be succinct, lower stress directions are not shown.

The bending stresses in Figure 4.6 clearly show the effects of the adaptive mechanism. As expected from the relative thrust coefficients, the highest stresses appear on the pitch to stall blade, while the lower stresses in the feathering blade are a function of its load-shedding capabilities. This can be seen both in tension, on the pressure face, and in compression, on

(a) Predicted maximum tip displacement
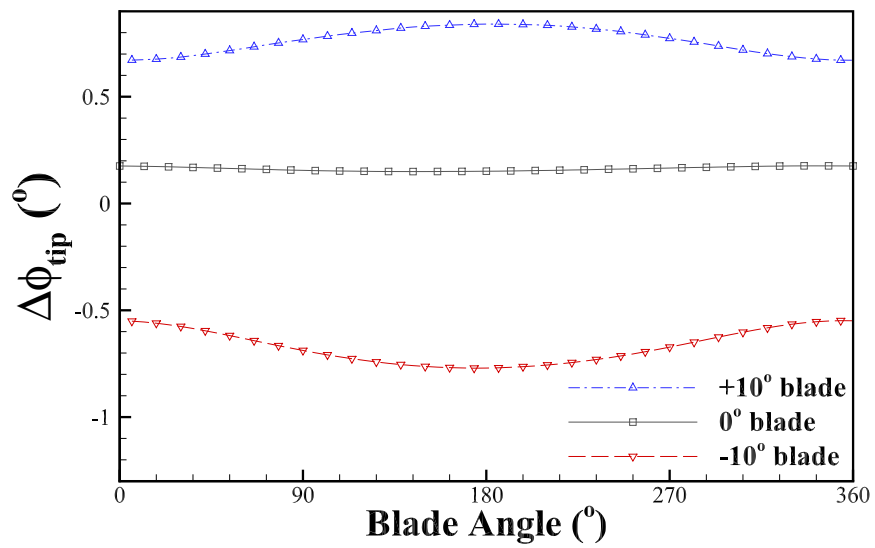
(b) Predicted change in tip pitch

Figure 4.5: Predicted tip deformation of two adaptive blades and a reference blade over one revolution at $U = 2.0$ m/s and $\lambda = 7$.
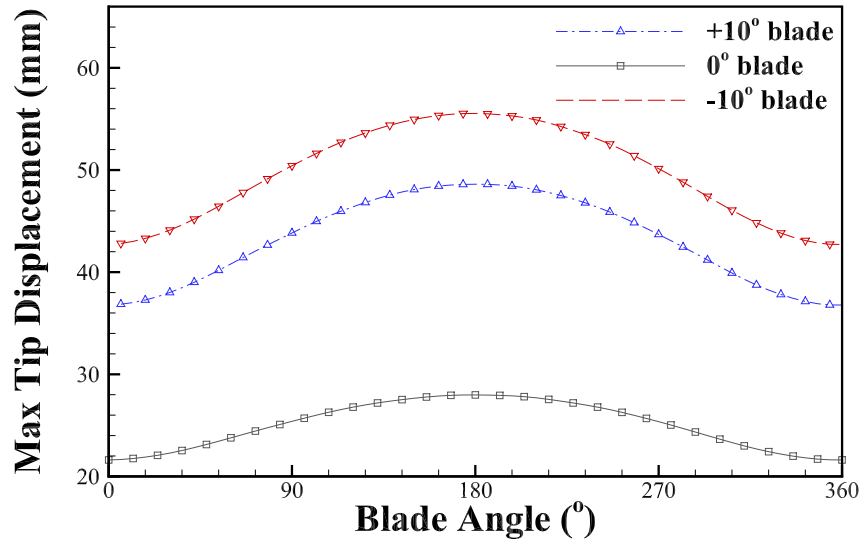
the suction face. Moreover, the orientation of the maximum stress area mirror the dominant fiber angle in the adaptive blades, reflecting the difference in the bending behavior.

Also of interest are the shear stresses (τ_{12}) in the blades, shown in Figure 4.7. Most notable is the order of magnitude difference between shear stresses in the adaptive and non-adaptive blades, showing the increased flexibility and twist in the passive pitch mechanism. Unlike the bending stresses, the magnitude of the stress profiles in the two adaptive blades are comparable, though the stresses in the pitch to stall blade are slightly higher due to the increased thrust. The switch in the direction of the shear stresses between the adaptive blades indicates the opposing directions of twist.

4.2.1   Predicting Composite Failure

In order to quantify the stresses experienced by the turbine blades in a useful way, it is necessary to compare them to a failure index. Fiber-reinforced polymer (FRP) composites like the material modeled in this work are extremely complex, and it is therefore much more difficult to define failure in these composites than in metallic materials. FRP composites are made of many laminate layers of woven polymer matrices strengthened by reinforcing fibers. In these materials, the development of damage leading to fatigue depends on many parameters including geometry, material, laminate lay-up, loading conditions, and load history. Furthermore, composites can display a multitude of failure mechanisms which often build up at the microscopic level and lead to a major visible failure. For the purposes in this work, the most general cases of failure will be considered. A selection of images representative of composite failure modes are shown in Figure 4.8.

On the simplest and smallest scale are failures that develop in the reinforcing fibers, along the ply fiber axis. Fiber tensile failure occurs when the loads applied to the material cause yield or fracture in the fibers. Figure 4.8(a) shows an example of a tensile fracture failure. Tension can also cause individual fibers to pull out of a laminate layer. In compression, fibers can crush, buckle or kink, as shown in Figure 4.8(b). To define tensile or compressive fiber failures, a generally accepted method applies a maximum stress or maximum strain limit [100]. In this work, a maximum stress criteria is used to monitor fiber damage.
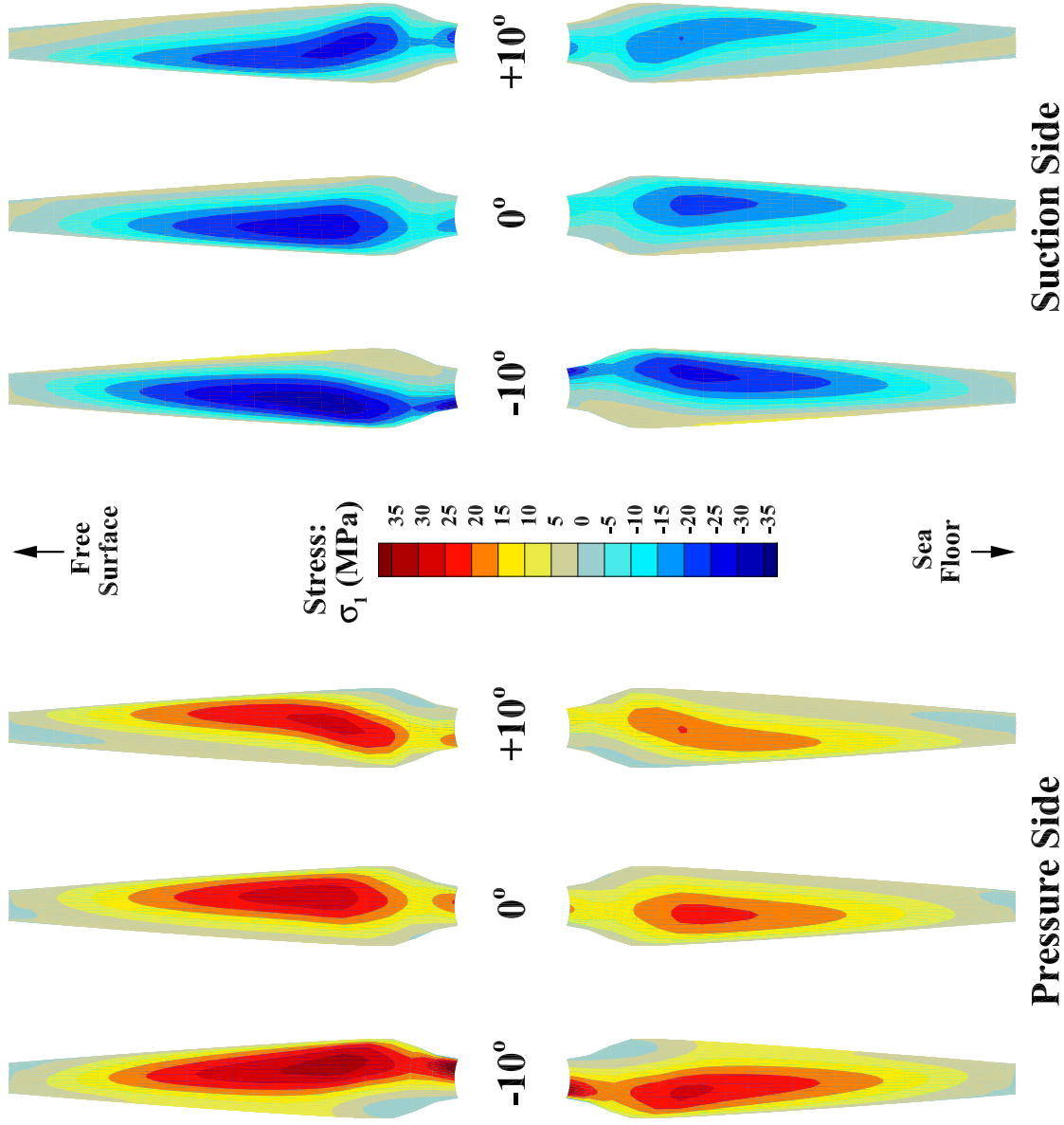
Figure 4.6: Predicted bending stresses (σ_1) in two adaptive blade turbines and a non-adaptive reference system at $U = 2.0$ m/s and $\lambda = 7$. Both the pressure (left) and suction (right) sides of the blades are shown. The turbine is displayed in the vertical position, with one blade pointing towards the free surface and the other towards the sea floor.
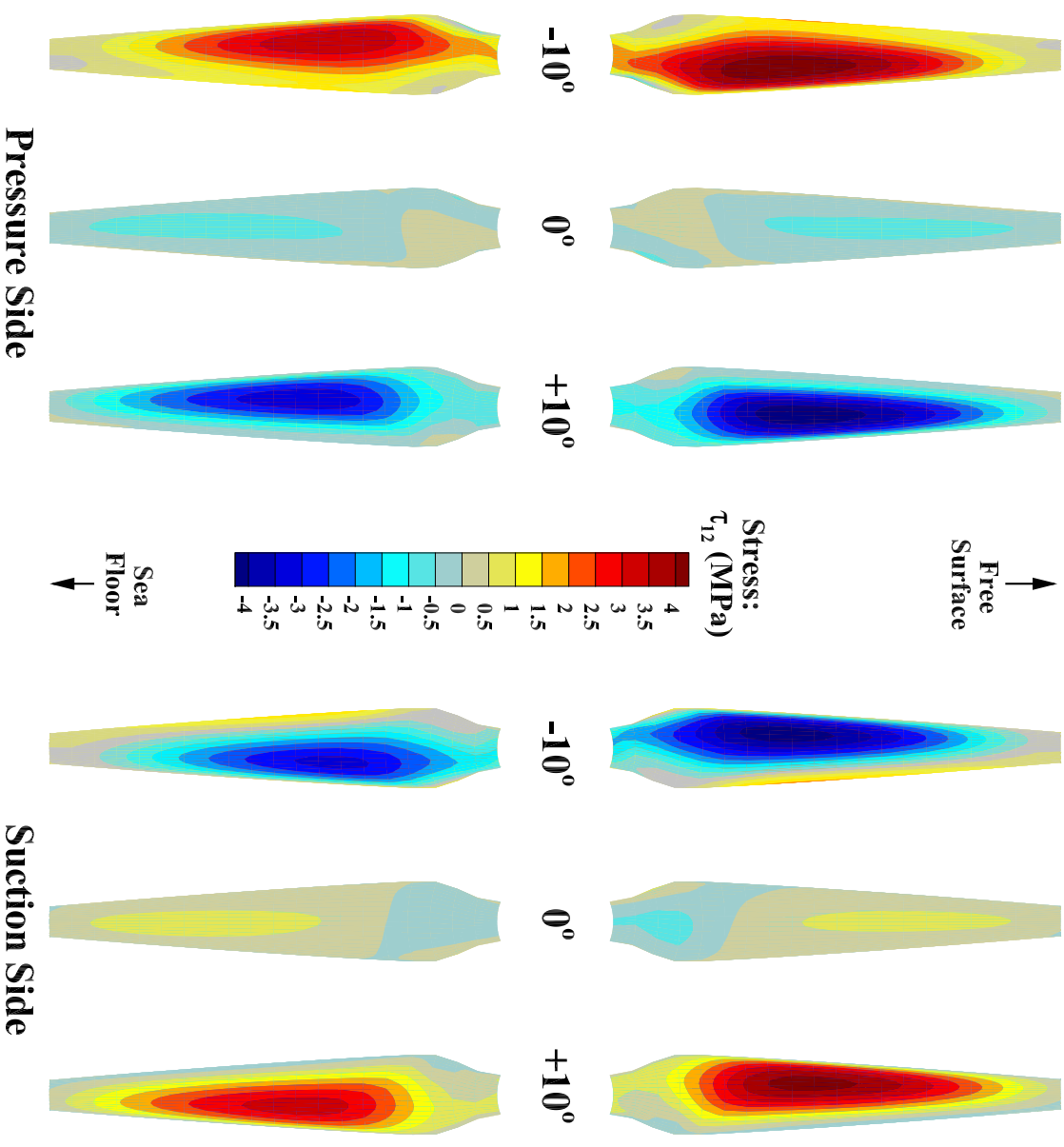
Figure 4.7: Predicted shear stresses (τ_{12}) in two adaptive blade turbines and a non-adaptive reference system at $U = 2.0$ m/s and $\lambda = 7$. Both the pressure (left) and suction (right) sides of the blades are shown. The turbine is displayed in the vertical position, with one blade pointing towards the free surface and the other towards the sea floor.
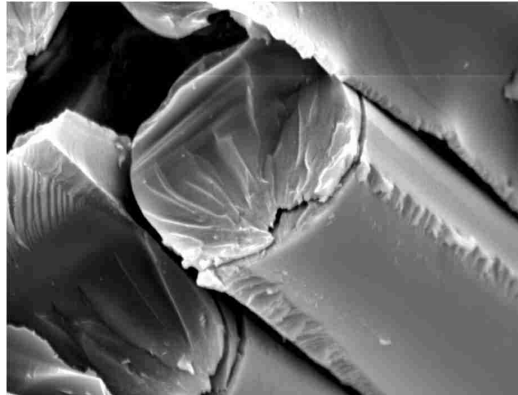
(a) Fiber Tensile Failure: Fracture [2]
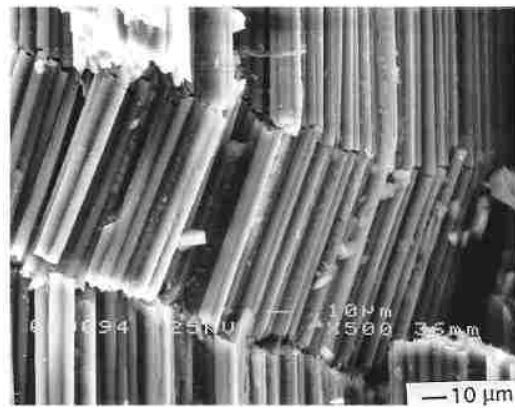
(b) Fiber Compressive Failure: Kinking [99]
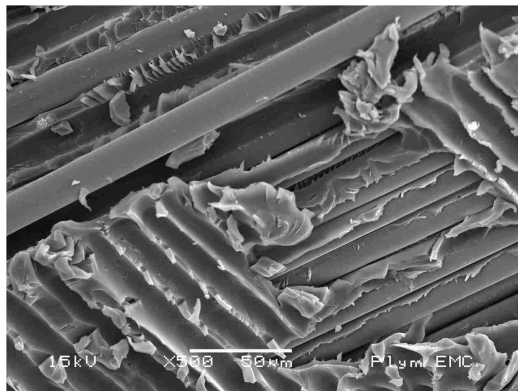
(c) Matrix Failure [2]

Figure 4.8: Examples of various composite failure mechanisms.

The next largest scale failures occur at the matrix level, when cracks or voids form between fibers in the matrix of a single laminate layer. This type of failure generally develops in-plane and orthogonal to the fiber axis, accumulating throughout the laminate and leading to failure across a critical plane, and often propagates from material or manufacturing defects. An example of a matrix failure is shown in Figure 4.8(c). A maximum stress or strain limit can be applied to quantify matrix failure, though more complicated methods are widely used as well. Both a maximum stress limit and a quadratic normal-shear interaction equation are used to determine matrix tension and compression failure indices in this work. To analyze fiber-matrix shear failures, a similar quadratic interaction criterion is used. It is interesting to note that there does not appear to be a consensus on the use of tensile or compressive strength in the denominator of the first term of this equation [100].

On the largest scale of the material, the composite layers can become detached. This is a failure mechanism known as delamination, which generally occurs due to high through-thickness stresses. There are many different standards for analyzing the initiation of delamination and its propagation; the criteria used here focuses on simply the initiation of failure, as an extended study into progressive damage modeling is well beyond the scope of this work. A simple maximum stress and a quadratic interaction limit are applied to determine the probability of delamination initiation here.

While there are many ways to quantify the development of failure mechanisms in composites, this work uses several of the most common methods to determine the mechanisms that introduce the highest likelihood of failure. The failure criteria used here are maximum stress criteria and interaction equations informed by Hashin [49] and Hashin and Rotem [50], and are presented in Table 4.1. Here, σ_1 refers to the stress along the longitudinal axis of the blade, σ_2 the stress along the crosswise axis and σ_3 the through thickness stress. The strength parameters X_T, X_C, Y_T, etc. are listed with the material properties in Table 3.1.

Figures 4.9-4.11 show contour plots of three failure indices. Though all the criteria listed in Table 4.1 were examined, for clarity only the controlling modes are shown here. None of the failure criteria limits are near to being reached in any of the mechanisms; however, there are still several items to be learned from these figures. In Figures 4.9 and 4.10, the tensile and compressive fiber maximum stress failure modes, respectively, are presented. It is clear

Table 4.1: Methods of predicting composite failure mechanisms used in this work.

Criterion	Equation
Fiber Tension, Maximum Stress	$\left\lvert\frac{\sigma_1}{X_T}\right\rvert \leq 1$
Fiber Compression, Maximum Stress	$\left\lvert\frac{\sigma_1}{X_C}\right\rvert \leq 1$
Matrix Tension, Maximum Stress	$\left\lvert\frac{\sigma_2}{Y_T}\right\rvert \leq 1$
Matrix Tension [50]	$\left[\frac{\sigma_2}{Y_T}\right]^2 + \left[\frac{\tau_{12}}{S_{12}}\right]^2 \leq 1$
Matrix Compression, Maximum Stress	$\left\lvert\frac{\sigma_2}{Y_C}\right\rvert \leq 1$
Matrix Compression [50]	$\left[\frac{\sigma_2}{Y_C}\right]^2 + \left[\frac{\tau_{12}}{S_{12}}\right]^2 \leq 1$
Fiber-Matrix Shear, Maximum Stress	$\left\lvert\frac{\tau_{12}}{S_{12}}\right\rvert \leq 1$
Fiber-Matrix Shear [49]	$\left[\frac{\sigma_1}{X_T}\right]^2 + \left[\frac{\tau_{12}}{S_{12}}\right]^2 \leq 1$
Delamination Initiation, Max Stress	$\left\lvert\frac{\sigma_3}{Z_T}\right\rvert \leq 1,\ \left\lvert\frac{\tau_{31}}{S_{31}}\right\rvert \leq 1,\ \left\lvert\frac{\tau_{23}}{S_{23}}\right\rvert \leq 1$
Delamination Initiation [49]	$\left[\frac{\sigma_3}{Z_T}\right]^2 + \left[\frac{\tau_{31}}{S_{31}}\right]^2 + \left[\frac{\tau_{23}}{S_{23}}\right]^2 \leq 1$

that between these two modes, compressive failure is more of a concern; this is logical, as the material strength in tension is nearly twice the strength in compression (see Table 3.1). Though the shear stresses were much lower than the bending stresses for all three blades, the shear strength is also lower, and Figure 4.11 shows that the fiber-matrix maximum shear failure mode controls over the tensile and compressive modes for the adaptive blades. This is valuable to note, as adaptive blades designed to meet structural safety requirements determined for rigid or non-adaptive blades may fail unexpectedly in shear, even in the load-shedding pitch to feather design, if proper consideration for the additional flexibility of the passive pitch mechanism is not taken.
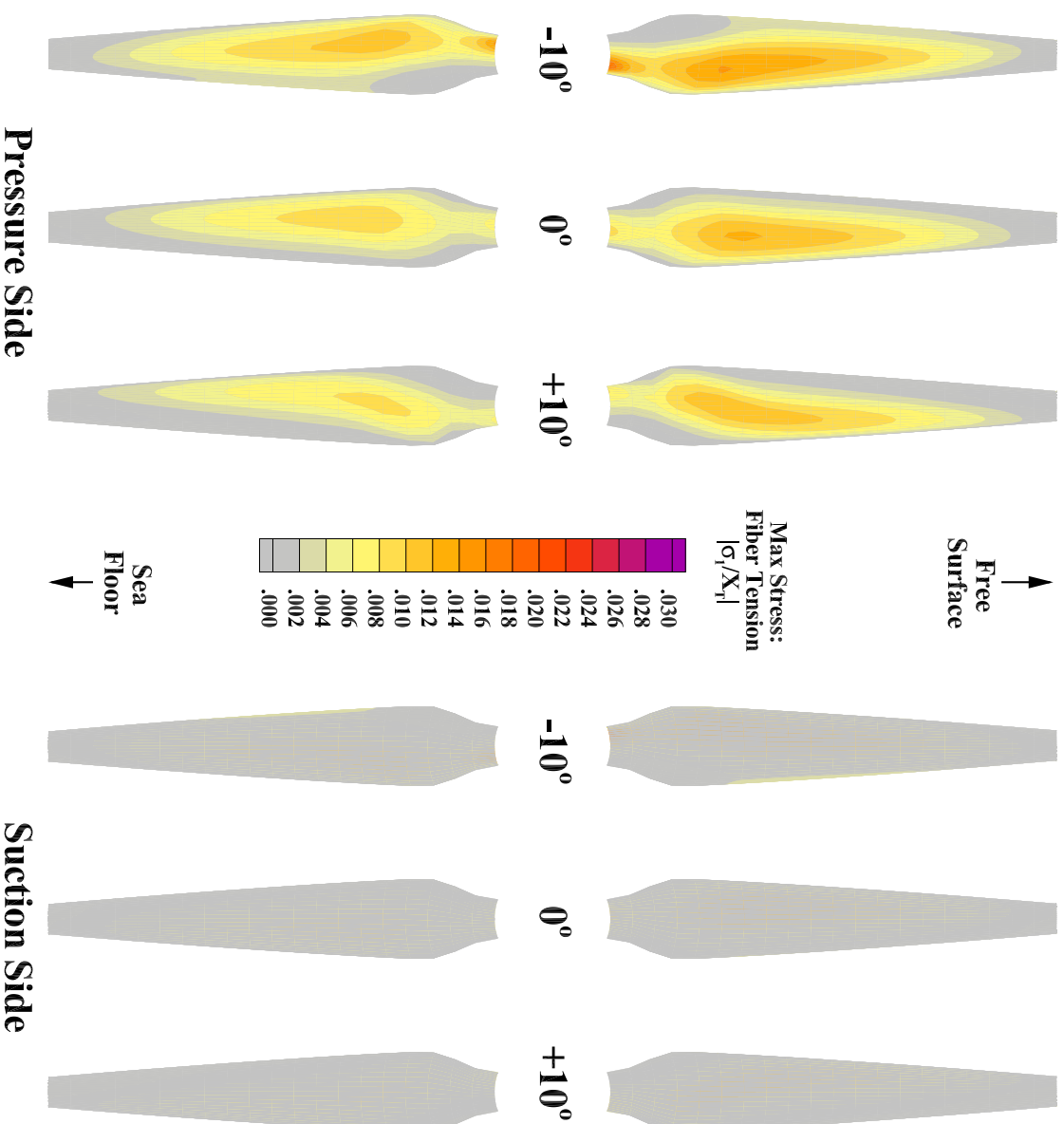
Figure 4.9: Predicted fiber maximum tension stress failure indices ($|\sigma_1/X_T|$) in two adaptive blade turbines and a non-adaptive reference system at $U = 2.0$ m/s and $\lambda = 7$. Both the pressure (left) and suction (right) sides of the blades are shown.

55
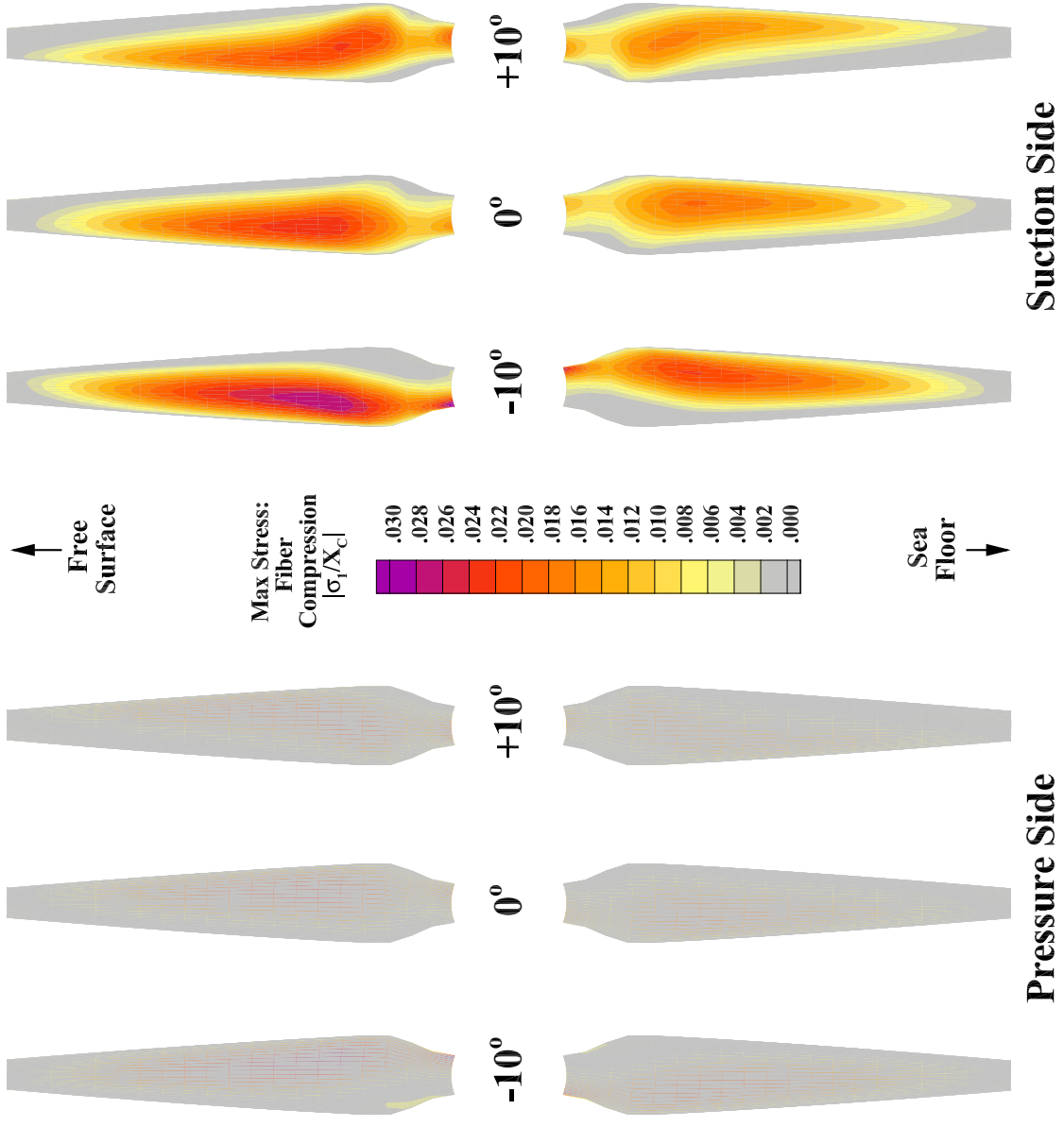
Figure 4.10: Predicted fiber maximum compression stress failure indices ($|\sigma_1/X_C|$) in two adaptive blade turbines and a non-adaptive reference system at $U = 2.0$ m/s and $\lambda = 7$. Both the pressure (left) and suction (right) sides of the blades are shown.
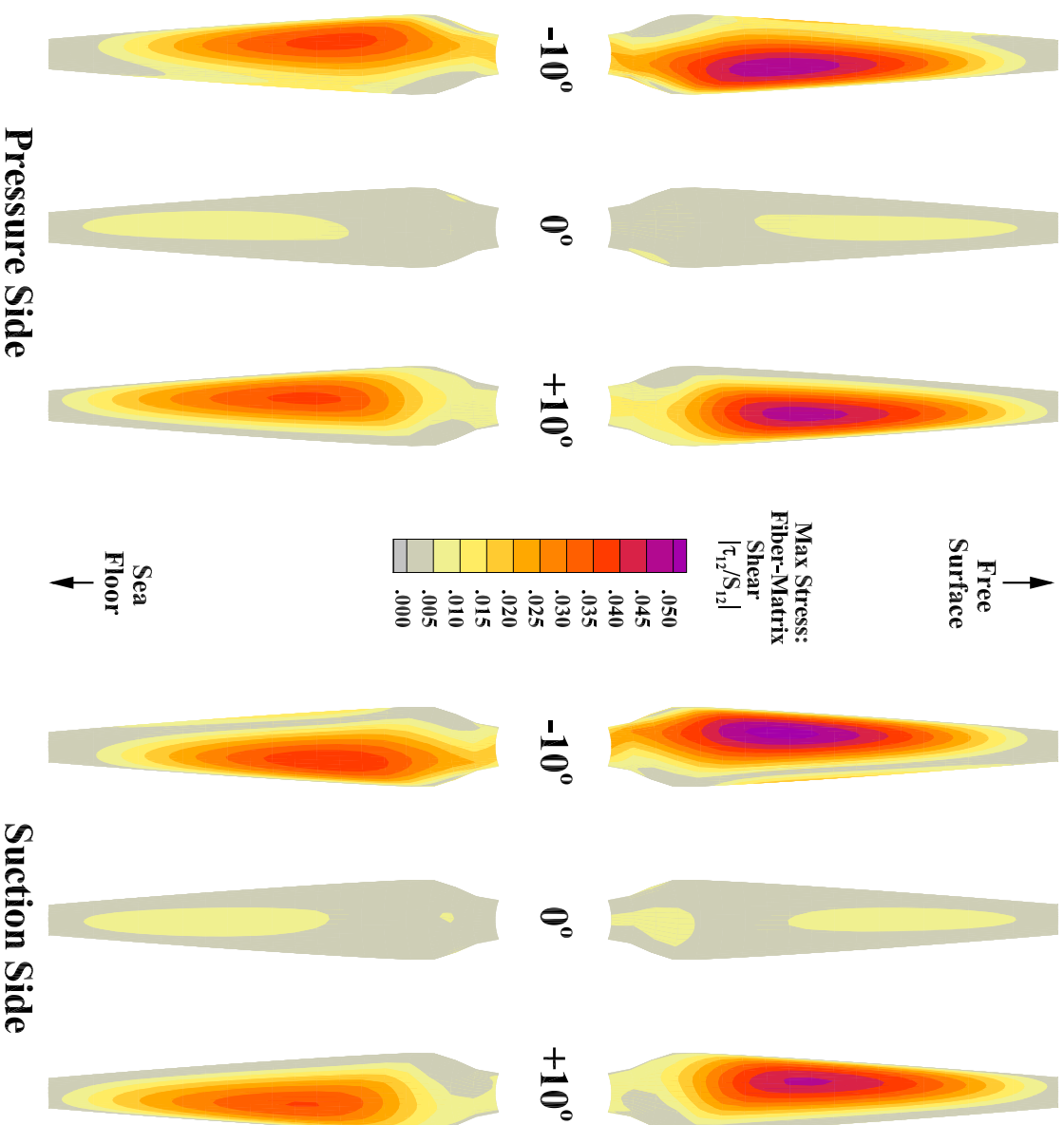
Figure 4.11: Predicted fiber-matrix maximum shear stress failure indices ($|\tau_{12}/S_{12}|$) in two adaptive blade turbines and a non-adaptive reference system at $U = 2.0$ m/s and $\lambda = 7$. Both the pressure (left) and suction (right) sides of the blades are shown.

Chapter 5

PERFORMANCE AND RESPONSE IN CAVITATING CONDITIONS

The presence of cavitation can drastically affect the normal performance and response of marine turbines as presented in Chapter 4. Previous research suggests that adaptive blades can be used in hydrofoils and marine propellers to reduce the susceptibility to cavitation; however, this has not yet been fully explored for marine turbine systems.

Every marine structure that moves at a high velocity relative to the incident flow is at risk of cavitation. In accordance with Bernoulli's principle, an increase in the velocity of a fluid will cause a decrease in pressure. When the pressure in the flow falls below that of the vapor pressure of the fluid, vapor bubbles form and collapse at a high rate. Cavitation contributes to pitting, corrosion, vibration, and fatigue in many marine structures[60]. Preliminary studies have indicated that the use of bend-twist coupled composite material could reduce cavitation on hydrofoils [43]. In research on marine propellers, numerical and experimental results have shown that adaptive composite propellers can provide improved cavitation performance and increased energy efficiency over their non-adaptive counterparts when operating at off-design conditions or in spatially varying flows[84, 117, 118].

5.1 Effects of Cavitation

Cavitation susceptibility is a major limiting criterion in modern marine turbine design. Research has shown that cavitation contributes to pitting, corrosion, vibration, and fatigue of marine structures [5, 112]. Additionally, the vibration caused by cavitation dramatically increases noise generation, a particular concern of turbine systems located in or near sensitive marine mammal habitats. Cavitation can be a function of high relative mean inflow velocities, but can also be initiated or exacerbated by turbulent fluctuations or wave orbital velocities.

The onset of cavitation also has a drastic effect on the power generation of the system.

In general, the lift and drag coefficients of a hydrofoil do not vary as the ambient pressure decreases; the pressures on the upper and lower surfaces decrease in tandem. However, as cavitation develops along the top of the foil, the pressure on the top surface can no longer decrease because it is limited by the vapor pressure. The pressure on the bottom surface is not restricted, however, and continues to fall, progressively approaching the pressure on the top of the foil. As the pressure differential across the foil decreases, there is a corresponding decrease in the lift coefficient. Additionally, the flow separation induced by cavitation changes the shape of the pressure distribution along the foil and causes an increase in drag. Thus, cavitation causes both a decrease in lift and an increase in drag, limiting the power generation as well as exacerbating the loads on the system.

Reducing cavitation susceptibility would allow marine turbines to operate more efficiently. The turbine performance and structural system would be more robust in conditions of increased turbulence or significant wave orbital velocities. Additionally, the maximum rotational speed of the turbine rotor is limited by the pressure reduction caused by the speed of the blade tips. In raising that limit, a turbine could operate at a higher tip speed ratio ($\lambda = \pi n D / U$, where n is the rotational speed in rps). This would provide a larger window for the turbine to operate at maximum efficiency. Furthermore, a reduction in cavitation susceptibility would allow the installation of turbine arrays in shallower waters where the ambient pressure in the fluid is lower. This would drastically expand the number of possible sites for tidal power generation as well as moderate the cost of installation and implementation, as power transfer cables could be shorter and the systems would be more accessible for maintenance.

In general, cavitation resistant blades would be more robust, experiencing less vibration, pitting, and fatigue loading. A decrease in cavitation susceptibility could reduce the limits on depth and maximum rotational speed that are in place for non-adaptive blades, and increase the system robustness in response to large fluctuations in the mean inflow velocity. For these reasons, it is essential to include the study of cavitation in the analysis and development of MHK systems. Though the effects of cavitation have been studied on other marine structures, little research has been conducted on the possible impact of cavitation on an MHK turbine blade. Understanding the structural response of a cavitating blade

is essential to predicting system fatigue life and the susceptibility of the blade to various failure modes.

5.2 Cavitation Prediction

The BEM used for adaptive blade analysis in this work also predicts the presence of sheet cavitation. Because it is a potential-based code, this method cannot fully account for viscous effects such as tip vortices and cavitation collapse; however, it is able to model mid-chord and tip cavitation on both the pressure and suction sides of a blade. This method of sheet cavitation prediction has been extensively validated against experimental results for rigid and adaptive marine propellers and rigid turbine blades [57, 58, 117–119, 130].

For the purposes of cavitation prediction and analysis, the BEM defines a pressure coefficient relative to the local flow,

$$-C_{pr} = \frac{P_0 - P_t}{\frac{1}{2}\rho n^2 D^2} \qquad (5.1)$$

where P_0 is the freestream pressure, P_t is the total pressure at the point in question, ρ is the fluid density, n is the rotational speed, and D is the turbine diameter. The local velocity squared term $n^2 D^2$ is used instead of the more common freestream velocity squared as it typically dominates at higher tip speed ratios. The use of the local velocitiy term also facilitates a direct comparison with the cavitation number,

$$\sigma_n = \frac{P_0 - P_v}{\frac{1}{2}\rho n^2 D^2} \qquad (5.2)$$

where P_v is the saturated vapor pressure in the fluid. Thus, if at any point the pressure coefficient C_{pr} falls below the cavitation number σ_n, the potential for cavitation development exists.

To determine the existence and extent of the potential cavity at each step, a Newton-Raphson iteration is used until the cavity closure condition (cavity height $= 0$ at trailing

edge) is satisfied. Dynamic and kinematic boundary conditions are applied to the cavitating and wetted surfaces to uniquely define the perturbation potential, and the analysis proceeds as described above. This process is described in depth in [58, 118, 119].

5.3   Cavitation Inception and Distribution

To begin a study of cavitation, it is logical to start with an investigation into the conditions at which the onset of cavitation occurs. In this study, three pitch to stall blades ($\theta_{eq} < 0°$) and three pitch to feather blades ($\theta_{eq} > 0°$) with increasing levels of flexibility are compared to a non-adaptive ($\theta_{eq} = 0°$) reference blade. The higher end of the velocity spectrum discussed previously is examined to predict the potential for cavitation inception on each blade. The tip speed ratio for all the following analyses is held constant at 7 in accordance with the optimal operating point found in [19].

Figure 5.1 shows the change of pitch for each blade as a function of velocity, with indications marking cavitating conditions. The blades experienced pitch change as designed, though the reference blade exhibited a minor degree of feathering due to the inherent flexibility in the material and pitch bias of the geometry. The effect of blade fiber angle on the onset of cavitating conditions is clear in this figure; the blades with a pitch to stall bias show cavitation at lower velocities than the reference blade, while the pitch to feather blades delay cavitation. This trend is strongest in the blades with the largest adaptive biases. After the onset of cavitating conditions, the blades tend to experience an increase in the rate of pitch change. This is likely due to the increased forces associated with cavitation.

Figure 5.2 shows the pressure distribution and presence of cavitation on the pressure and suction sides of a single blade as it rotates. The particular blade shown in this figure is the 0° reference blade at an inflow velocity $U = 3.0$ m/s, which is well representative of any moderately cavitating blade in this study. The onset of cavitation appears on the suction side of the blade as expected, initially at the point of the blade's rotation nearest the free surface, where the fluid flow is strongest and the surrounding pressure is lowest. As cavitation progresses, it begins to spread and appear throughout the upper half of the rotational sweep of the blade as shown in Figure 5.2; however, due to the pressure and velocity differentials between the extreme blade positions, at no point is it possible for the
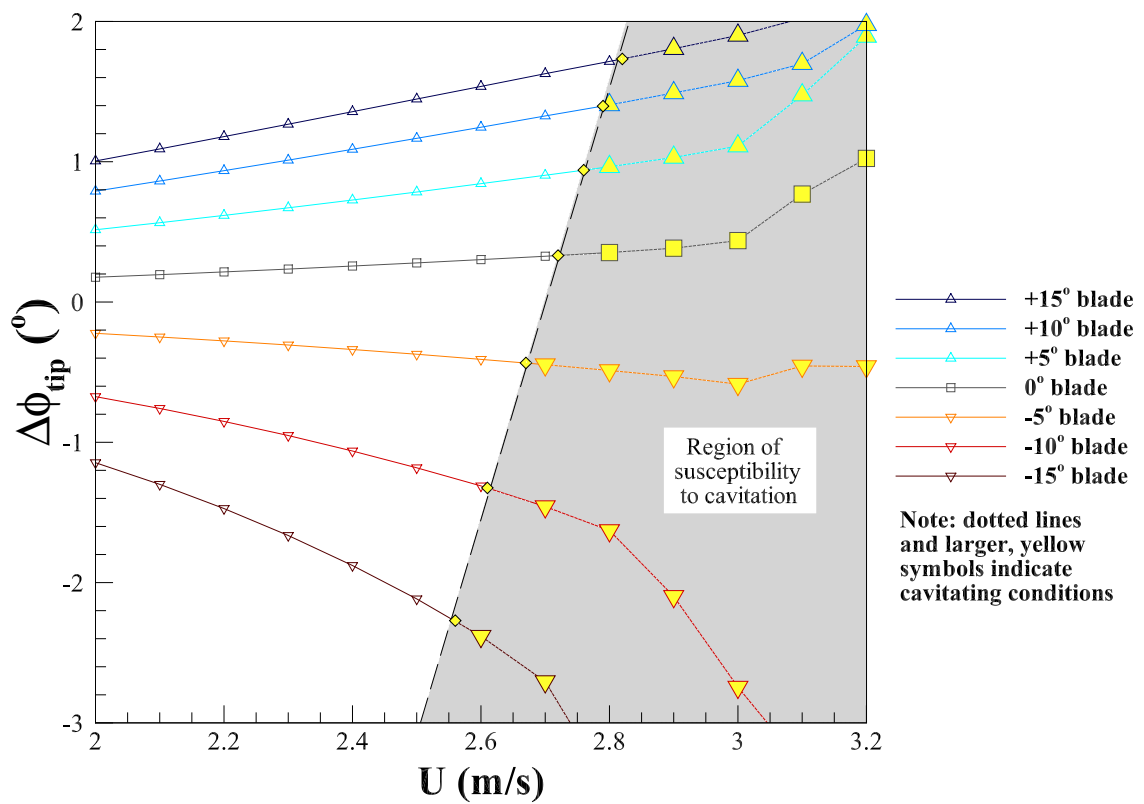
Figure 5.1: Predicted change in pitch for six adaptive blades compared to a non-adaptive reference blade at $\lambda = 7$. The presence of cavitating conditions is indicated with larger, yellow-filled symbols and dotted lines.

cavitating volume to be constant around a full revolution. Thus, as the blade advances, cavitation forms and disappears in each rotation, causing a periodic and unbalanced loading.

This periodic effect, as well as the significance of the increased rate of pitch change under cavitating conditions, can be seen clearly in Figure 5.3. This figure shows the volume of cavitation on the reference and adaptive blades during a full revolution from $U = 2.7$ m/s to $U = 3.0$ m/s. Here the cavitation volume is normalized by the turbine radius R^3.

As the inflow velocity increases, cavitation forms and grows on each blade. The blades with a pitch to stall bias are the first to experience cavitation, with the largest bias blades showing the greatest cavitation volume. This is consistent with the onset of cavitating conditions shown in Figure 5.1. The cavitation volume on these blades grows dramatically with a small increase in velocity, due to the increasing rate of pitch change shown above. The pitch to feather blades, however, delay cavitation compared to the pitch to stall and reference blades. The feathering blades show both a volume reduction and substantially slower cavitation growth compared to the other blades, as the increased rate of pitch change reduces the angle of attack significantly. Again, the benefit is greatest in the blades with the largest adaptive bias.

It is also possible to compare the extent of the revolution of each blade for which cavitation is apparent. At the onset of cavitation, the cavity volume is visible only around the top of the blade's rotation. For blades operating at a more advanced state of cavitation, cavitation is apparent through more than half of the rotation. In all cases shown, the bottom of the revolution, nearest the sea floor, is free of cavitation.

5.4 Structural Response of a Cavitating Blade

The onset of cavitation has a strong impact on blade forces and therefore deformation. For a more detailed analysis of structural response, this section focuses on two adaptive blades ($\theta_{eq} = \pm5°$) and the reference blade ($\theta_{eq} = 0°$). The fluctuation of forces on the system in cavitating conditions can be seen in the unsteady nature of the thrust coefficient (C_T), shown in Figure 5.4. At $U = 2.7$ m/s, the $-5°$ blade has just entered cavitating conditions. There is very slight unsteadiness evidenced in the C_T at that inflow velocity, but in general the C_T curves for all three blades are smooth. At $U = 2.9$ m/s, however, there are large
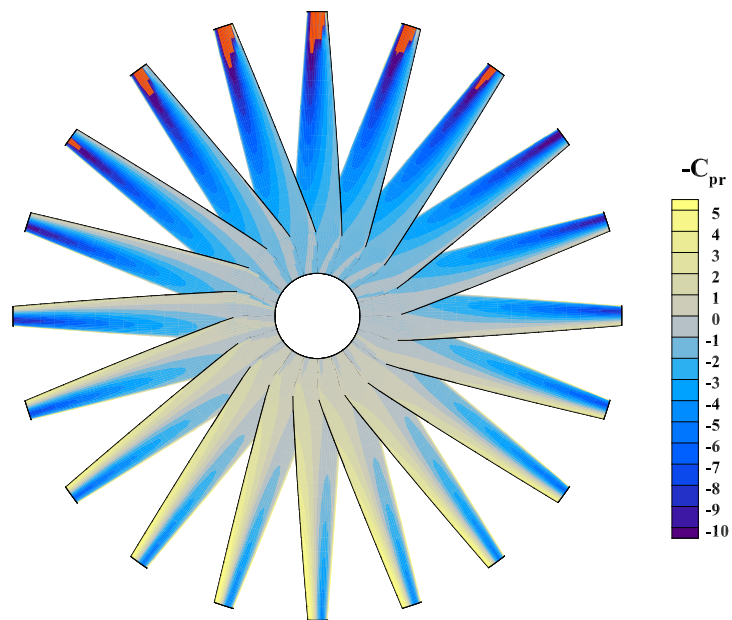
(a) Suction (downstream) side
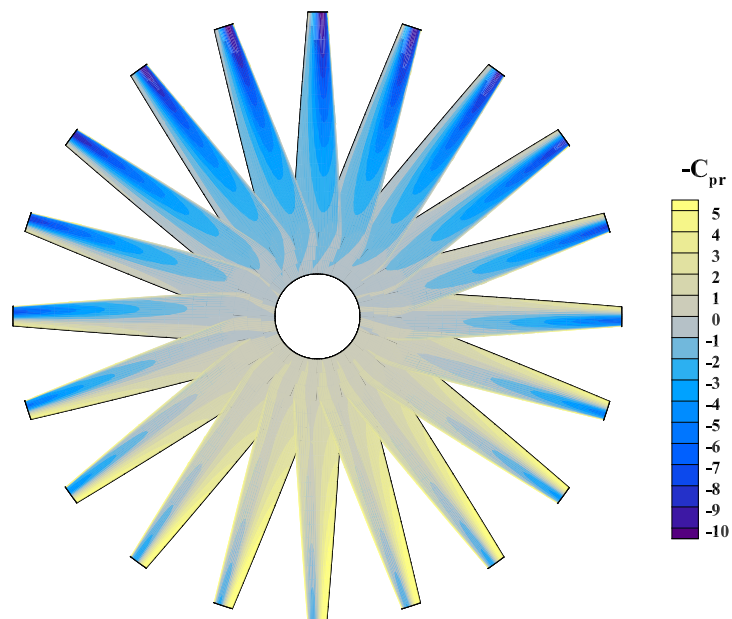
(b) Pressure (upstream) side

Figure 5.2: Pressure distribution and presence of cavitation (shown in red) on the reference blade for one full rotation at $U = 3.0$ m/s.
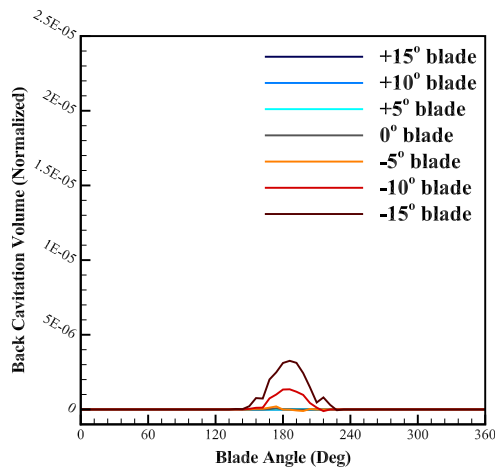
(a) $U = 2.7$ m/s
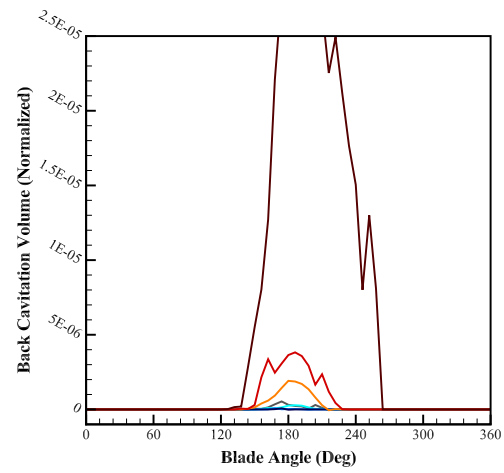
(b) $U = 2.8$ m/s
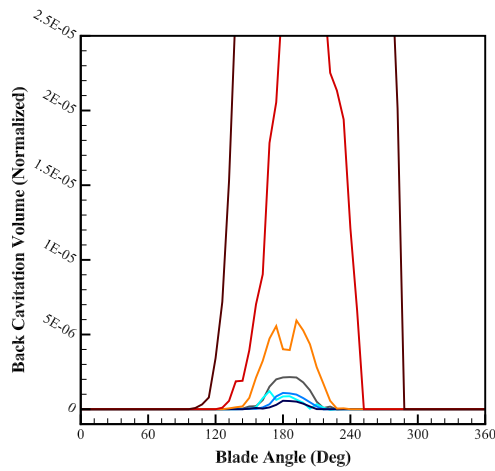
(c) $U = 2.9$ m/s
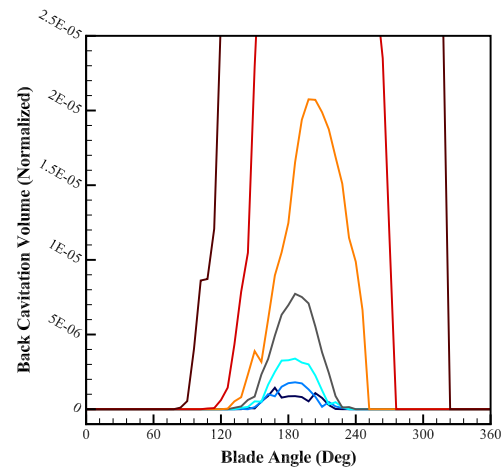
(d) $U = 3.0$ m/s

Figure 5.3: Cavitation volume normalized by turbine radius R^3 over one full rotation at increasing inflow velocities.

fluctuations in the C_T for the $-5°$ pitch to stall blade, and unsteadiness in all three blades. The $+5°$ pitch to feather blade has the smoothest C_T profile of the three, corresponding to the minimal cavitation volume shown in Figure 5.3.

The effect of these fluctuating forces can be seen in the maximum tip displacement of each blade, shown in Figure 5.5. The magnitude of the displacement in both adaptive blades is higher than that of the reference blade, with the pitch to stall blade undergoing moderately larger deformations than the feathering blade. This result is consistent with earlier findings and is due to the fact that the pitch to stall blade experiences slightly higher forces than the feathering blade. The notable feature of these figures is the difference that the onset of cavitation creates. At $U = 2.7$ m/s, the $0°$ and $+5°$ blades are fully wetted while the $-5°$ blade has just entered cavitating conditions. The smooth lines in the wetted blade profiles show the gradual change in blade deformation brought on by the rotation though a nonuniform velocity profile, while the pitch to stall blade shows the effects of cavitation inception in very small oscillations in the displacement curve. As the fluid velocity is increased to $U = 2.9$ m/s, cavitation is apparent on all three blades. The feathering blade is only just beyond the onset of cavitation and shows small oscillations similar to the pitch to stall blade at $U = 2.7$ m/s. However, the other two blades show more significant cavitation and experience strongly unsteady displacements. These fluctuating effects in the blade displacements will increase the rate of fatigue on the system and could lead to unanticipated failures if proper cavitation analysis is not included in the design process.

The structural effects of fluttering caused by cavitation can also be seen in a harmonic analysis. Both the individual blade harmonics (defined with respect to blade-fixed coordinates) and the shaft, or full system, harmonics (in global coordinates) for the reference blade and the two adaptive pitch blades at $U = 2.7$ m/s and 2.9 m/s are presented in this section. For ease of comparison, the magnitudes of the harmonic excitation are normalized by the amplitude of the 0th harmonic. The harmonics for a fully-wetted analysis are compared to those found by the cavitating analysis in each figure for reference.

The axial force blade harmonics are shown in Figure 5.6. At the lower inflow velocity $U = 2.7$ m/s, low level excitation is found for the $-5°$ blade in the higher harmonic modes,
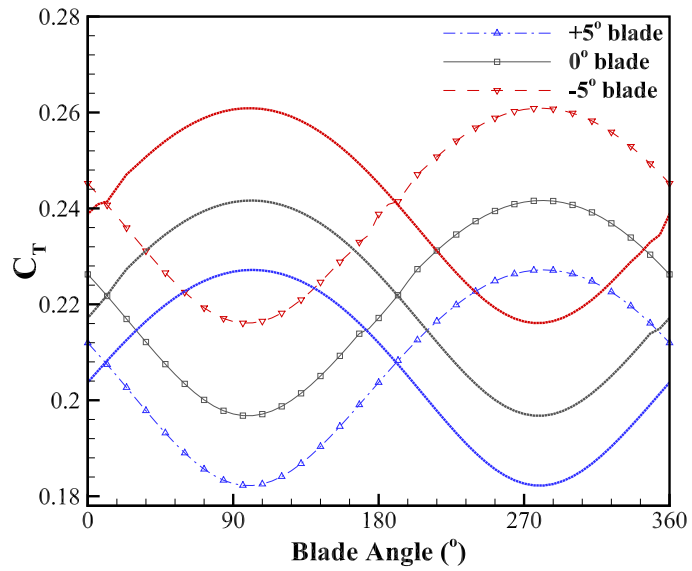
(a) $U = 2.7$ m/s
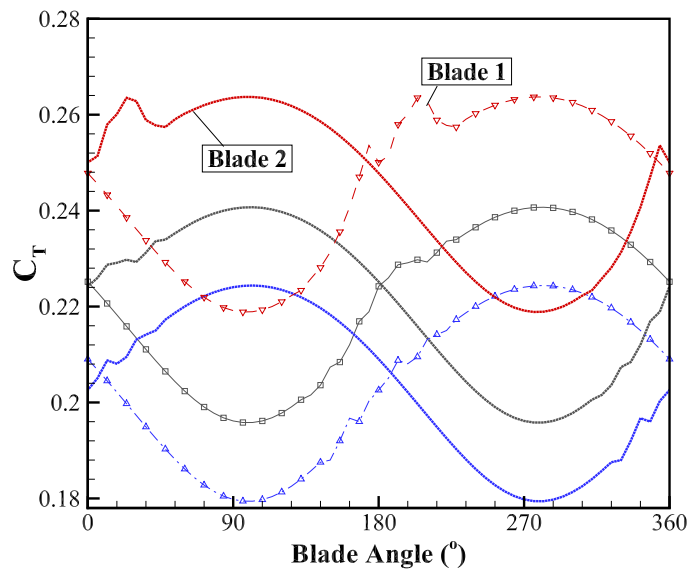
(b) $U = 2.9$ m/s

Figure 5.4: Predicted thrust coefficient on each blade over one full rotation.

67
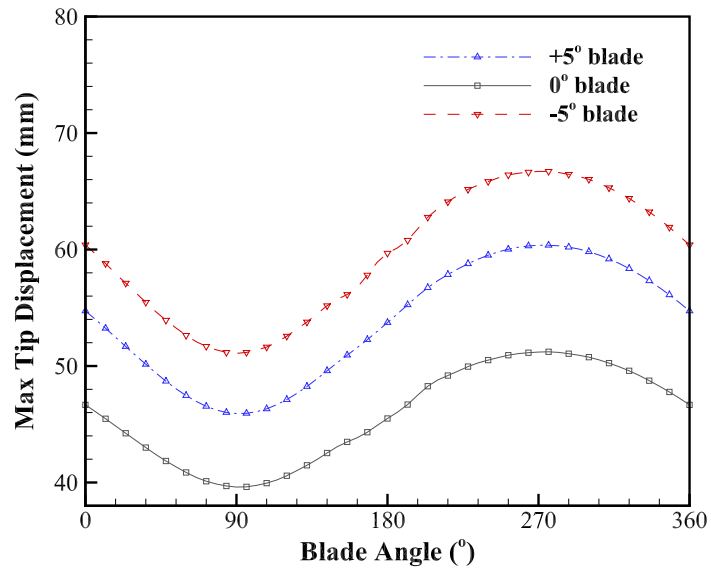
(a) $U = 2.7$ m/s
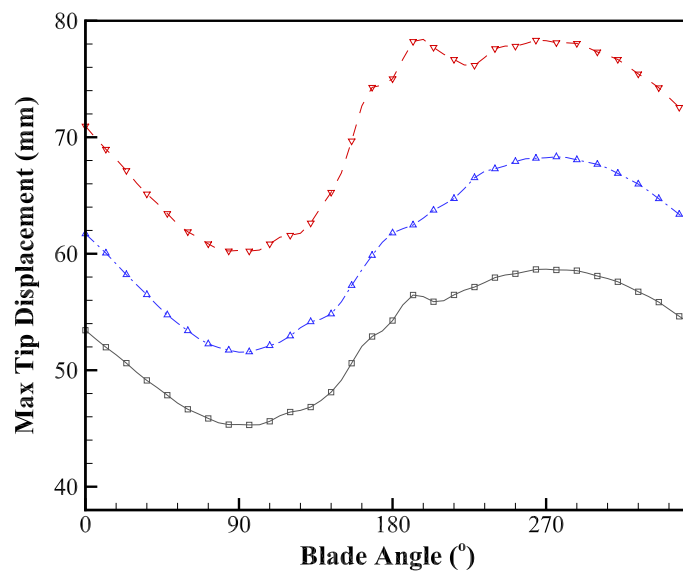
(b) $U = 2.9$ m/s

Figure 5.5: Predicted maximum displacement of each blade tip over one full rotation.

reflecting the onset of cavitating conditions. Very slight excitation is also found in the mid-level modes for the 0° reference blade; this likely reflects the imminent onset of cavitation for that blade. At $U = 2.9$ m/s, excitation is found in the higher modes of all three blades in the cavitation analysis that can not be seen in the simple wetted analysis. The +5° feathering blade is shown to perform significantly better than both the reference and pitch to stall blades, in that it experiences much less excitation of the higher harmonic modes. This reflects the lower volume of cavitation activity on the blade (as shown in Figure 5.3).

The same pattern can be seen in the harmonics due to the moment on the blade, shown in Figure 5.7. The high mode excitation is slightly stronger in this figure, due to the twisting nature of the blade. Again, solely the cavitating blades show high mode excitation. Similarly, Figure 5.8 shows the harmonic response on the full system due to torque. The higher-mode excitation due to cavitation is significantly greater here than in the single blade analysis, due to the fact that cavitation is initiating and disappearing as each blade nears and passes the apex of its rotation, creating an uneven forcing on the system. In this figure, as in Figs. 5.6 and 5.7, the pitch to feather blade shows much weaker excitation in the higher modes for both the blade and shaft harmonics. It is essential to identify these high-frequency harmonic excitations induced by cavitation, as they contribute to blade and system fatigue over the lifetime of a turbine.
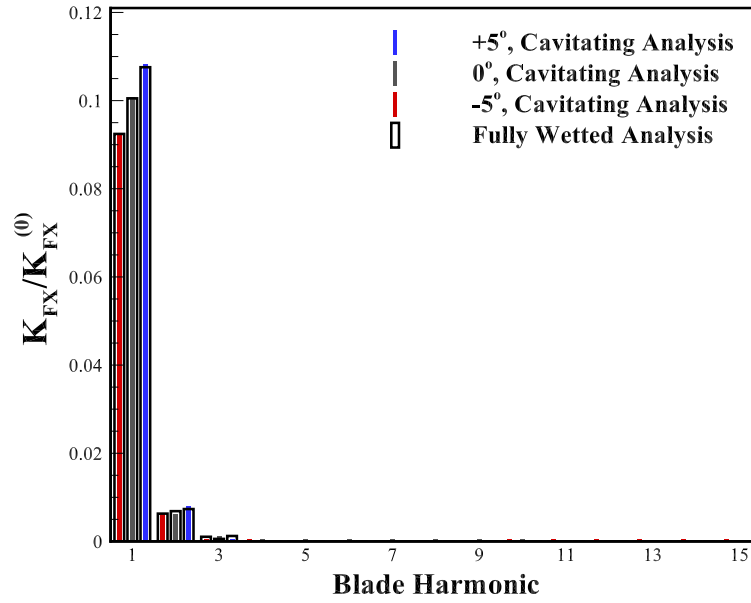
(a) $U = 2.7$ m/s
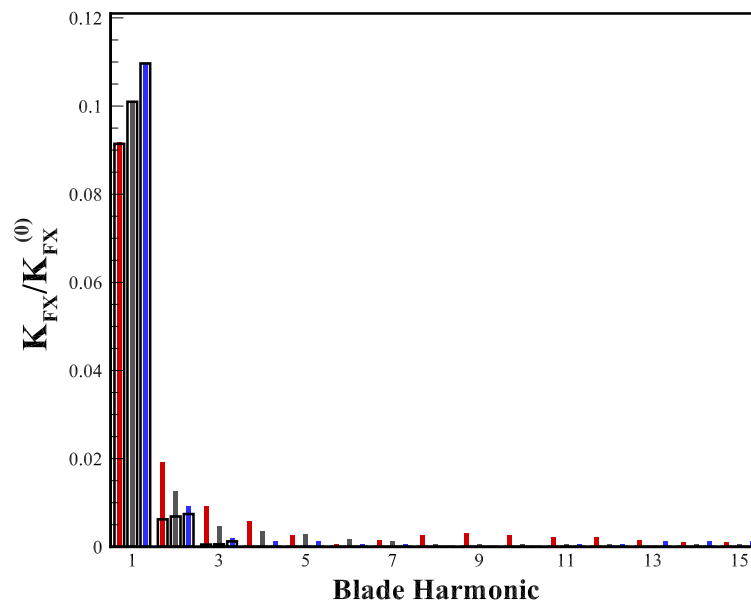
(b) $U = 2.9$ m/s

Figure 5.6: Harmonic excitation in the blade due to axial forces, normalized by the 0th harmonic amplitude.
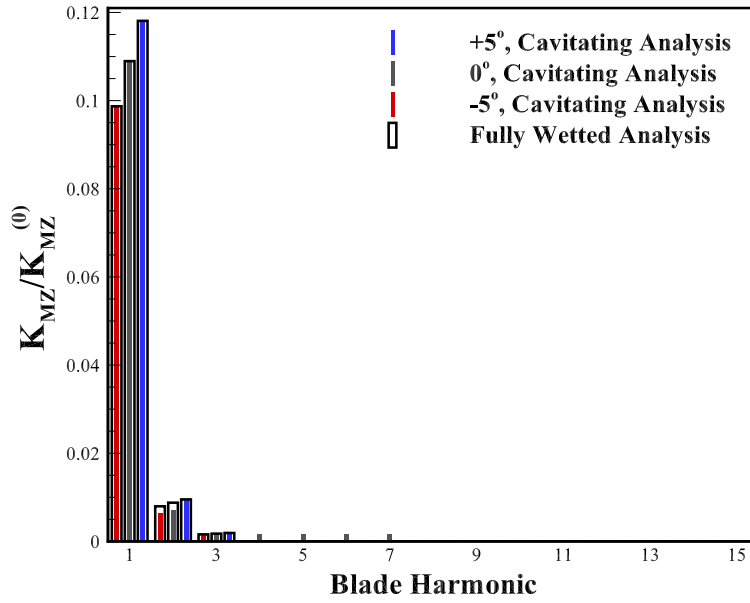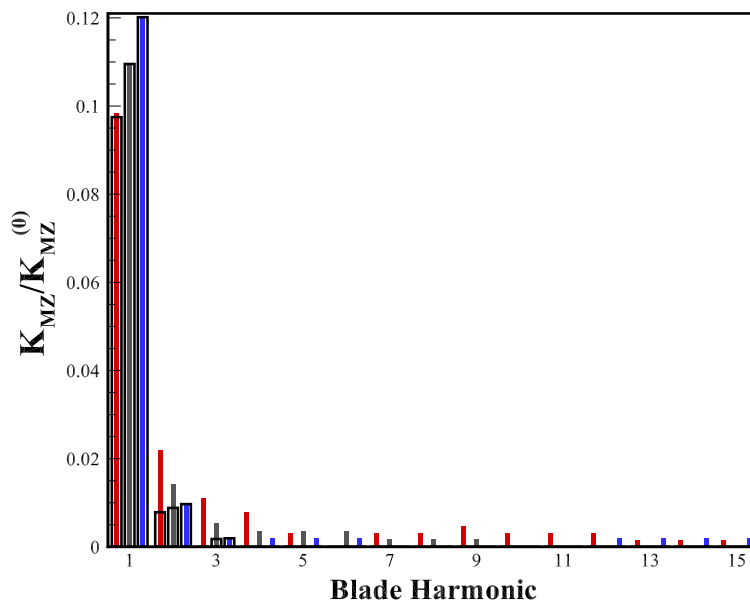
(a) $U = 2.7$ m/s

(b) $U = 2.9$ m/s

Figure 5.7: Harmonic excitation in the blade due to moment forces, normalized by the 0th harmonic amplitude.
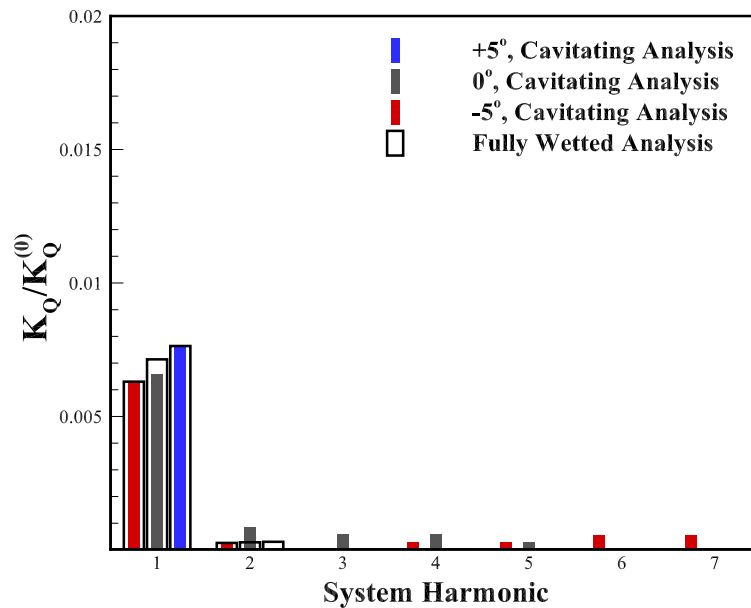
(a) $U = 2.7$ m/s
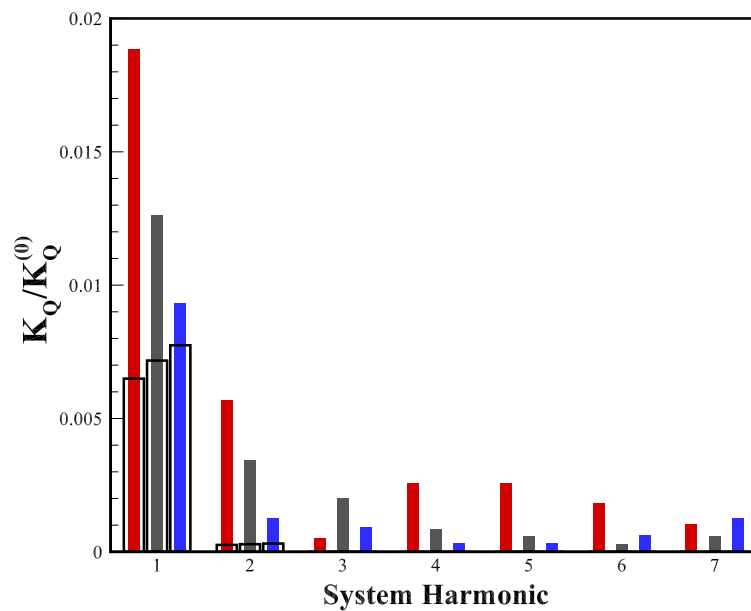
(b) $U = 2.9$ m/s

Figure 5.8: Harmonic excitation in the system due to torque, normalized by the 0th harmonic amplitude.

Though the high-frequency harmonics are a concern in terms of blade and system fatigue, they are not likely to cause resonance in the system. Table 5.1 shows the associated modal frequencies for the first five modes in each blade. These frequencies are much higher than the rate of rotation; at $U = 3.0$ m/s, the turbine is rotating at 0.334 cycles/s.

Table 5.1: Modal Frequencies (Hz).

Mode	$\theta_{eq} = -5°$	$\theta_{eq} = 0°$	$\theta_{eq} = +5°$
1	4.9	5.1	4.5
2	15.2	16.1	15.3
3	20.5	19.1	19.9
4	23.4	24.9	24.7
5	26.1	26.0	26.1

Chapter 6

METHODOLOGY: EXPERIMENTAL TESTING

The research described to this point has concentrated on developing a numerical strategy for predicting the performance and structural response of varying adaptive blade designs. The predicted behavior of these designs was compared numerically to a non-adaptive model in normal and cavitating operating conditions, and results suggest that numerous advantages can be obtained with the use of adaptive blades in marine turbines. However, to provide support and validation for these results and a baseline for further numerical studies, experimental evidence is required. To that end, the remaining chapters detail a set of experiments conducted with a flume-scale MHK turbine.

6.1 The Flume-Scale Turbine

The turbine used for these experiments is a three-bladed variable-speed axial-flow turbine with a rotor diameter $d_T = 0.45$ m, shown in Figs. 6.1 and 6.2. This turbine was designed and built by research students and staff at the University of Washington Applied Physics Laboratory and Mechanical Engineering Department. Though the turbine was fitted with the capacity for a variable-pitch control system, such a scheme was not implemented at the time; thus, it was operated throughout the following studies as a fixed-pitch rotor.

The flume-scale turbine was not designed to generate power. Rather, for each operating point the turbine was set to rotate at a defined speed while the loads on the system were measured. By recording the magnitude and direction of the torque on the rotor applied by the flow as well as the flow velocity, the capacity for power generation could be calculated. To simulate the application of generator torque and achieve variable-speed control, an Applied Motion ST10-Q-RE motor drive ran a Parker Automation LV233 stepper motor inside of the turbine nacelle to apply a user-defined continuous and constant rotor angular velocity.

To measure the loads on the turbine system, two separate load cells were employed. A
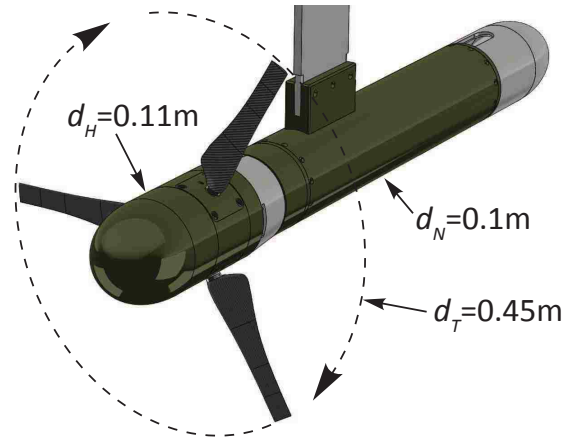
(a) Schematic showing rotor diameter, d_T, hub diameter, d_H, and nacelle diameter, d_N
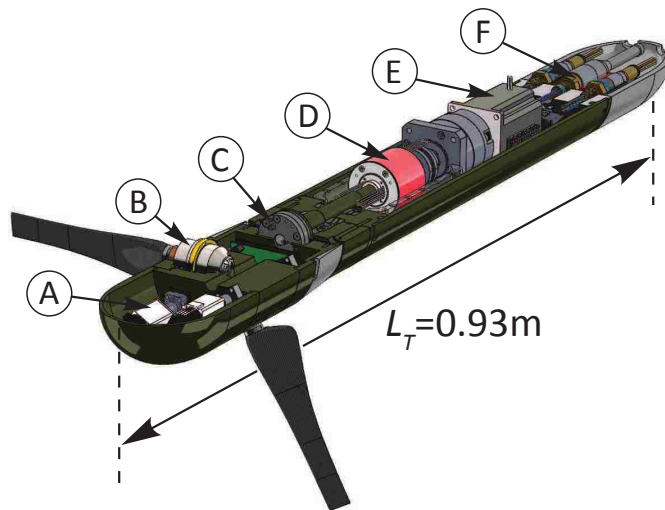
(b) Internal schematic of the turbine: (A) Active blade pitch control motors; (B) Six-axis blade root load cell; (C) Six-axis hub load cell; (D) Slip ring; (E) Rotor speed control motor and encoder; and (F) Communication and data acquisition cables connections

Figure 6.1: Schematics of the axial flow turbine.
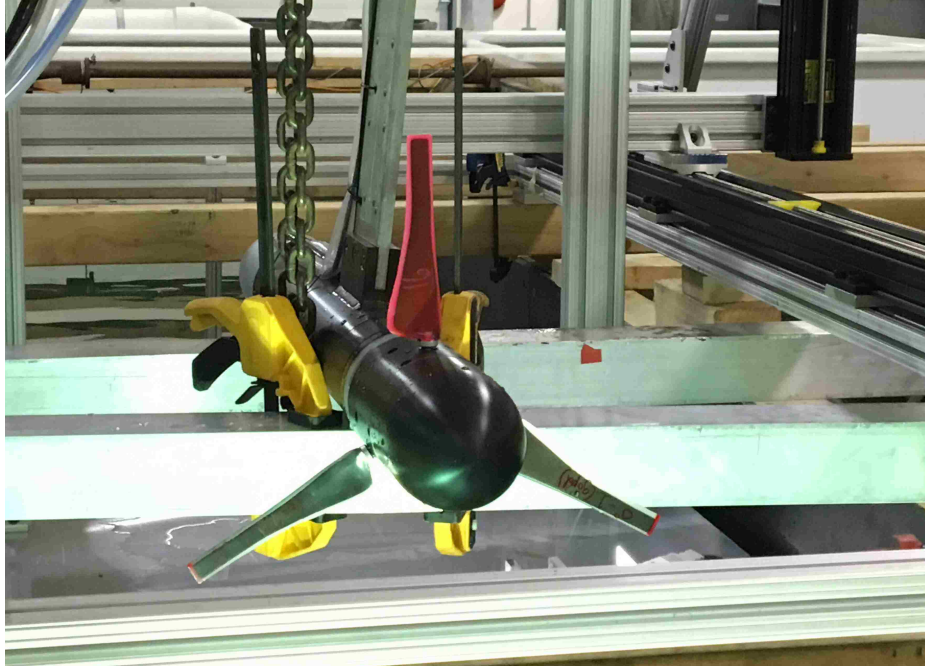
(a) Photo of the flume-scale axial flow turbine, key blade in pink

(b) Photo of the turbine under operating conditions

Figure 6.2: Photos of the axial flow turbine.

76

six-axis ATI Industrial Automation Mini45 load cell provided the connection between the main drive shaft and the hub, enabling instantaneous measurements of rotor forces and moments used to calculate performance characteristics. Inside the rotating hub, a six-axis ATI Industrial Automation Nano25 load cell was mounted to the root of one of the three blades (from here on referred to as the "key blade") to acquire instantaneous measurements of the blade loads and moments. The coordinate systems associated with each load cell are diagrammed in Figure 6.3. To correlate the loads recorded on the key blade with its point in the rotation, blade angular position was measured using an Applied Motion ZAA optical encoder mounted on the main drive shaft.
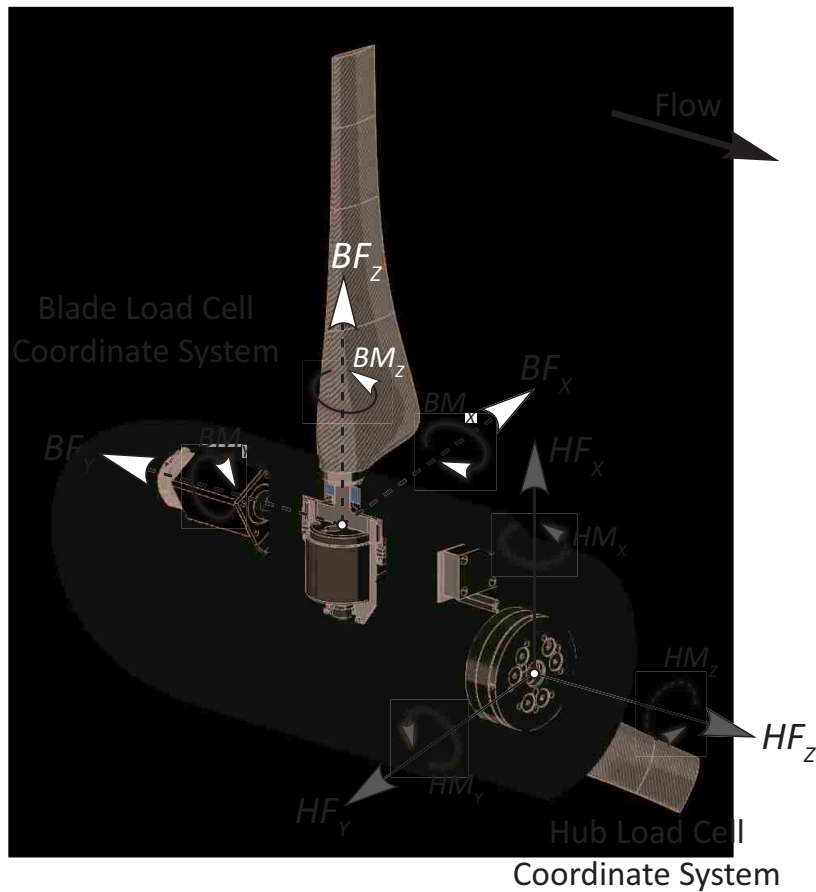
Figure 6.3: Schematic of the blade (BF_{xyz},BM_{xyz}) and hub (HF_{xyz},HM_{xyz}) load cell coordinate systems.

6.2 Uncertainty Analysis

As with any experiment, possible error from several sources contribute to varying amounts of uncertainty in the results. These tests are primarily a comparative study between the behavior of geometrically identical blades under the same hydrodynamic conditions and not intended to provide an accurate prediction of full-scale turbine performance and loads in a realistic deployment; however, it is important to include a discussion of uncertainty for completeness.

Uncertainty analysis for the data collected during these experiments was performed following methods outlined in ASME PTC 19.1-2005 [34]. Total uncertainty for measurements includes both random and systematic uncertainty. Random errors are due to variability in measurements during the length of the data set, typically resulting from natural fluctuations in the measured quantity or electrical noise in the system. Systematic uncertainty is typically provided as calibration data in instrument specification documents from the sensor vendor. To quantify the uncertainty, first the random errors from the data are calculated by finding the standard deviation, s_X, of the sample mean, defined as

$$s_X = \sqrt{\sum_{i=1}^{N} \frac{(X_i - \bar{X})^2}{N - 1}} \tag{6.1}$$

where N is the sample size, $\bar{X}$ is the sample mean, and X_i is each individual sample. To determine the random standard uncertainty, Eq. 6.1 is divided by $\sqrt{N}$.

Systematic uncertainties, or errors that are constant in a measurement, are found using instrument calibration data, shown in Table 6.1. The total uncertainty, $u_{\bar{X}}$, for a measured experimental quantity is defined as

$$u_{\bar{X}} = \sqrt{(b_{\bar{X}})^2 + (s_{\bar{X}})^2} \tag{6.2}$$

where $b_{\bar{X}}$ is the systematic uncertainty from the instrument specifications. For large sample sizes, the total uncertainty can be used to estimate the 95% confidence intervals for the data,

$$U_{\bar{X}} = 2u_{\bar{X}} \tag{6.3}$$

resulting in final measurement mean values with a 95% confidence interval

$$\bar{X} \pm U_{\bar{X}}. \tag{6.4}$$

Experimental quantities are often functions of multiple measured variables, each with their own level of uncertainty due to random and systematic errors. When this occurs, such as in the case of the power coefficient, C_P, or the thrust coefficient, C_T, in these tests, sensitivity of these quantities is determined by

$$\Theta_i = \frac{\partial R}{\partial \bar{X}_i} \tag{6.5}$$

where R is the quantity that is a function of multiple variables (*i.e.*, C_P or C_T), resulting in the absolute random (s_R) and systemic (b_R) uncertainties for a test case defined as

$$s_R = \sqrt{\sum_{i=1}^{I}(\Theta_i s_{\bar{X}_i})^2} \tag{6.6}$$

$$b_R = \sqrt{\sum_{i=1}^{I}(\Theta_i b_{\bar{X}_i})^2} \tag{6.7}$$

and a total uncertainty with 95% confidence intervals

$$U_{R,95} = 2\sqrt{(s_R)^2 + (b_R)^2}. \tag{6.8}$$

For clarity, the 95% confidence intervals are displayed as error bars only on quantities which are functions of multiple variables (*i.e.*, C_P and C_T), as they are in general sufficiently small on individually measured quantities to neglect.

6.3 Blade Design and Fabrication

To fully explore the adaptive pitch effect, two sets of adaptive composite blades were compared to a non-adaptive composite set and a set of aluminum blades. One set of adaptive

Table 6.1: Systemic uncertainties of instruments used.

Instrument	Measured Quantity	Systemic Uncertainty
Nortek Vector ADV	Inflow velocity	0.5%, $\pm 1mm/s$
ATI Industrial Automation Nano25 six-axis force and torque sensor	Blade force and torque	$F_x = 1.25\%$ $F_y = 1.25\%$ $F_z = 1.25\%$ $M_x = 2.00\%$ $M_y = 2.00\%$ $M_z = 1.50\%$
ATI Industrial Automation Mini45 six-axis force and torque sensor	Main rotor shaft force and torque	$F_x = 1.25\%$ $F_y = 1.00\%$ $F_z = 0.75\%$ $M_x = 1.25\%$ $M_y = 1.50\%$ $M_z = 1.25\%$
Applied Motion rotary encoder	Rotor angular position	$\pm 0.045°$
Micro-Epsilon optoNCDT 2300-20 and 1700-500	Static blade displacement	$\pm 1\mu m$

blades was tailored with a pitch to stall bias, such that an increased fluid loading would cause each blade to twist towards stall, decreasing the pitch angle and increasing the effective angle of attack. The other set of adaptive blades was designed to behave in the opposite fashion, pitching to feather and increasing the pitch angle (thus decreasing the angle of attack) under load. The non-adaptive, or neutral, composite blades provided a baseline with identical composite fabrication but no designed material bend-twist coupling. The aluminum set was assumed to be effectively rigid, allowing further comparison between rigid and flexible blades. The tailored bend-twist mechanism in the adaptive models was created solely on the material level; all of the blade sets were designed to identical geometric parameters.

The blade geometry was determined using an optimization routine in the HARP_Opt (Horizontal Axis Rotor Performance Optimization) code developed by the National Renewable Energy Laboratory (NREL). HARP_Opt implements the WT_Perf Blade Element Momentum (BEM) theory to predict rotor performance while iteratively optimizing the hydrodynamic shape of the blade chord lengths, twist, and thickness distributions. Primary input for HARP_Opt includes a distribution of design current velocities and aerodynamic coefficients for the desired blade profiles (i.e. lift, drag, pitching moment, and minimum pressure coefficients). In this case, the system was designed to operate in conditions typical to Puget Sound, WA, as outlined in [82, 102]. As a result, the blade section profiles transition from a circular root at the hub radius ($d_H/2 = 0.055$ m) through a series of NACA-44xx profiles to the tip of the blade ($d_T/2 = 0.225$ m). The blades were aligned at a resting position of $0°$ pitch (i.e. $2.97°$ pre-twist at the tip). The NACA-44 series was chosen because it has been used extensively for marine hydrodynamic turbines due to the benefits of low critical Reynolds number for transition from laminar separation bubble, high lift to drag ratio, large structural rigidity, and acceptable cavitation resistance. See Table 6.2 for full details of the geometry.

Due to the small scale of the blades required for flume-level testing, it was not feasible to lay up an adaptive composite laminate following the complex blade geometry with sufficient accuracy in either the geometry or the fiber orientation. To address this issue, the composite blades were composed of a flat carbon fiber spar, twisted to follow the chord line of the

Table 6.2: Blade geometry, NACA-44xx profiles.

r/R	c/r	t/c	Pre-Twist (°)	r/R	c/r	t/c	Pre-Twist (°)
0.23	0.35	1.00	15.40	0.64	0.18	0.16	6.39
0.24	0.34	1.00	15.40	0.69	0.16	0.15	5.93
0.25	0.36	0.93	15.40	0.73	0.15	0.15	5.51
0.26	0.42	0.86	15.40	0.77	0.14	0.15	5.12
0.27	0.53	0.54	15.40	0.81	0.13	0.15	4.77
0.29	0.66	0.39	15.40	0.84	0.12	0.15	4.44
0.30	0.66	0.28	15.40	0.87	0.12	0.15	4.14
0.32	0.64	0.24	15.40	0.90	0.11	0.15	3.86
0.35	0.57	0.23	15.27	0.93	0.11	0.15	3.62
0.39	0.49	0.21	12.63	0.95	0.11	0.15	3.41
0.43	0.42	0.20	10.73	0.97	0.10	0.15	3.23
0.47	0.35	0.19	9.36	0.98	0.10	0.15	3.10
0.51	0.29	0.18	8.34	0.99	0.10	0.15	3.01
0.56	0.25	0.17	7.55	1.00	0.10	0.15	2.97
0.60	0.21	0.17	6.92				
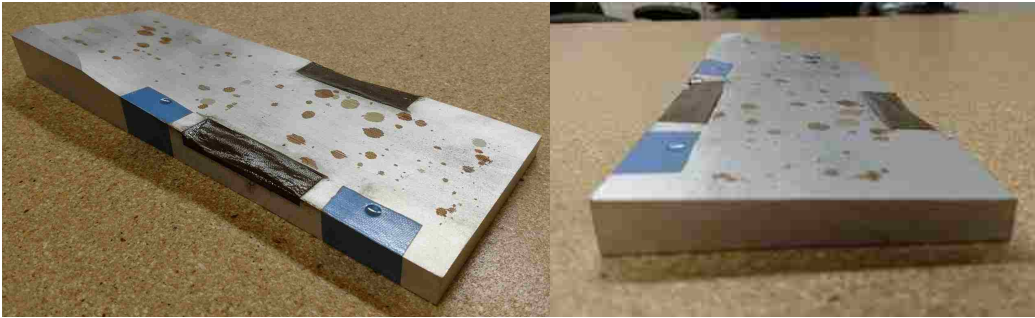
Figure 6.4: Aluminum plate used to tool the blade spars, twisted to follow the blade chord profile.

Figure 6.5: Blade spar with aluminum hub connection.

target blade geometry, and a semi-flexible urethane body cast around the spar to create the hydrodynamic blade shape. The twisted flat plate used for tooling the spars can be seen in Figure 6.4. The hub connection at the blade root was created with an aluminum insert that was attached with epoxy to the blade spar prior to casting the urethane body, as seen in Fig 6.5. The mold used for casting the urethane is shown in Figure 6.6.

The urethane was chosen such that it had adequate hardness to maintain the blade geometry but would not significantly impede the elastic bend-twist deformations. In this way, the adaptive tailoring of the composites could be explicitly controlled in the carbon fiber spar without sacrificing accuracy in the hydrodynamic profile. This fabrication process was used solely for the small-scale blades in this initial test sequence; future work on larger

Figure 6.6: Aluminum mold used to cast the urethane around the blade spar.

scales will use more traditional manufacturing processes.

To design the appropriate composite laminate spars for the adaptive blades, a parametric study in ABAQUS/Standard [1] was conducted. Due to the complex stress distributions within the laminates, composite FRP structural design is often strain- or displacement-based. In this process the blade deflection and twisting response is optimized for a target blade behavior, then a laminate is designed with appropriate stiffness and twist coupling. A target pitch change ($\pm 5°$) and a limit on bending deflection (10% of the blade length) at the design condition were imposed, along with constraints based on the predefined geometry. To design for both twist and deflection, the thickness and fiber angle of the laminate were tailored. Varying the fiber angles of the laminate resulted in an "unbalanced" laminate and induced bend-twist coupling, while laminate thickness was adjusted to meet target deflection goals.

The resulting laminates each consisted of 14 plies of unidirectional IM7/8552 Hexply carbon fiber, resulting in a final spar thickness of 1.43 mm. All plies for the adaptive

Figure 6.7: Composite blade sets; semi-flexible urethane over twisted composite spar.

blades were laid up with a 7° fiber angle offset from the blade axis: +7° for the pitch to feather blades and −7° for the pitch to stall blades. The neutral composite blades were also 14 ply, with the unidirectional fibers aligned with the blade longitudinal axis. Though the coupling between bending and twisting behaviors has been shown to reach a maximum with fiber angles of ≈ 30°, the bending stiffness of composite laminates reduces drastically with fiber angles greater than 10°. With a higher degree of bend-twist coupling, the thickness required of the laminate to limit tip bending deflections would have been greatly increased. Because the thickness of the composite spar was limited by the geometric parameters, less coupling was chosen in order to maintain adequate bending stiffness. The fiber angle offset required for the creation of an adaptive mechanism will always result in reduced stiffness compared to a neutral fiber orientation, however all deflections were within the acceptable range. Properties of all three materials used are shown in Table 6.3. The finished blades are shown in Figure 6.7. For one blade of each design, the clear urethane was dyed pink and designated the "key blade", facilitating visual tracking of the blade mounted to the load cell.

Table 6.3: Properties of materials used for blade fabrication.

Aluminum	Compound: 6061-T6 $\rho = 2700\ kg/m^3$ $E = 68.9$ GPa $G = 26$ GPa $\nu = 0.33$
Carbon Fiber Laminate	Compound: Hexcel IM7/8552 $\rho = 1570\ kg/m^3$ $E_1 = 158$ GPa, $E_2 = E_3 = 8.96$ GPa $G_{12} = G_{13} = 4.69$ GPa, $G_{23} = 3.09$ GPa $\nu_{12} = \nu_{13} = 0.316,\ \nu_{23} = 0.451$
Urethane	Compound: Smooth-Cast 45D $\rho = 1100\ kg/m^3$ Shore Hardness: 45D Elongation at Break: 100%

6.4 Design Validation

Prior to flume testing, static load-deformation tests were performed on each individual blade in order to confirm design goals and behavior predictions. In these tests, the force-deformation relationships of all four blade sets in response to a single point load were calculated. Though in practice the loading profile on a turbine blade is highly complex, these tests provide a baseline performance survey to both confirm design behavior and calibrate future numerical models. Load-deformation testing on the turbine was performed in the structural vibrations laboratory at the University of Washington.

The blades were loaded quasi-statically in the streamwise direction (see Figure 6.3; negative BF_Y direction) using a displacement-controlled method in which a slowly incrementing displacement was applied to the blade tip at the neutral pitch axis. The force-displacement test was repeated three times for each individual blade, and displacement data was used

from the loading period only to avoid capturing any hysteretic behavior in the unloading period. Two lasers, a Micro-Epsilon optoNCDT 2300-20 and a Micro-Epsilon optoNCDT 1700-500, were used to measure deflection of the blades under load. The lasers each captured "streamwise" deflection 163 mm from the blade root ($r/R = 0.96$) at points separated by 14.7 mm along the chord of the blade, as depicted in Figure 6.8. Note that because the deformation in each test was applied at the blade tip and the deflections were measured at $r/R = 0.96$, simple beam theory was used to extrapolate the deflection and twisting responses to the tip. This was determined to be an acceptable approximation due to the small deflections and curvatures. Each individual blade was mounted on the key blade load cell of the turbine for the test, which was used to record forces and moments corresponding to the applied displacement. Measurements from the two lasers and the load cell were synchronized in order to calculate force-deflection, force-twist, and deflection-twist relationships.

Figure 6.9 show the results of a suite of force-deformation tests. Point data from each of three tests conducted on every blade is reported. In Figure 6.9(a), the strongly linear nature of the force-deflection response is clear. Though nonlinear behavior is apparent in deflections under 1 mm, this is likely due to a lack of rigidity in the blade root-to-hub fitting. As expected, the aluminum blades display a nearly rigid behavior, showing maximum deflections on the order of 10% of those measured in the adaptive blades. The adaptive composite blades behave similarly to the neutral design; however, the reduced stiffness that is a function of the adaptive mechanism can clearly be seen. The bending deformation of the pitch to feather and pitch to stall blades is effectively identical. This is to be expected, as the fiber angle offset, and thus stiffness reduction, is the same magnitude in the two blades designs.

The difference in the direction of the fiber angle offset can be seen in the force-twist response, shown in Figure 6.9(b). Though the adaptive blades display very similar behavior in bending, the force-twist responses in the two designs are opposite. The pitch to feather blades show a positive pitch change, while the pitch to stall blades twist in a negative direction. Again, the aluminum blades display effectively rigid behavior, while the neutral composite shows a slight bias towards pitching to feather (increasing pitch). The trends in these results are also linear, though the correlation is less strong than in the force-deflection
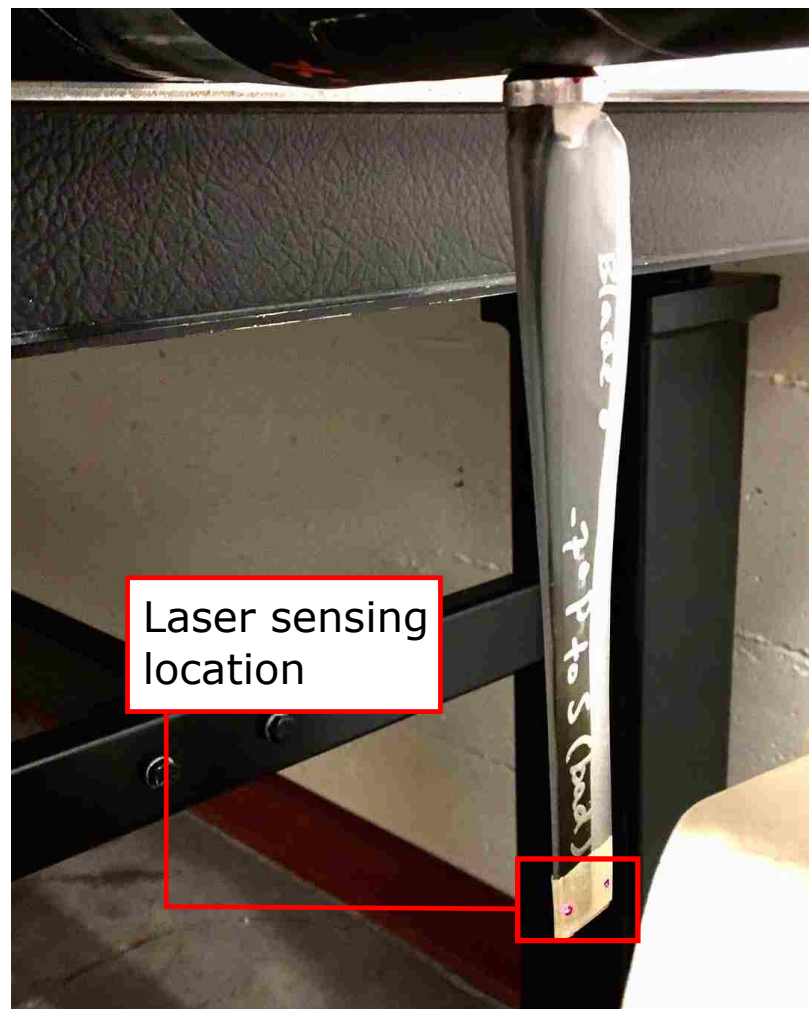
Figure 6.8: Placement of laser sensors on turbine blade for load-deformation tests.

responses. The scatter in Figure 6.9(b) is due to the difficulty in imposing a displacement on the blade tip without influencing the twisting deformations. Though the blades were loaded at a point as close to the neutral pitch axis as possible, any small deviation from that point will have a significant impact on the twist response.

The deflection and pitch change responses shown in Figure 6.9 are combined in Figure 6.10 to show empirical bend-twist relationships. A linear regression for each blade design is plotted for additional clarity. As expected, the bend-twist response of the pitch to feather blades is approximately equal in magnitude (as measured from the neutral pitch behavior)
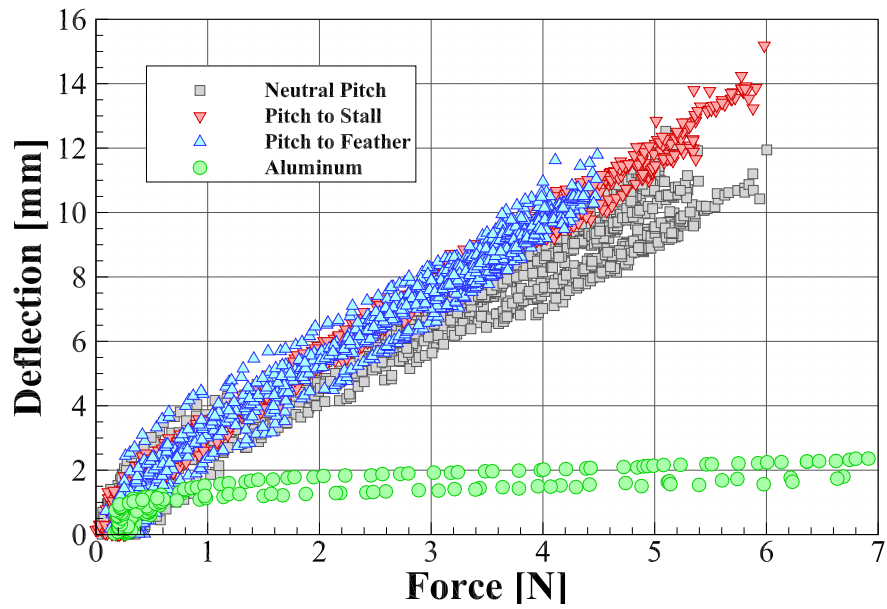
(a) Force-deflection response at blade tip
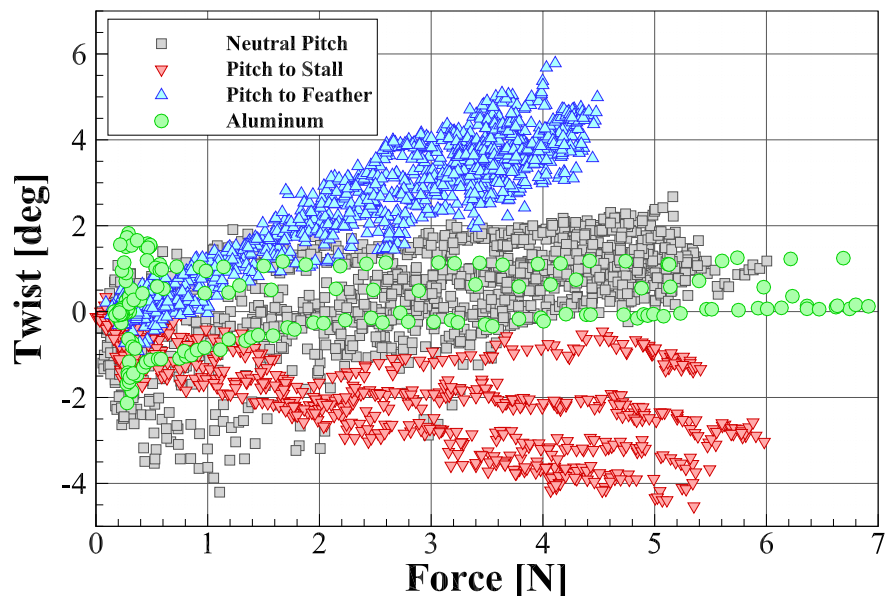
(b) Force-twist response at blade tip

Figure 6.9: Load-dependent elastic deformation responses of each blade type.

and opposite in direction to that of the pitch to stall blades. Though the aluminum blades displayed effectively rigid behavior by neither bending nor twisting to a significant extent, they show the same influence of the slight geometric bias to pitch to feather as the neutral composite blades, a behavior that agrees with previous numerical predictions [82, 83]. However, the correlation of the aluminum bend-twist response especially is quite low, and additional tests are necessary for conclusive results.
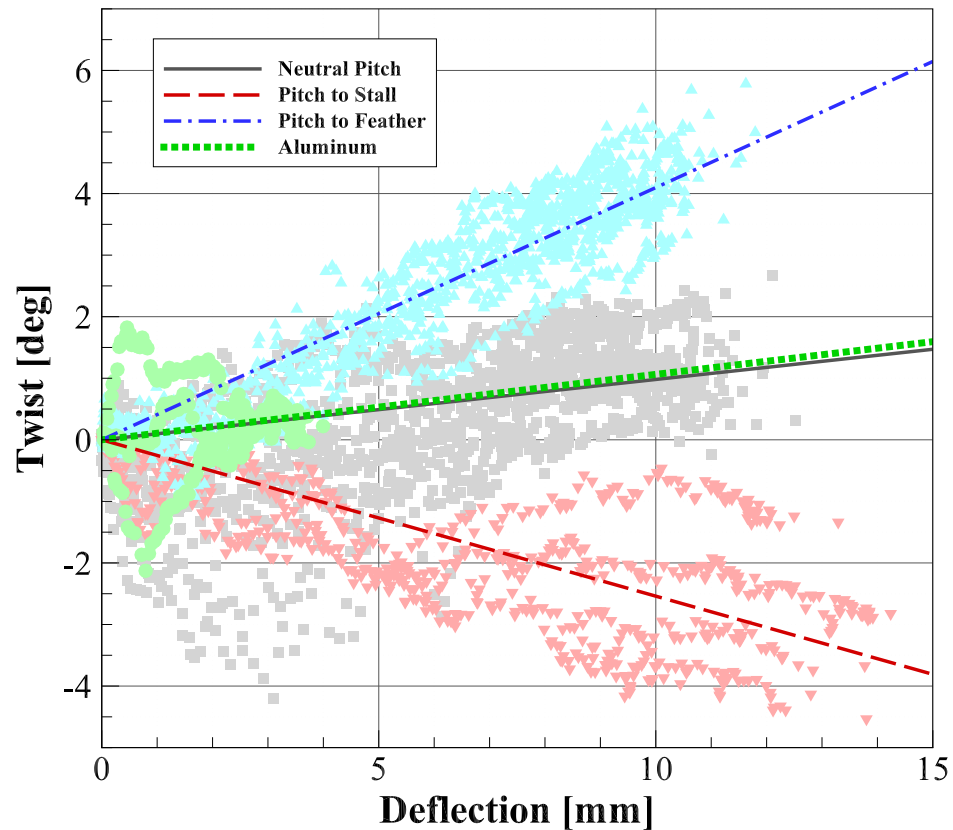
Figure 6.10: Deflection-twist relationship, with linear regression plotted.

In general, the results of the load-deformation tests showed good agreement with design goals and behavior predictions. The pitch to feather blades displayed a bias to increase blade pitch under load, while the pitch to stall design tended to decrease blade pitch. Both adaptive designs were slightly more flexible than the neutral composite, and the assumption

of rigidity for the aluminum blades was shown to be an acceptable approximation. In flume testing, it could thus be expected that the adaptive behaviors will lead to the load control system as predicted; the decrease in blade pitch under load on the pitch to stall design will correspond to an increase in angle of attack and therefore higher load capturing, while in the opposite fashion, the pitch to feather design will experience a decreased angle of attack, shedding the increasing loads.

Chapter 7

FLUME TESTING: STEADY INFLOW

In order to experimentally compare the behavior of the adaptive pitch designs to non-adaptive and rigid blade systems, a series of flume tests were conducted. To gather baseline data, initial observations were collected under steady, uniform flow conditions. In these tests, load data and performance curves were generated for all four blade designs at several inflow velocities.

7.1 Experimental Facility and Procedures

The initial flume experiments were conducted at the Bamfield Marine Sciences Center in Bamfield, BC, Canada. The Bamfield facility includes a recirculating rectangular open channel flume ($b = 0.98$ m, $L = 12$ m). Fluid velocity in the Bamfield flume is controlled by a series of four pumps, allowing for speeds of up to 1.0 m/s. The dynamic water depth and temperature were held constant at $h_d = 0.73$ m and $T = 16°$ C, respectively, for all tests. The turbine was placed near the center of the flume longitudinally, with the hub height, $h_{hub} = 0.375$ m, set to approximately half of the static water depth in the flume.

During flume testing, a Nortek Vector acoustic Doppler velocimeter (ADV) was positioned approximately 1.1m ($\approx 2.5d_T$) upstream of the turbine. The ADV sampled instantaneous three-dimensional inflow velocities at points coinciding with data from the turbine encoder and load cells. From the recorded velocity data, the turbulence intensity in the flume was determined to be around 7-8%; this is consistent with field measurements in Puget Sound and previous flume experiments in the literature, though the distribution of energy with turbulent time scale is somewhat distorted from field observations [102].

Performance curves were generated by holding the fluid velocity constant and varying turbine rotational speed, in order to measure loads over a range of tip speed ratios. Measurements at each point on the performance curve were sampled at ≈ 16 Hz for 2-5 minutes

to ensure steady state operation. Due to the load-dependent nature of the adaptive blades, however, performance is dependent on both velocity and tip speed ratio, as discussed in Section 2.3. Therefore, curves were collected for the adaptive pitch blades at three inflow velocities: $U_{hub} = 0.5$ m/s, 0.65 m/s, and 0.85 m/s, resulting in a range of Reynolds numbers $Re_D = 2.0$-$3.4x10^5$ ($Re_c \approx 0.7$-$1.1x10^5$). For comparison with the composite blades and to investigate effects of Reynolds number dependence, performance curves for the rigid aluminum blades were collected at $U_{hub} = 0.5$ m/s, 0.85 m/s, and 1.0 m/s.

To investigate the performance behavior of the adaptive blades as compared to the non-adaptive and rigid designs, forces and moments on the key blade of each turbine system were recorded during dynamic testing. A 30-second sample of the data output, along with the corresponding velocity measurements, is shown in Fig 7.1. This sample shows the blade forces and moments and components of the fluid velocity recorded on a neutral pitch composite blade system operating at a rotational frequency $f_T = 2$ rps in a flow of $U_{hub} = 0.50$ m/s. Similar force and moment data are gathered from the hub load cell. In the blade load cell, the x-direction points from the leading to the trailing edge of the blade at the $0°$ pitch line, the y-direction points upstream, and the z-direction points out radially along the blade. The coordinate systems for both load cells can also be found in Figure 6.3. The x-direction of the ADV is oriented upstream and the y- and z-directions reflect horizontal and vertical velocities, respectively.

7.2 Dynamic Blade Loading

Using data from the blade load cell and ADV, it is possible to calculate the mean forces and moments on the key blade as a function of tip speed ratio ($\lambda = R\omega/U_{avg}$) for each inflow velocity. This data is presented in Figs. 7.2 and 7.3. The data for the pitch to stall blade design at $U_{hub} = 0.85$ m/s stops at $\lambda = 5.5$ due to blade failure at the following test point ($f_T = 3.75$ rps, $\lambda \approx 6.25$); this is discussed in depth in Section 7.4 below.

Looking at the blade forces and moments in Figs. 7.2 and 7.3, respectively, there are several items of note. First, the neutral pitch (non-adaptive) composite blade and the aluminum blade perform similarly in nearly all respects. The only significant difference between the two is in the z-direction force in Figure 7.2. This is effectively the centripetal
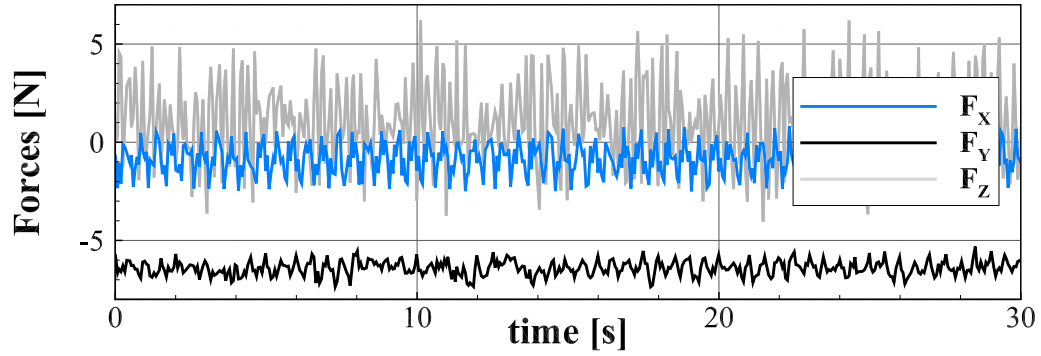
(a) Sample key blade load cell data: Blade forces
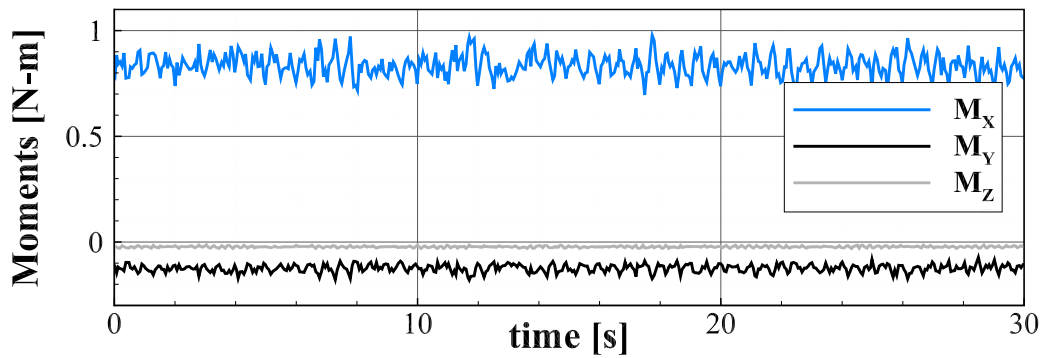
(b) Sample key blade load cell data: Blade moments
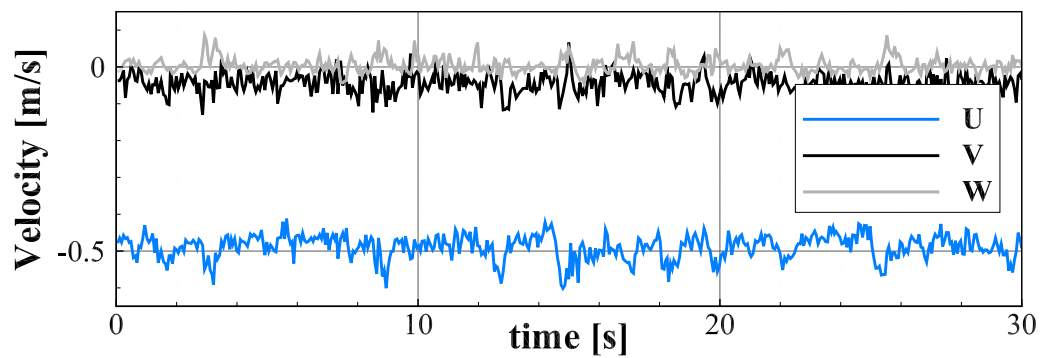
(c) Sample ADV data: Velocity

Figure 7.1: Calibrated data samples from the blade load cell and ADV for the neutral pitch blades at $U_{hub} = 0.50$ m/s, $f_T = 2.0$ rev/s. Refer to the coordinate system shown in Figure 6.3.

(a) $U_{hub} = 0.50$ m/s

(b) $U_{hub} = 0.65$ m/s

(c) $U_{hub} = 0.85$ m/s
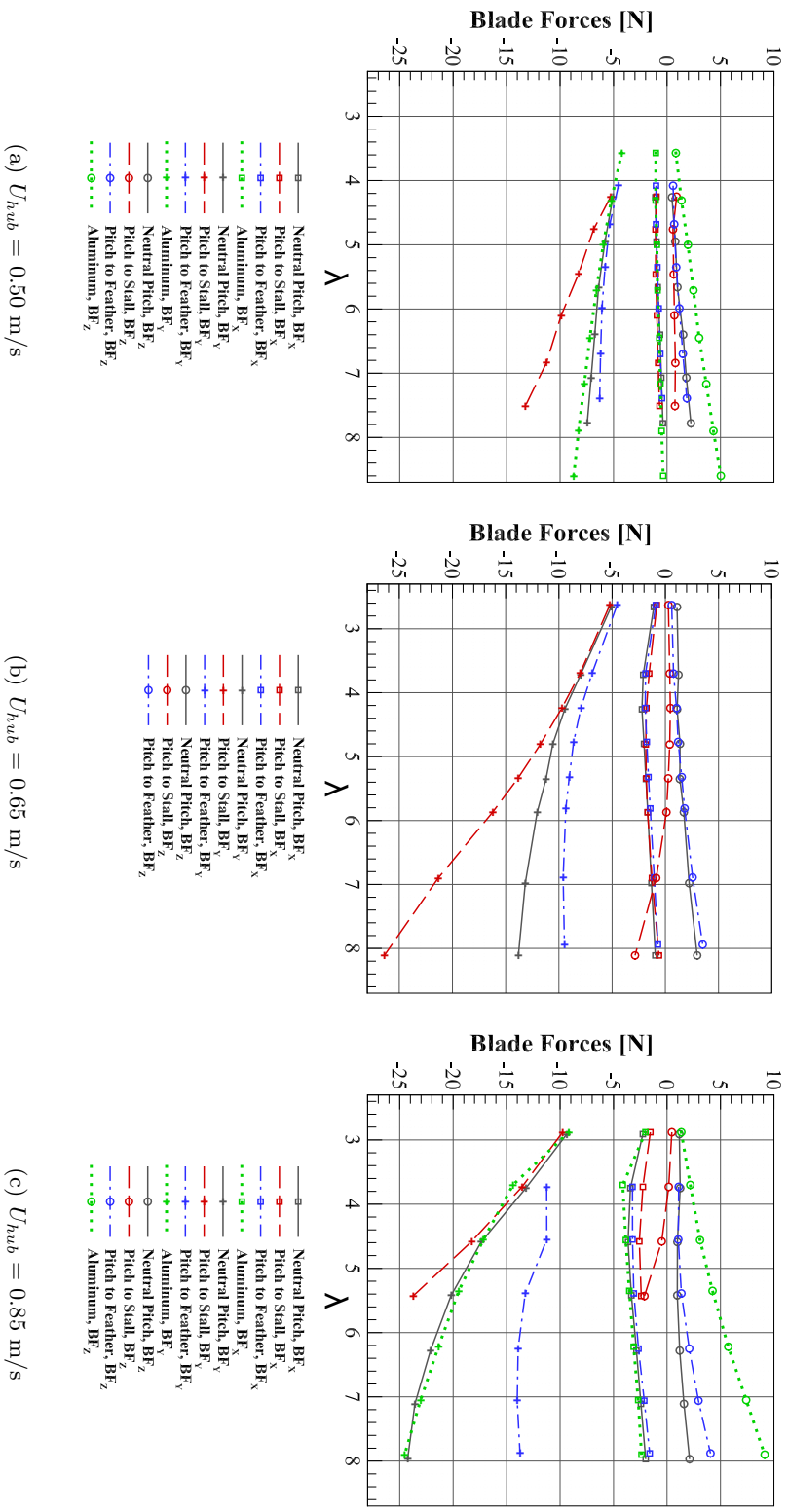
Figure 7.2: Mean forces on the key blade load cell for each inflow velocity.

(a) $U_{hub} = 0.50$ m/s

(b) $U_{hub} = 0.65$ m/s

(c) $U_{hub} = 0.85$ m/s
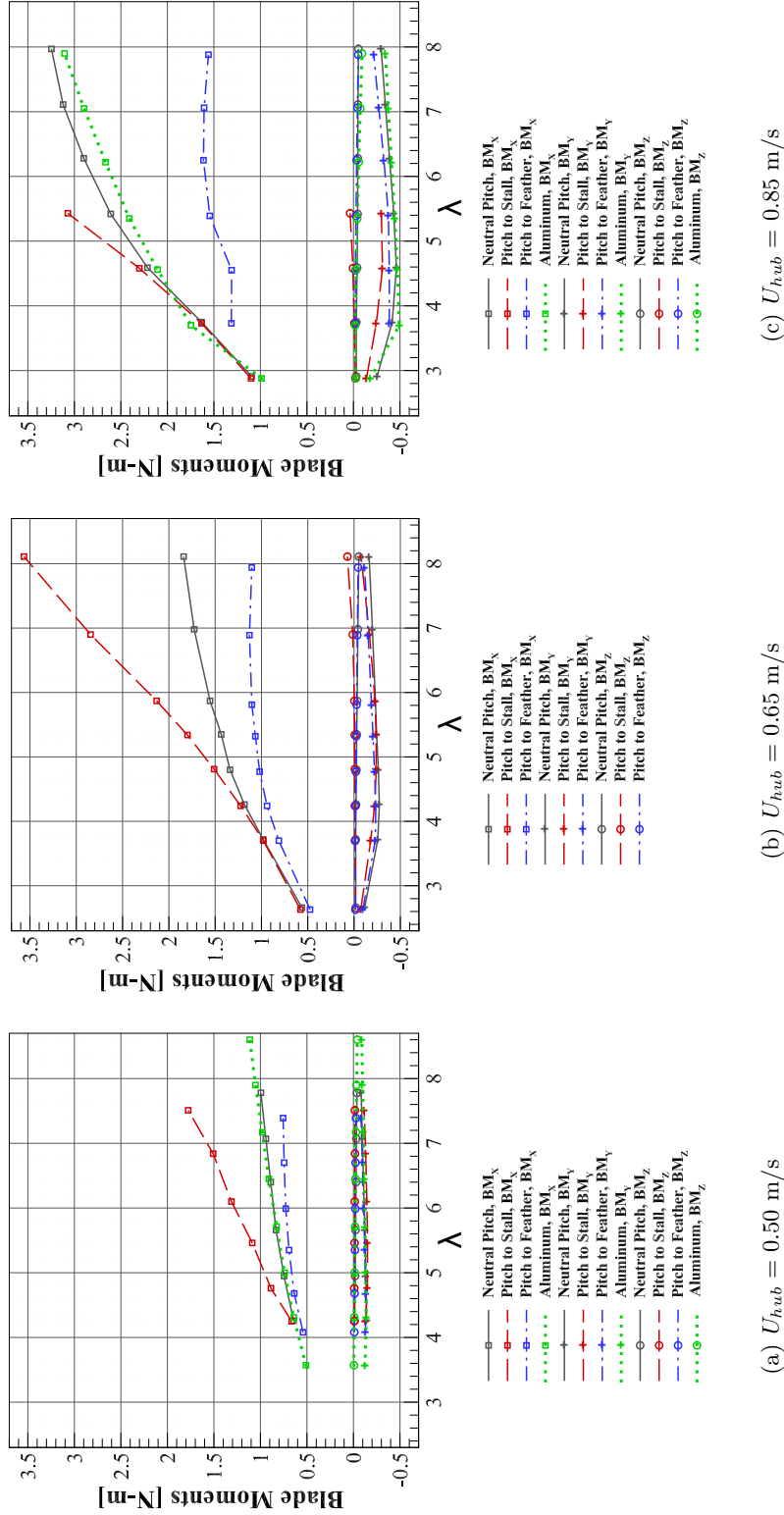
Figure 7.3: Mean moments on the key blade load cell for each inflow velocity.

force, which is larger in magnitude for the aluminum blades due to their higher total mass; the general increase in this force corresponds to the increase in rotational velocity. Beyond BF_Z, all four blade designs trend together in the x-direction forces and the y- and z-direction moments. It is worth noting that the blade pitching moment (BM_Z) is close to zero for all blades. This indicates that any twist the blades experience will likely be due to the bend-twist mechanism, rather than any outside forcing.

The largest difference by far between designs can be seen in the y-direction, or streamwise, forces (Figure 7.2) and the x-direction, or bending, moments (Figure 7.3). To better compare the different cases, Figure 7.4 shows the mean streamwise forces for each test, normalized by $1/2\rho U_{hub}^2 L_c^2$ (where L_c is the blade chord length at mid-span). These streamwise forces and the associated bending moments are the main driver for the load-dependent adaptive pitch mechanism. Thus, at low tip speed ratios the blades experience similar loading conditions, but as the forces on the system increase the performance of the different blade designs begin to diverge. As seen in the static testing, the neutral and aluminum blades behave in a similar manner, providing a baseline model for comparison. The difference in streamwise forces on the adaptive blade designs is therefore attributable to the predicted twist deformations. Under increased load, the pitch to stall blade will twist to decrease the pitch angle, effectively increasing the angle of attack. This was shown statically in Figure 6.9(b) as well as predicted numerically in [82]. The increase in angle of attack in turn causes the higher loading seen in Figure 7.4. In the opposite fashion, the pitch to feather blade twists to decrease the angle of attack and starts to shed excess loads.

Moreover, the rate of change in streamwise forces in the feathering blade is reduced at higher tip speed ratios, while the pitch to stall design starts to see exponentially increased loading. This can also be attributed to the load-dependent nature of the adaptive deformations; the pitch to feather blade twists to shed the excess loading that would cause a greater increase in twist, while the pitch to stall blade is approaching divergent behavior as seen in the numerical models and discussed in Section 4.1. It is interesting to note that slight geometric bias to pitch to feather of the neutral pitch composite and the aluminum blade designs seen in the static testing (Figure 6.10) is apparent in Figure 7.4 as well, in that the increase in streamwise loading with λ is reduced at higher tip speed ratios.
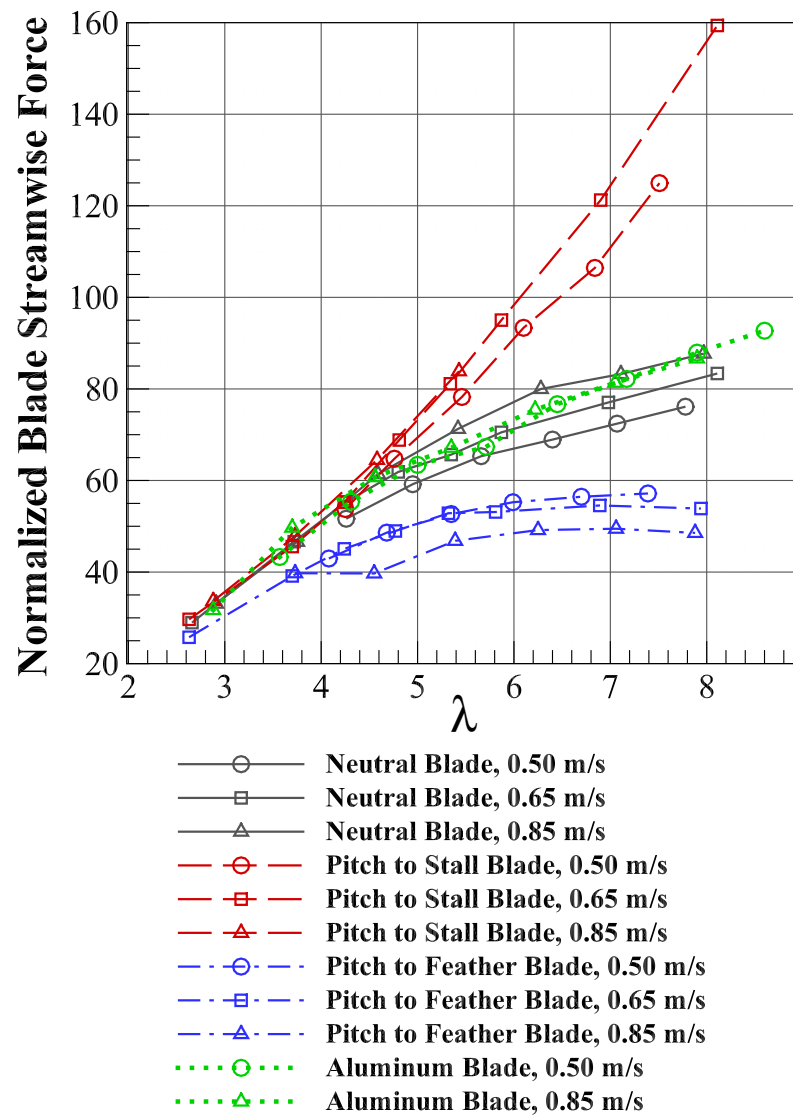
Figure 7.4: Mean normalized streamwise force on the key blade as a function of tip speed ratio (λ).

Though the forces are non-dimensionalized in Figure 7.4, it is important to consider the effect of the full dimensional loading on the blades. Due to the load-dependent nature of the bend-twist response, the adaptive behavior of the blades should further diverge with increased fluid loading. As the velocity increases, the forces and moments that drive the adaptive pitch mechanism at a given tip speed ratio also increases. This can be seen in Figure 7.4; as the inflow velocity increases, the normalized streamwise loading on the adaptive blades increases for the pitch to stall design and decreases on the pitch to feather. This underlines the necessity of taking full dimensional loading into account when assessing the performance of adaptive blades, rather than expressing performance as a simple function of tip speed ratio.

In the dynamic testing of the adaptive turbine systems, the predicted load control behavior was demonstrated experimentally. The pitch to feather and pitch to stall behaviors seen under static conditions successfully adjusted the loading on the turbine blades as designed; the pitch to stall blades captured increased loading while the pitch to feather blades shed excess forces. Though there is an apparent benefit in power generation to a load-capturing strategy, such a system would need to be carefully designed in order to avoid flow separation and stall and minimize the risk of failure due to the divergent behavior of the pitch to stall mechanism.

7.3 Hub Loading and Performance

Along with blade loads, rotor force and moment measurements were collected. These are shown in Figs. 7.5 and 7.6. In Figure 7.5, all four blade designs show negligible forces in the cross-stream (HF_Y) and vertical (HF_X) directions. In Figure 7.6, the hub pitch and yaw moments (HM_Y and HM_X, respectively) start out near zero at low λ, but increase in magnitude was the tip speed ratio increases. This is due to a slight asymmetry in the hub assembly that created an imbalance in the rotor moment of inertia, leading to a slight oscillation in the cross-stream plane that increased in severity with rotational speed.

The hub axial thrust (HF_Z) and torque (HM_Z) are better discussed in terms of the more common turbine performance characteristics, coefficients of thrust (C_T) and power (C_P). To that end, the instantaneous axial thrust (HF_Z or T), moment (HM_Z or τ),

(a) $U_{hub} = 0.50$ m/s

(b) $U_{hub} = 0.65$ m/s

(c) $U_{hub} = 0.85$ m/s
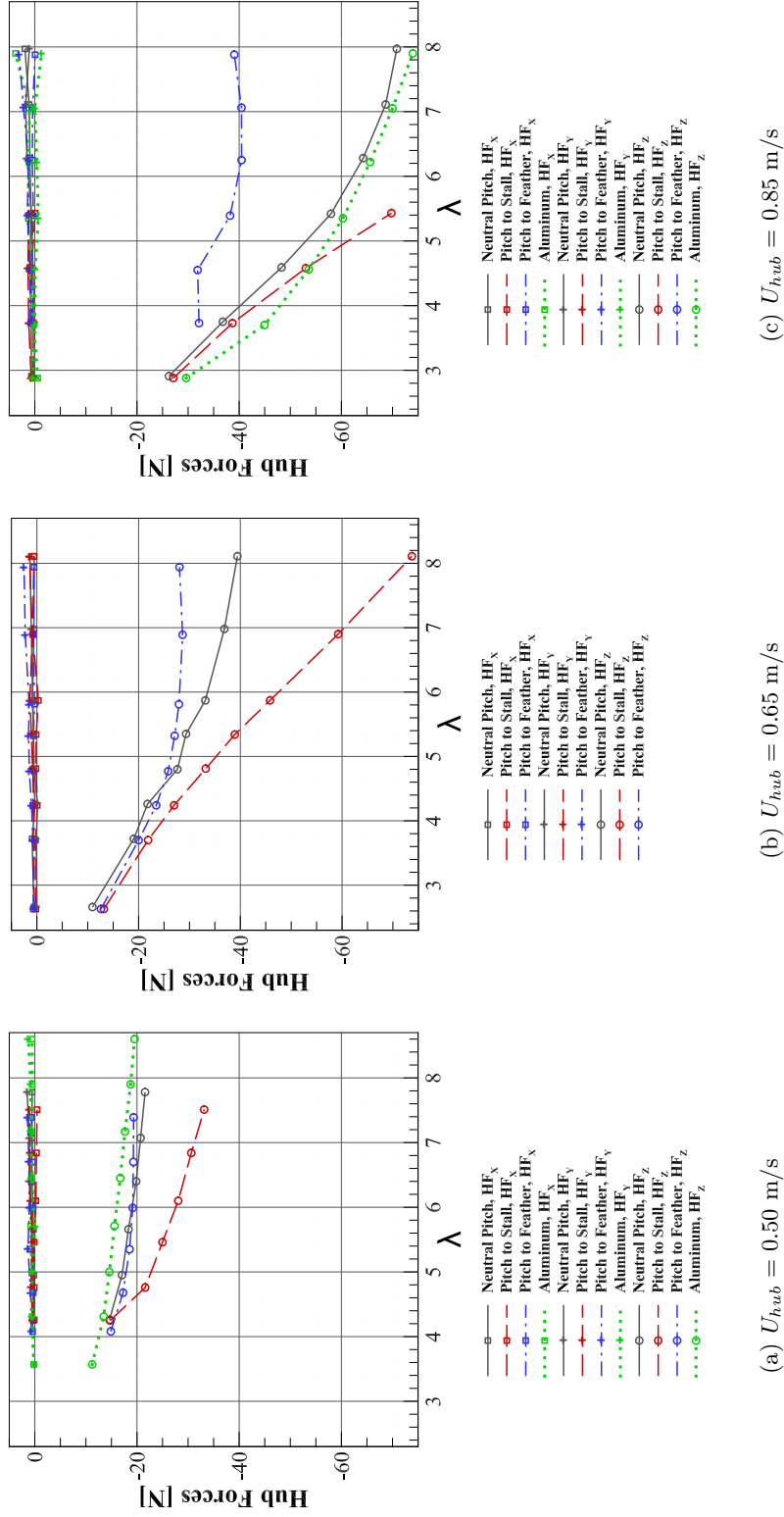
Figure 7.5: Mean forces on the hub load cell for each inflow velocity.

(a) $U_{hub} = 0.50$ m/s

(b) $U_{hub} = 0.65$ m/s

(c) $U_{hub} = 0.85$ m/s
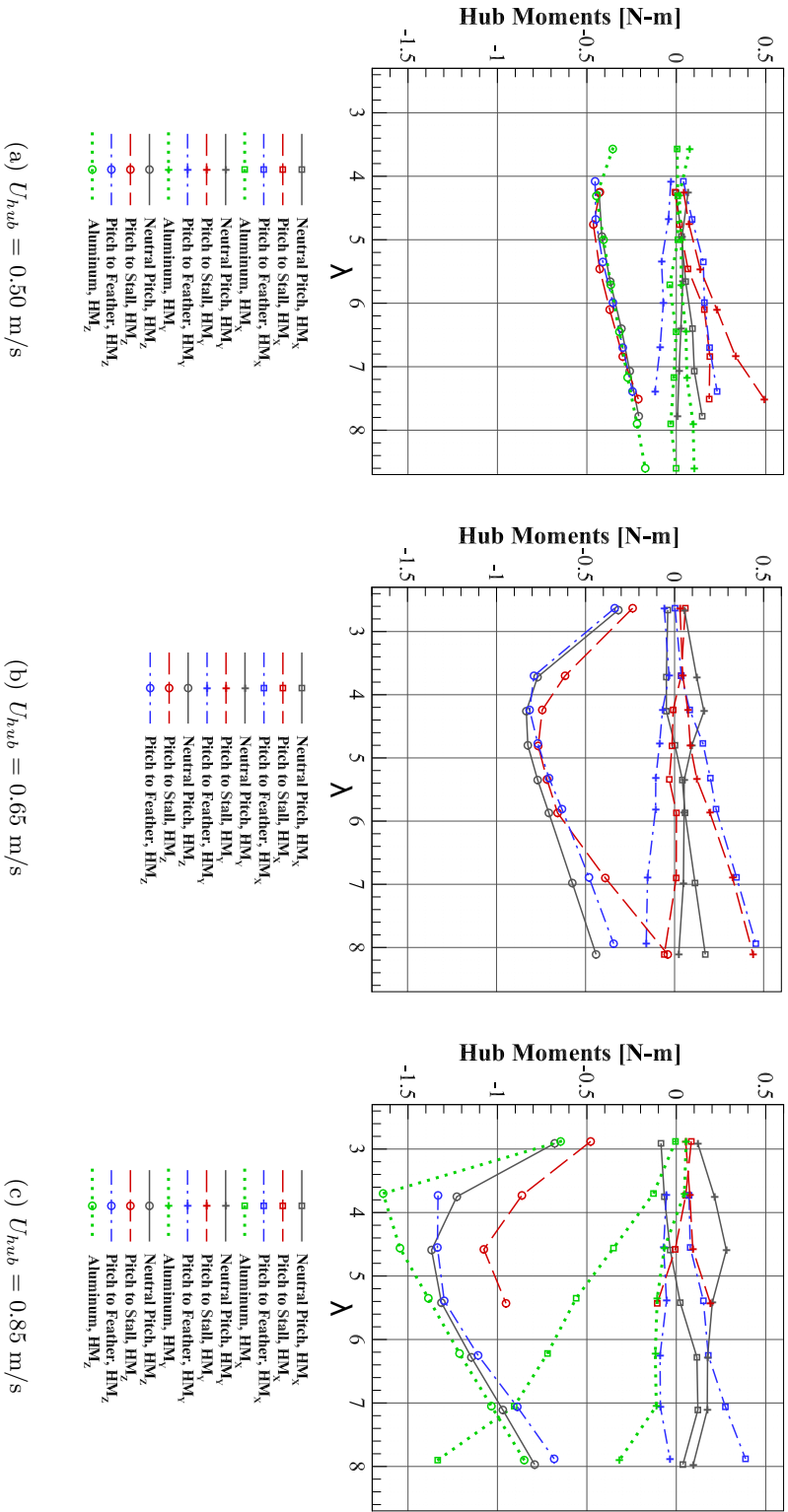
Figure 7.6: Mean moments on the hub load cell for each inflow velocity.

flow velocity (U_{hub}), and rotor angular velocity ($\omega = 2\pi f_T$) measurements were used to calculate the system thrust coefficient, $C_T = T / \left(0.5\rho A_T U_{hub}^2\right)$, and power coefficient, $C_P = (\tau\omega) / \left(0.5\rho A_T U_{hub}^3\right)$ for all four blade designs. It is important to note that no blockage corrections have been applied to these data; the blockage ratio (A_T/A_f, where A_f is the cross sectional area of the flow) of the experimental setup was determined to be $\approx 22\%$. The resulting performance curves calculated from the tests conducted at $U_{hub} = 0.50$ m/s, are shown in Figure 7.7. Error bars are used to indicate the 95% confidence interval of this data. The larger error bars seen on the calculated power coefficients relative to the thrust coefficients are likely due to the slightly higher accuracy of the hub load cell in reading thrust as compared to torque measurements.

The thrust coefficients, in Figure 7.7(a), generally reflect the trends seen in the stream-wise blade force seen in Figure 7.2(a). The pitch to stall system experiences increased thrust compared to the neutral pitch design as the tip speed ratio increases, while the pitch to feather system sheds load over the same range. The neutral pitch system differs slightly from the aluminum blades, but maintains a similar trend. In Figure 7.7(b), the calculated power coefficients are displayed. Though all four designs show comparable performance behavior, there are several features to highlight. From the lower tip speed ratios to the apex of the curve, the pitch to stall blade produced a generally higher C_P than the other designs. The pitch to feather blade had the lowest calculated value, while the neutral and aluminum blades fell in between. However, at higher tip speed ratios, the performance of all three composite blades falls off much more steeply than the aluminum blades. This is likely due to the fact that the composite blades, especially of the pitch to stall design, showed considerable out-of-plane deformation with increased thrust on the system. In this case, increased lift on the foils will not translate as directly to increased torque on the system, and much of the gains in performance expected from the pitch to stall system would be lost.

As mentioned above, the adaptive composite mechanism depends on both the dimensional loading and the tip speed ratio. It is therefore essential to look at performance trends at multiple inflow velocities. To that end, Figure 7.8 shows power and thrust coefficients calculated from experiments at $U_{hub} = 0.85$ m/s. It is interesting to note that the total uncertainty of the power coefficients at $U_{hub} = 0.85$ m/s is less than that of the power

102
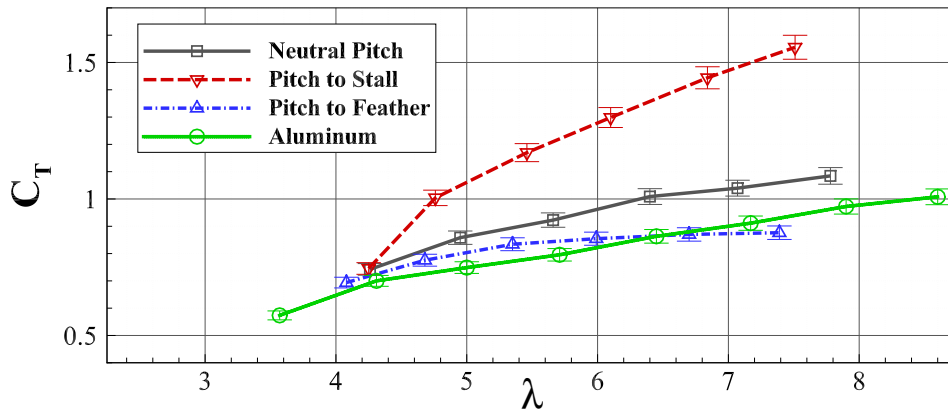
(a) Calculated thrust coefficients
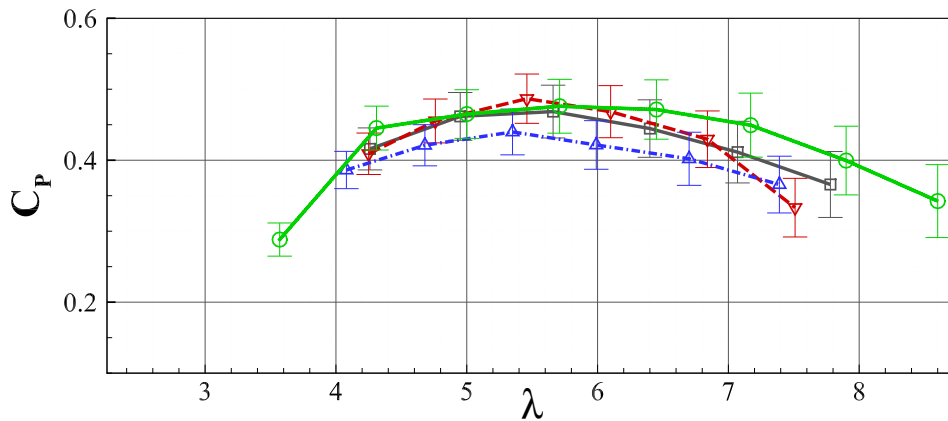
(b) Calculated power coefficients

Figure 7.7: System performance characteristics with increasing λ at $U_{hub} = 0.50$ m/s.

coefficients at $U_{hub} = 0.50$ m/s. This is due to the fact that at the lower inflow velocity, the load cell was reading at the bottom of its calibrated range. Thus the uncertainty of the reading was a larger percentage of the measured value than it was for the higher loads measured at the higher inflow velocity.

The first aspect to note is that from $U_{hub} = 0.50$ m/s to $U_{hub} = 0.85$ m/s, there is a change in the performance curves for the effectively rigid aluminum system. This indicates that Reynolds number independence was not achieved between these two runs (though data from the aluminum blades at $U_{hub} = 1.0$ m/s indicates that Reynolds independence was

achieved at $U_{hub} = 0.85$ m/s); it is thus difficult to quantify the change in adaptive blade performance between the two inflow cases. However, it is still informative to compare the blades to each other. Again, good agreement is seen between the neutral and aluminum turbine systems in both thrust and power coefficients. Unlike the performance calculated at $U_{hub} = 0.50$ m/s, the pitch to stall system in this higher inflow case experienced greater thrust but with greatly reduced potential for power generation; this is likely an indicator that the blades had twisted far enough to stall entirely, instead of increasing the effective angle of attack within the operational limits. It is possible that this could have been another factor leading to the failure of that system at $\lambda \approx 6.25$. Most interesting, however, is the performance of the pitch to feather design. The load-shedding system was able to drastically reduce the thrust on the system while maintaining a power coefficient similar to the non-adaptive designs up to the peak of the performance curve. At $\lambda = 6.25$, the pitch to feather design shows a 38% reduction in thrust compared to the system with rigid aluminum blades, while the decline in power is only 7%. This ability to shed excess loading while maintaining power production could be a highly desirable characteristic for a marine hydrokinetic turbine system.

7.4   Blade Failure

Beyond examining the blade and hub loading and system performance, it is essential to understand the failure of the pitch to stall design at $f_T = 3.75$ rps during the $U_{hub} = 0.85$ m/s velocity case. Examining the blades after failure showed that all three pitch to stall blades broke off completely at the connection between the composite and the aluminum root insert, as seen in Figure 7.9. From the blade load data shown in Fig 7.2 above, it is clear that the streamwise loads on the pitch to stall design were increasing in an exponential fashion between data points. A closer look at the streamwise forces on the key blade and on the full system, shown in Figure 7.10, adds further detail.

From the streamwise hub loading in Figure 7.10, it is clear that the three blades broke off over a 2-second span, or over ≈ 7.5 rotations at $f_T = 3.75$ rps. Because the streamwise force on the key blade goes to zero at the beginning of that time span, it can be understood that the key blade was the first of the three blades to fail. That is valuable, as it means
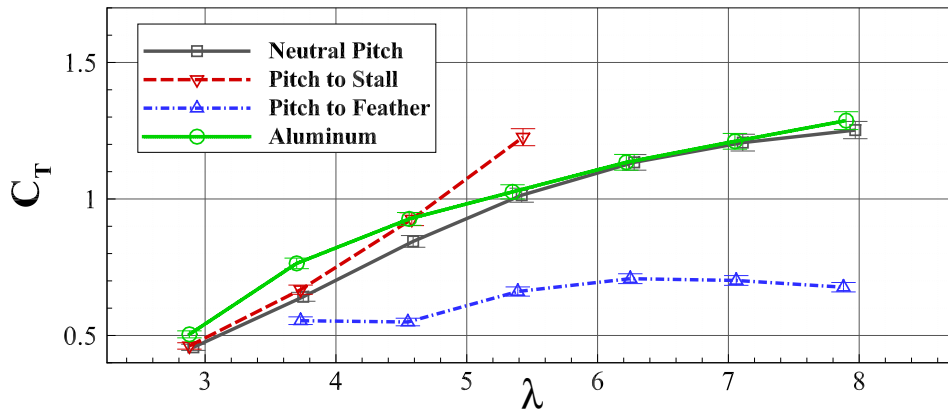
(a) Calculated thrust coefficients
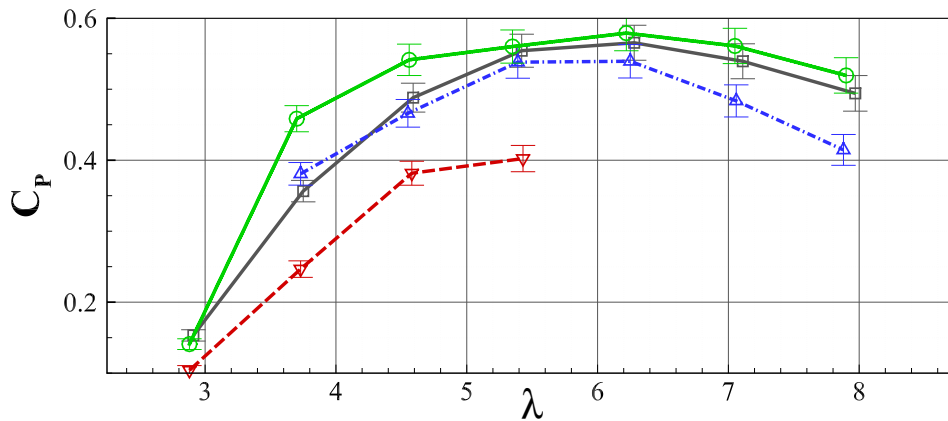
(b) Calculated power coefficients

Figure 7.8: System performance characteristics with increasing λ at $U_{hub} = 0.85$ m/s.

the loading on the blade was recorded up to the moment of the initial failure. Figure 7.10 also shows a slight decrease in magnitude and variation of the blade streamwise force in the second before failure, which might indicate increasing flexibility from a growing fault in the composite.

To further investigate the material response, the blades were examined in a North Star Imaging X5000 computed tomography (CT) scanner in the Structures Laboratory at the University of Washington. Each failed blade was scanned with an FXE 225 kV x-ray source and a Perkin Elmer 16 in DDA detector panel at a resolution of 64-70 microns. A selection

Figure 7.9: Pitch to stall blade failure between blades (top) and root connection (bottom).
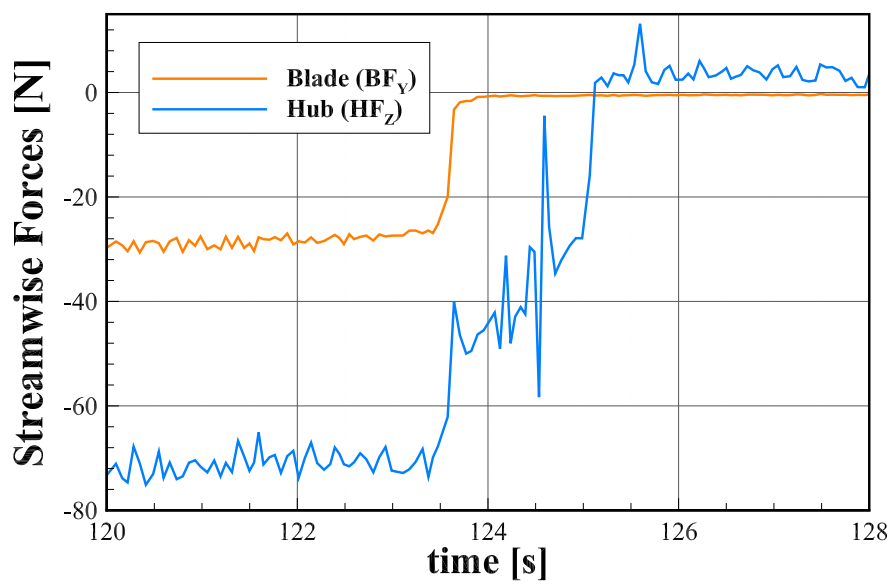
Figure 7.10: Streamwise forces on the blade and hub at failure.

of images taken from the scan of the key blade are shown in Figure 7.11. In these figures, lighter color indicates higher density. In Figure 7.11(a), The negative impression of the blade root insert can be seen (compare to Figure 7.9). Figure 7.11(b) shows a flapwise cross-section of the blade root. The site of failure is indicated in red, where a crack in the composite was discovered. Analysis of the CT scan suggested that the fault likely initiated in the area of high stress concentration adjacent to the root insert and propagated along the length of the blade before reaching the critical failure point.

Though it is essential to understand the reason for the blade failure, the structural weakness in this case was a consequence of the way in which the design and fabrication process was modified to produce small-scale blades. Thus, the wider application of this knowledge to blade design is limited; however, it is important to note that only the pitch to stall system experienced this failure. In the design of pitch to stall blades, extensive care must be taken to fully understand both the normal operating conditions and the extreme loads likely at a given site to ensure the safety of the structural system. Though there is a possible benefit in power generation to a load-capturing strategy, such a system would need to be carefully designed in order to minimize the risk of failure due to the divergent behavior of the pitch to stall mechanism. Because of the load-shedding behavior of the pitch to feather mechanism, these designs are less sensitive to changes in force under high loading conditions. Thus, the pitch to feather design strategy is considerably more robust in extreme conditions.

7.5   Wake Imaging

In addition to analyzing blade load and performance, Particle Image Velocimetry (PIV) was used to characterize the wake of the turbine rotor under different tip speed ratios and Reynolds numbers. PIV is a non-intrusive optical method widely used in fluid mechanics to determine instantaneous flow velocities; the method involves the correlation of the position of particles suspended in the flow between two images taken in quick succession. The images are captured by briefly illuminating the plane of interest in the flow with a laser sheet. Light scattered by the particles in the pair of images can then be correlated and particle displacement calculated; those displacements divided by the time elapsed between
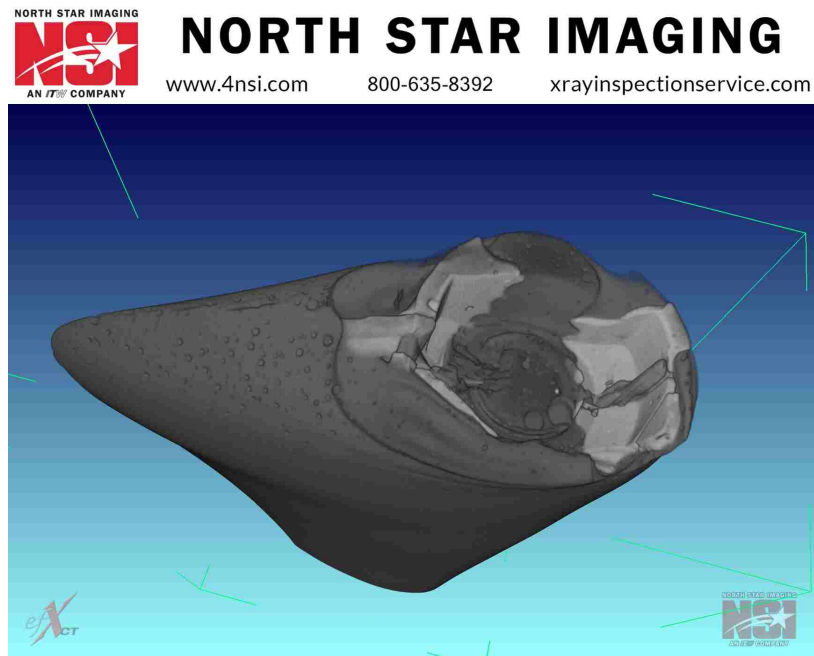
(a) CT scan image of key blade root
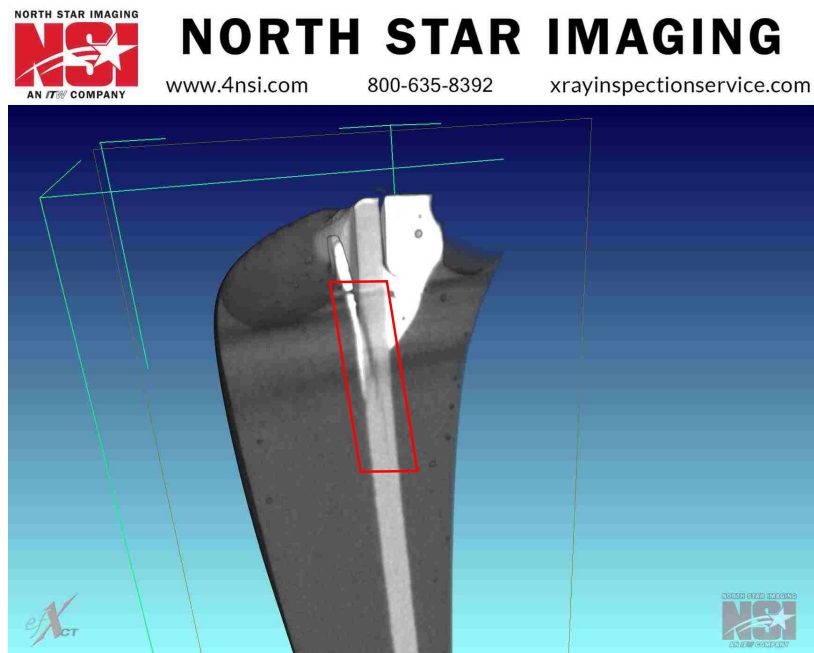
(b) Flapwise slice of the key blade scan, site of failure indicated

Figure 7.11: Results of computed tomography scan of key blade post-failure. Lighter color indicates higher density.

images provide a fully-realized velocity field.

A LaVision PIV system at the Bamfield Marine Science Centre was used in this study. The system used consisted of a dual frame-straddling camera, a timing unit, and a laser. The camera setup had an acquisition rate of 15 Hz and a resolution of 2560 x 1600 pixels per image, with a field of view of 38 x 24 cm. The laser sheet was $\approx$3 mm thick; the laser operated at $\approx$120 mJ per pulse. Inter-frame time was set to 1 ms, leading to an average displacement between frames of 6 pixels. PIV measurements were conducted on a horizontal plane at hub height, located 2.3 turbine diameters downstream of the rotor plane and covering about 75% of the flume width, with two cameras each spanning 40% of the width with a 5% overlap. Note that 2.3D in this case is immediately downstream of the turbine nacelle. 900-2700 image pairs were temporally-averaged to determine mean wake effects.

Mean normalized wake profiles calculated at hub height in the cross-stream direction of the rigid aluminum, pitch to feather, and pitch to stall turbine systems are shown in Figure 7.12, respectively. PIV data was not collected during the neutral blade runs due to time limitations.

Between the blade designs, there are several differences in the overall shape of the wake profiles. Most significantly, the variability of the flow deceleration in the rotor wake, particularly near the blade roots ($y/d_T \approx 0.25$), is notably greater for the pitch to stall blades than in the pitch to feather, with the spread in the wake from the aluminum blades falling in between the two. This is associated with a steeper change in the thrust curve, which agrees with both blade loading and C_T results shown in Figs. 7.4 and 7.8(a).

There is also a significant difference between the blade designs found in the bypass flow, the part of the flow which is forced to accelerate around the outside of the rotor disk due to the blockage of the turbine, where $\bar{u}/u_\infty > 1.0$. Results show that peak velocities in the bypass flow are larger for the pitch to stall design and minimum for the pitch to feather blades. This is in agreement with the notion that thrust and loads on the pitch to feather blade design are minimized, reducing the acceleration of flow around the rotor disk.

As in previous results, the two adaptive blade designs show similar effects at low tip speed ratios; the difference between the blade behaviors becomes stronger as λ increases. This
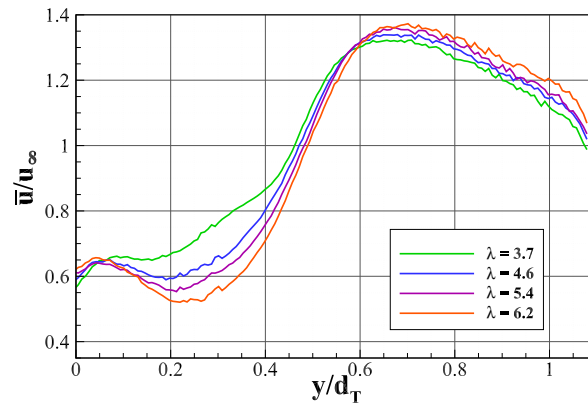
(a) Aluminum blade wake
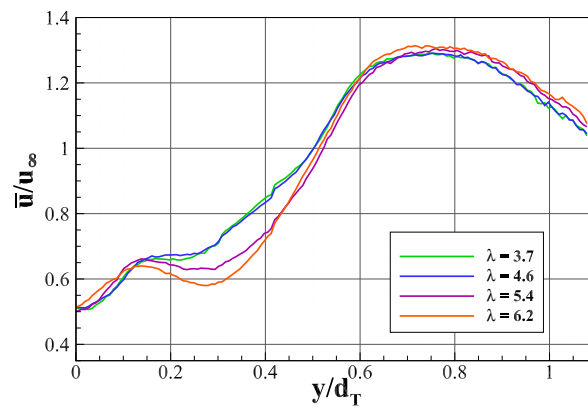
(b) Pitch to feather blade wake
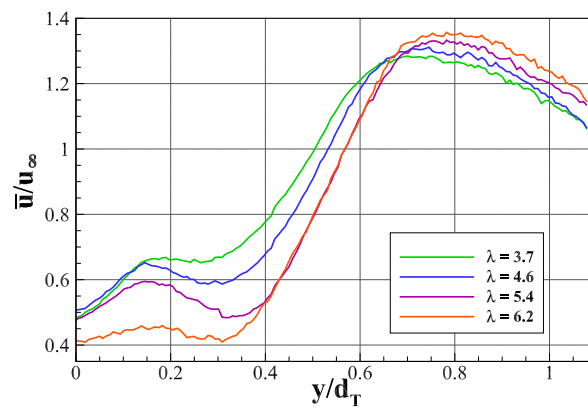
(c) Pitch to stall blade wake

Figure 7.12: Wake velocity profiles at 2.3D, $U_{hub} = 0.85$ m/s.
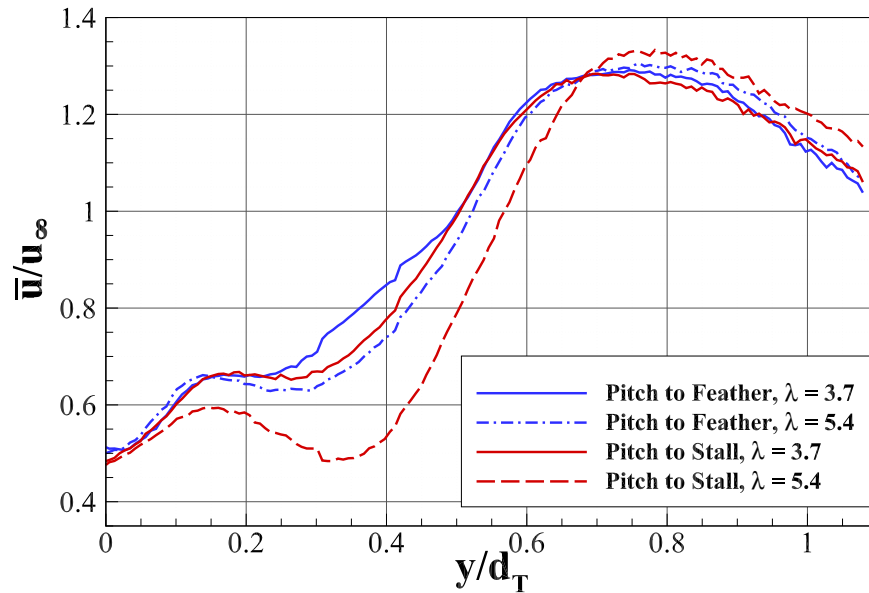
Figure 7.13: Wake velocity profiles at 2.3D for both adaptive blade designs at $\lambda = 3.7$ and 5.4, $U_{hub} = 0.85$ m/s.

is shown more clearly in Figure 7.13, where the normalized wake profiles for the adaptive blade designs are shown together for both a low tip speed ratio ($\lambda = 3.7$) and a tip speed ratio near the peak of the C_P curve ($\lambda = 5.4$). The increase in rotational speed creates little difference in the flow deceleration in the rotor wake for the pitch to feather design, but the deceleration in the wake of the pitch to stall design is significant; again, this is due to the much higher relative thrust loads on the pitch to stall design.

Overall, the wake characterization of the flow around the rigid and adaptive blade systems supports previous results of the blade loads and performance analyses; the adaptive pitch to stall blade design was seen to capture higher loads than the neutral blades, while the pitch to feather blades shed the excess loading.

Chapter 8

FLUME TESTING: TURBULENT INFLOW

In Chapter 7, the adaptive mechanism was shown to offer potential improvements in steady flow conditions; however, a marine turbine will realistically spend much of its operating life in the presence of various scales of turbulence structures. The ability of an adaptive pitch to feather composite blade to passively adjust to the instantaneous flow and shed excess loading may be an especially valuable asset under turbulent conditions. To investigate this possibility, an additional flume-scale experimental study was performed comparing the behavior of the axial-flow hydrokinetic turbine with adaptive pitch to feather blades to the same turbine with non-adaptive composite blades under various scales of eddies in the inflow.

8.1 Effects of Turbulence

Marine hydrokinetic turbines are typically deployed at energy-dense sites where fluid flow can be extremely complex. Boundary layer flow, free surface waves, currents, local bathymetry, and surrounding structures or turbines combine to create highly nonuniform inflows that vary spatially and temporally. These complex flow fields typically contain turbulence at a large array of length and time scales [110]. Previous studies have found that the performance, blade loads, and fatigue life of hydrokinetic turbines can depend strongly on a variety of turbulence parameters. Blackmore et al. found that both turbulence intensity and turbulent length scale can have large impacts on blade and rotor loads and turbine performance characteristics [20, 21]. Chamorro et al. determined that instantaneous power generation is affected most strongly by low frequency turbulent flow features, relative to the rotor tip speed ratio [30]. Additionally, a spectral analysis of the turbine wake suggested that this region is especially sensitive to turbulence [29]. Mycek et al. also found that turbulence intensity has a large impact on the wake region, though less of an effect

on performance [92]. A parametric study conducted by Milne et al. identified longitudinal turbulence intensity as the dominant factor for blade loading, though integral length scale had a larger influence on extreme and fatigue loads [76, 77].

Overall, previous studies agree that both turbulence intensity and integral length scale have a significant impact on turbine behavior and wake structure. To focus on the possible benefits that an adaptive blade system could offer in turbulent inflow, this study centers on introducing well-defined, coherent, and isolated eddy structures of varying length scale relative to the size of the turbine. This is accomplished by placing vertically-oriented cylinders of various diameters upstream of the turbine in order to introduce dominant coherent eddies to the inflow. In this way, specific frequencies can be targeted for analysis and comparison between the two systems. These frequencies were chosen to be within the highly responsive region of the turbine, as identified in [30].

8.2   *Experimental Facility and Procedures*

Testing was performed at the Tyler flume at the University of Washington. The Tyler flume is a glass-walled flume, 0.75 m wide by 3 m long. Background turbulence levels are typically very low ($\approx 2\%$) due to a 3 m wide stilling basin above the test section. Dynamic water depth was controlled at 0.6 m. A recirculating pump provided constant flow through the test section; flume velocity was maintained at 0.5 m/s throughout the testing program.

During flume testing, a Nortek Vector acoustic Doppler velocimeter (ADV) was used to quantify the instantaneous three-dimensional velocities in the approach flow, located -3D upstream of the rotor plane and sampling at hub height in the center of the channel. Additionally, two Nortek Vectrino Profiler ADVs were used to characterize the flow upstream and downstream ($\pm$ 1.2D) of the rotor energy extraction plane. The upstream (-1.2D) Vectrino was positioned at approximately 0.02 m inboard from the blade tip ($r/R \approx 0.9$) and sampled at hub height. The structures from both upstream ADVs were confirmed to be outside the swept rotor area. The downstream Vectrino also sampled at hub height and was aligned with the blade tip in order to capture tip vortex dynamics.

Both turbine blade systems were tested at three states of turbulence. For each case, rotor and blade loading and instantaneous velocities were recorded for turbine rotational

speeds of $f_T = 1.0\text{-}3.5$ rps. During the first case (T0), no turbulence was added to the flow. For the second case (T1), a small vertically-oriented cylinder was installed upstream of the turbine ($d_{c_1} = 0.06$ m) to introduce coherent turbulent eddies with length scales on the order of the blade chord ($d_{c_1} \approx 2l_c$). A third test scenario (T2), used a larger vertically-oriented cylinder ($d_{c_2} = 0.107$ m) to create turbulent structures on the length scale of the rotor radius ($d_{c_2} \approx 1/2R_T$). The cross-stream location of each cylinder was centered with the upstream (-1.2D) ADV. Details of the cylinders, location with respect to the turbine rotor energy extraction plane, and characteristic vortex dynamics are provided in Table 8.1.

8.2.1 Inflow Profile

The addition of the cylinders changed the approach flow significantly. Table 8.1 provides details of the cylinders as well as the associated von Kármán shedding frequency ($f_k = StU/d_{c_i}$, where St is the dimensionless Strouhal number, a function of Reynolds number), and streamwise turbulence intensity (I_u). The calculated turbulence intensity ($I_u = u_{rms}/\bar{u}$) is extremely low for the case of no added turbulence; this is likely a function of the relatively low sampling frequency (≈ 45 Hz). Note that the large cylinder increased not only the characteristic length scale of the energetic coherent structures in the flow but also the mean turbulence intensity compared to the small cylinder case.

To verify the influence of the cylinders, a spectral analysis of the inflow was performed. Figure 8.1 shows the result for the T1, small cylinder case at $f_T = 2$ rps; the u and v components of the inflow velocity are plotted for both the adaptive and neutral blade systems. Though one case is shown for clarity, analysis confirmed that the inflow was not influenced by the tip speed ratio or the blade design of the turbine. Two clear peaks in the velocity spectrum can be seen in Figure 8.1: the first in v at the von Kármán shedding frequency of the small cylinder, f_{c_1}, the second in u at twice that frequency, likely due to the generation of two paired counter-rotating vortices traveling in the streamwise direction. This signature of von Kármán shedding confirms the presence of well-defined, coherent turbulent structures at the target frequencies created by the introduction of the small cylinder into the approach flow. Similar results were seen for the large cylinder case.

Table 8.1: Case definition and details.

Case Name	T0	T1	T2
Turbulence Generator	None	Small cylinder $d_{c_1} = 0.06$ m	Large cylinder $d_{c_2} = 0.107$ m
Streamwise Location of Center	-	$x_{c_1} = $ -0.71 m $x_{c_1}/d_{c_1} = $ -11.8 $x_{c_1}/d_T = $ -1.6	$x_{c_2} = $ -0.87 m $x_{c_2}/d_{c_2} = $ -8.1 $x_{c_2}/d_T = $ -1.9
Von Kármán Shedding Frequency	-	$f_{c_1} = 1.72$	$f_{c_2} = 0.96$
Mean Inflow Turbulence Intensity, I_u	0.02%	18.7%	21.2%

8.2.2   Rotor Loads

In order to fully evaluate and compare the influence of the added turbulence on the adaptive and non-adaptive systems, it is necessary to consider the effect on blade loading. Changes in both mean blade loads and load variation will give an indication as to the structural robustness and fatigue life of each system.

To that end, Figure 8.2 shows the mean streamwise blade loads with increasing tip speed ratio. As expected from previous numerical and experimental studies [7, 82], the adaptive blades in each case perform similarly to the non-adaptive, or neutral, blade system at low λ, but experience increasingly reduced streamwise loading as the rotational speed increases. This load-shedding behavior is due to the load-dependent change in blade pitch, which causes the adaptive blade to increase blade pitch and therefore decrease effective angle of attack under increased load. The change in mean blade loading due to added turbulence is apparent but slight; each blade design sees a relatively small increase in mean streamwise loading as turbulent activity increases.
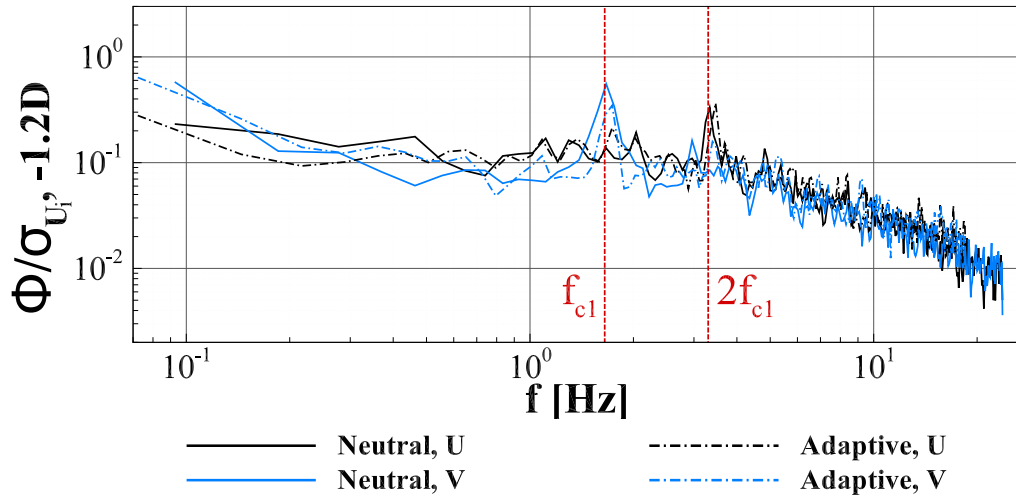
Figure 8.1: Spectral analysis of hub-height streamwise velocity at -1.2D, case T1, $f_T = 2$ rps ($\lambda \approx 5.5$).

Though the additional turbulence does not appear to have a large impact on mean blade loading, it is also important to consider blade load variations. Research has shown that variations in streamwise forces and bending moments due to turbulence contribute significantly to blade fatigue and failure [76]. To investigate the impact of added turbulence on blade load variations, Figure 8.3 shows the root mean square of the blade streamwise force with increasing tip speed ratio. As expected, load variation increases with both turbulence and rotational speed. However, the adaptive blade turbine again shows advantageous behavior over the neutral blade design. Not only does the use of adaptive blades reduce load variations, but it is shown to provide higher reduction in load variation in cases of increased turbulence. This is due to the nearly instantaneous nature of the adaptive response, which allows for automatic pitch adjustment to turbulent fluctuations in the ambient flow. As seen in Figure 8.2, the difference in performance between the two blade models increases with increasing dimensional loading; the behaviors of the neutral and adaptive systems begin to differ increasingly after $\lambda \approx 6$.

The reduction in both mean streamwise blade loading and load variation found via the use of adaptive pitch blades is significant to the lifetime robustness of a marine hydrokinetic
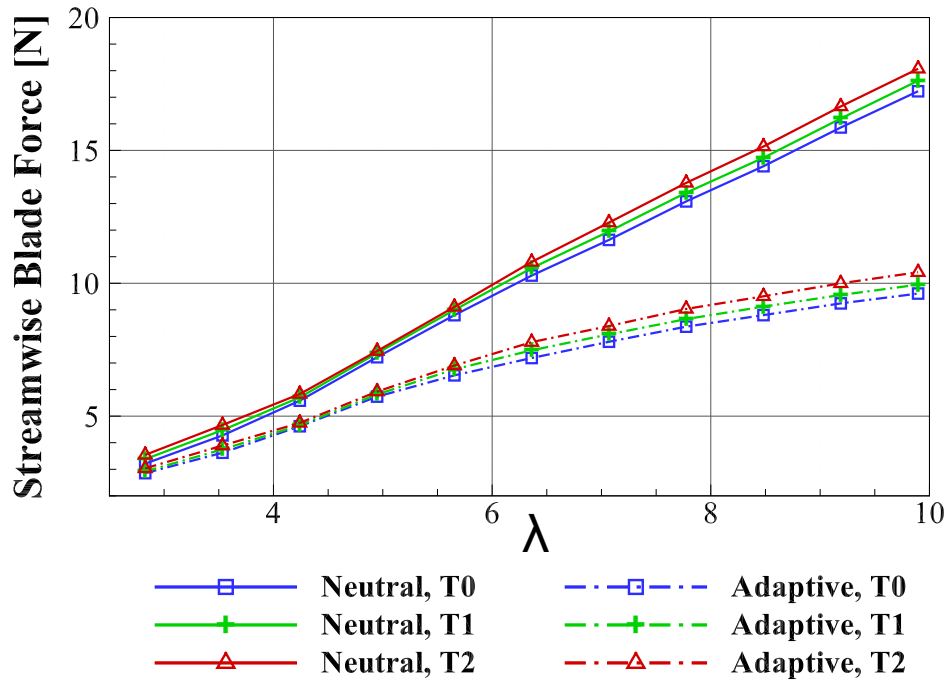
Figure 8.2: Mean streamwise force on the key blade for each case and blade design.

turbine. These reductions would lead to fewer fatigue cycles and lower extreme loads, increasing structural reliability of the turbine. Because of this behavior, an adaptive blade system is highly advantageous under turbulent conditions.

8.2.3 Turbine Performance

To further compare the adaptive and non-adaptive blade turbines, the impact of the added turbulent structures on the power generating capacity of each system is considered. To that end, the instantaneous rotor moment (τ), mean inflow velocity ($\bar{U}_{hub}$), and angular velocity ($\omega = 2\pi f_T$) measurements were used to calculate the system power coefficient, $C_P = (\tau \omega) / \left(0.5\rho A_T \bar{U}_{hub}^3\right)$. A spectral analysis of the resulting instantaneous power coefficient for all cases at $f_T = 2.5$ rps ($\lambda \approx 7$) is shown in Figure 8.4.

There are three distinct peaks in the frequency content of the instantaneous power coefficients seen in Figure 8.4. For all cases and blade designs, there is a local maximum in
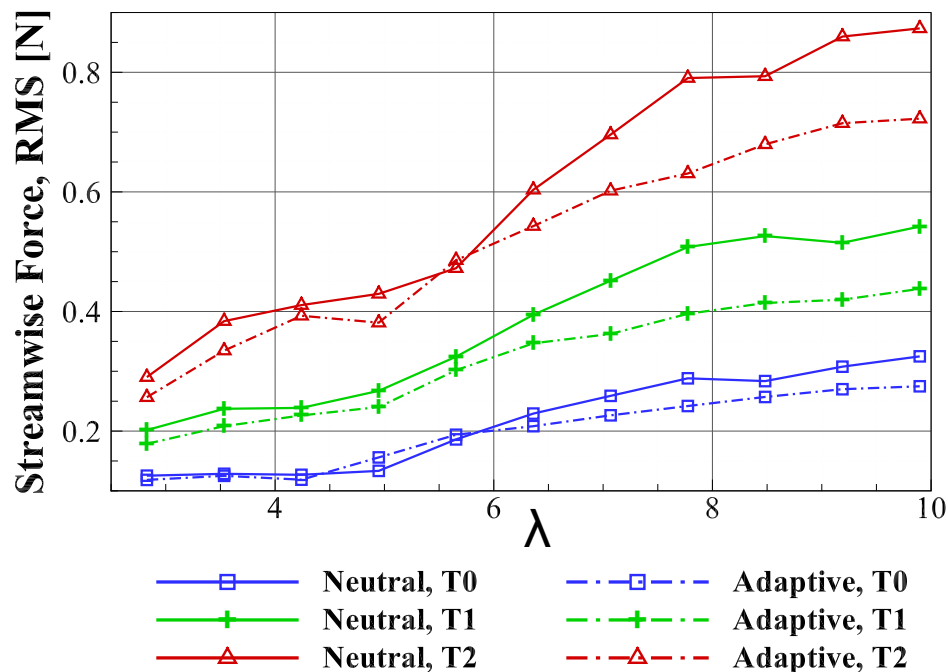
Figure 8.3: Streamwise force variation on the key blade for each case and blade design.

at $f \approx 2.5$, reflecting the rotational frequency of the rotor. More interesting, however, are the two case-specific peaks. Most prominently, there is a strong signal at $f \approx 1.0$ for both blade designs in the T2 case, seen in Figure 8.4(c). This coincides with the von Kármán shedding frequency of the cylinder associated with case T2, f_{c_2}, which indicates that the presence of the cylinder in the approach flow created significant fluctuations in the rotor torque due to the coherent, energetic eddy structures introduced into the inflow at that frequency. Secondly, there is a distinct signal at $f \approx 1.7$ in the power spectrum of both blade designs in the T1 case, seen in Figure 8.4(b). Again, this matches the von Kármán shedding frequency of the associated cylinder, f_{c_1}. Though the peak in the spectral content is clear, this signal is significantly weaker than that generated by the cylinder in the T2 case. There are two factors that could explain this phenomena. The overall turbulence intensity is lower in case T1 compared to case T2, and this could lead to the turbulent eddies having a lesser impact on the rotor performance. However, another factor to consider is the length
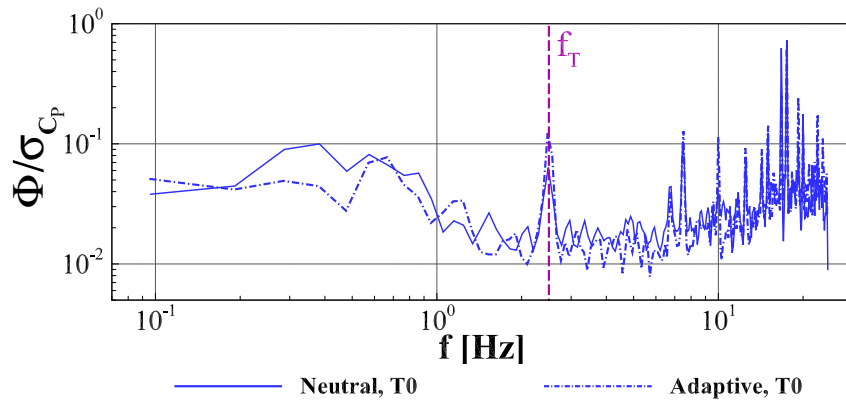
(a) Case T0
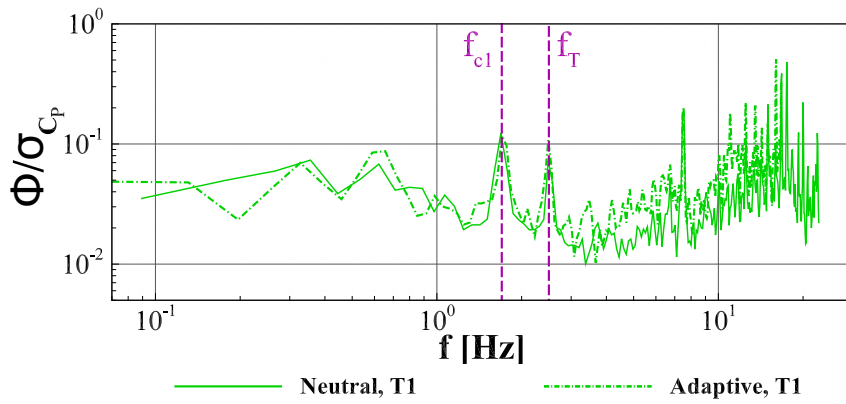
(b) Case T1
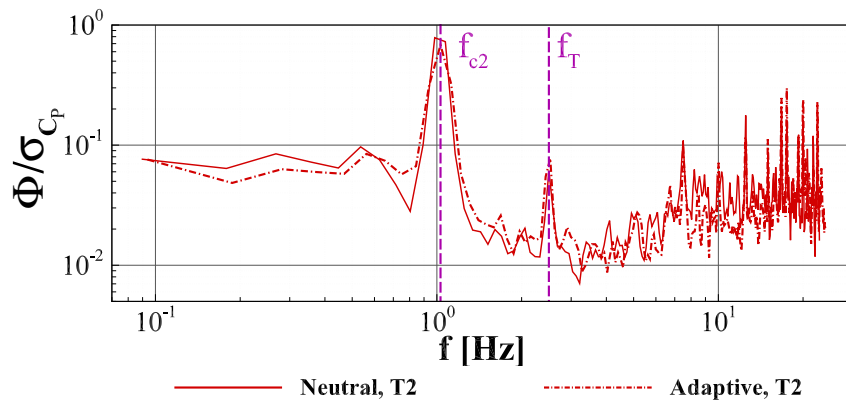
(c) Case T2

Figure 8.4: Spectral analysis of power coefficient for each case and blade design, $f_T = 2.5$ rps ($\lambda \approx 7$).

scale of the induced turbulent structures. In case T1, the length scale of the cylinder-induced structures is on the order of the blade chord length ($d_{c_1} \approx 2l_c$), whereas in T2 the length scale is on the order of the rotor radius ($d_{c_2} \approx 1/2R_T$). It is likely that the turbulent structures with a length scale on the order of the rotor will affect the rotor torque more strongly than those on a smaller scale.

To more closely investigate the turbine performance at these frequencies, it is useful to examine the relative intensity of the T1 and T2 peaks with increasing tip speed ratio. To that end, the spectral intensity at $f = f_{c_1}$ and $f = f_{c_2}$ for every case is plotted as a function of tip speed ratio in Figs. 8.5(a) and 8.5(b), respectively. The first item of note is that the magnitude of spectral excitation overall is lower at $f = f_{c_1}$, in Figure 8.5(a), than for $f = f_{c_2}$, in Figure 8.5(b). This is in agreement with the trend seen in Figure 8.4. As expected, the only significant excitation at $f = f_{c_1}$ is in the case T1 results; the same is true for $f = f_{c_2}$ for case T2. This shows that the excitation at these specific frequencies is solely due to the associated induced turbulent structures. The only exception is for the points around $f_{c_i} = f_T$ in each case, where there the rotational frequency of the rotor adds to the overall spectral intensity, as seen in Figure 8.4.

Again, in both Figure 8.5(a) and Figure 8.5(b) the adaptive blade turbine behaves similarly to the neutral system at low tip speed ratios. As λ increases, however, the effect of the adaptive blade mechanism becomes more apparent. At higher tip speed ratios in Figure 8.5(a), the adaptive system shows consistently lower excitation at the von Kármán shedding frequency compared to the neutral blade turbine. This can be attributed to the adaptive mechanism reducing the effect of fluctuations in the flow, as they were seen to reduce load variation under conditions of increased turbulence in Figure 8.3. This trend is much less pronounced in Figure 8.5(b), however, suggesting that the the adaptive mechanism is more successful in filtering out the effect of fluctuations on rotor torque from turbulent structures with a length scale on the order of the blade, rather than larger eddies that might encompass more of the rotor area.

Combined with the trends in blade loading discussed in Section 8.2.2, these results indicate that the adaptive mechanism could be employed to reduce the effect of flow fluctuations on a marine hydrokinetic turbine. Though the impact of flow fluctuations on blade loading

120
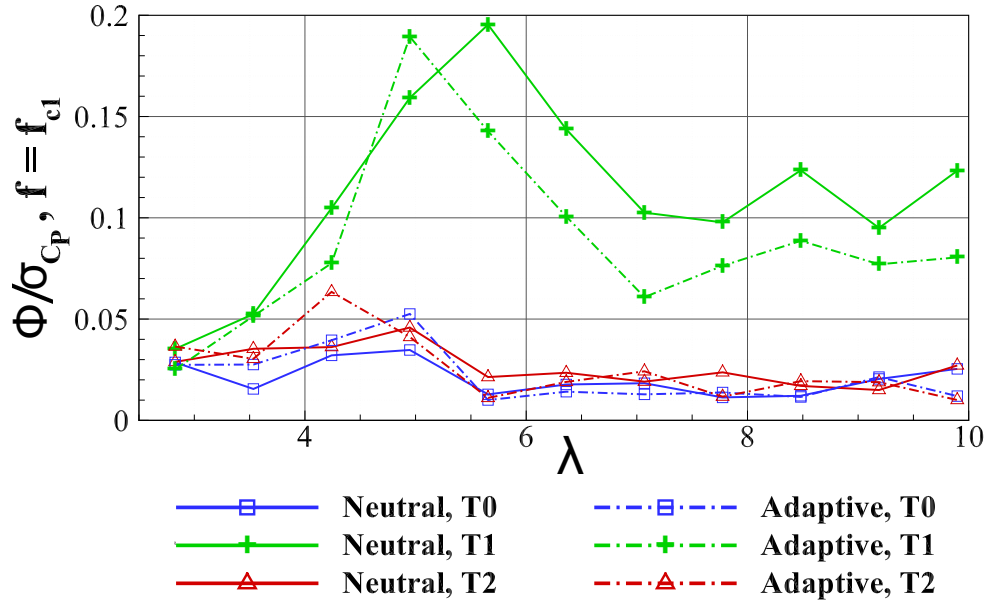
(a) ϕ/σ_{C_P} at $f = f_{c_1}$
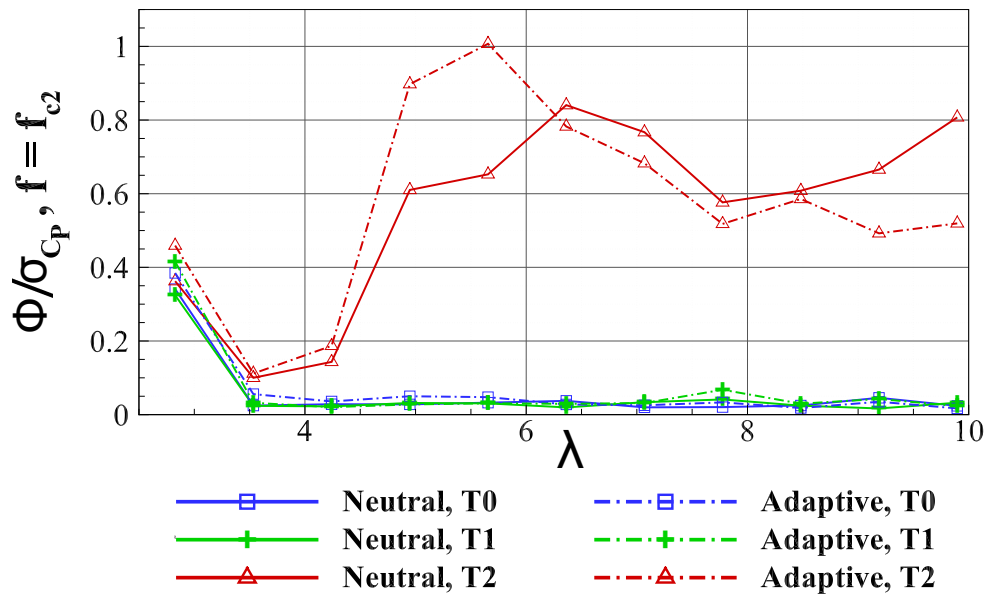
(b) ϕ/σ_{C_P} at $f = f_{c_2}$

Figure 8.5: Φ/σ_{C_P} for all cases at the von Kármán shedding frequency of each cylinder.

is shown to be reduced for both turbulent length scales studied, the benefits that can be gained in system performance appear to be most effective at turbulent length scales on the order of the blade.

8.2.4 Wake Characterization

The last factor to consider in evaluating the relative performance of the two turbine systems in turbulent flow is the impact of the adaptive mechanism in the wake region. Flow effects in this region have significant implications for array design; additionally, further analysis of the wake can provide added insight into turbine behavior. This section presents an analysis of the velocity readings measured at 1.2D downstream of the turbine, at hub height, and aligned with the blade tip in the cross-stream direction. The location of the downstream ADV allows features of the tip vortices to be captured.

To begin the wake characterization, a spectral analysis on the downstream velocity measurements is performed. Figure 8.6 shows the frequency content of the u and v components of the wake velocity at $f_T = 2$ rps. For each case, the turbine rotational frequency (f_T), blade passing frequency ($3f_T$), and von Kármán shedding frequency of the associated cylinder (f_{c_i}, if any) are indicated.

In case T0, shown in Figure 8.6(a), there are strong peaks in the spectral intensity at the turbine rotational frequency (f_T) and blade passing frequencies ($3f_T$), as well as higher order harmonics. However, these peaks disappear completely in cases T1 and T2 (Figs. 8.6(b) and 8.6(c), respectively). This phenomena is expected, as the increase in turbulence causes heightened mixing in the wake region. The elevated mixing can also be seen in the spectral content at the von Kármán shedding frequency in cases T1 and T2; there is no discernible maximum at f_{c_1} in case T1, and only a slight peak at f_{c_2} in case T2. This is likely due to the length scale of the turbulent fluctuations, in that the flow structures on the order of the rotor maintain a stronger coherency through the rotor plane than the structures on the scale of the blade. Though the peak at f_{c_2} in Figure 8.6(c) is more prominent in the neutral blade case compared to the adaptive blade, this feature was not seen consistently.

Though the spectral content of the wake in each case appears to be little affected by
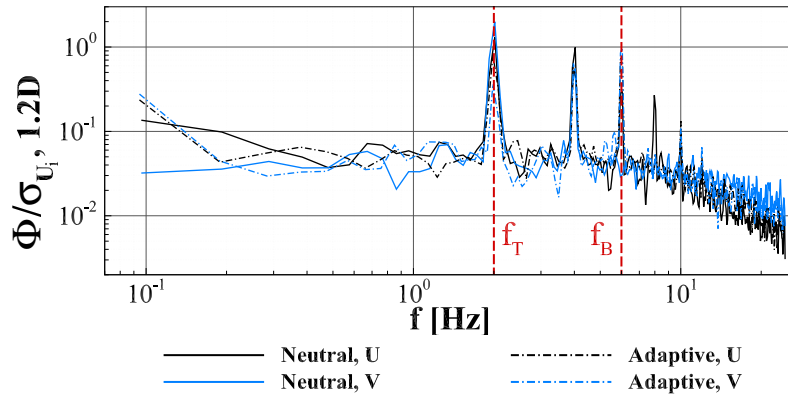
(a) Case T0
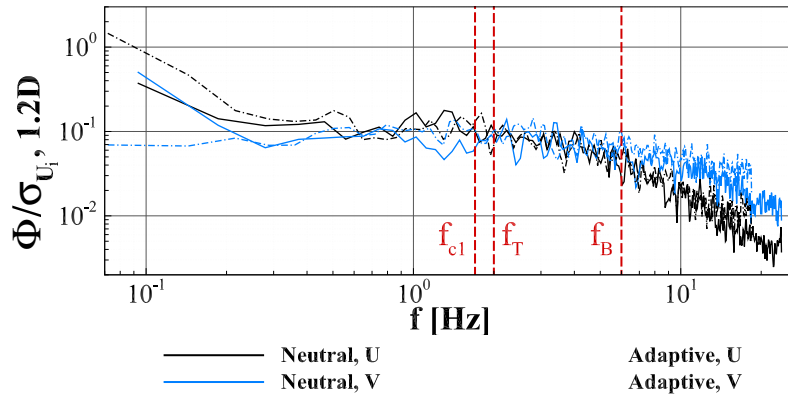
(b) Case T1
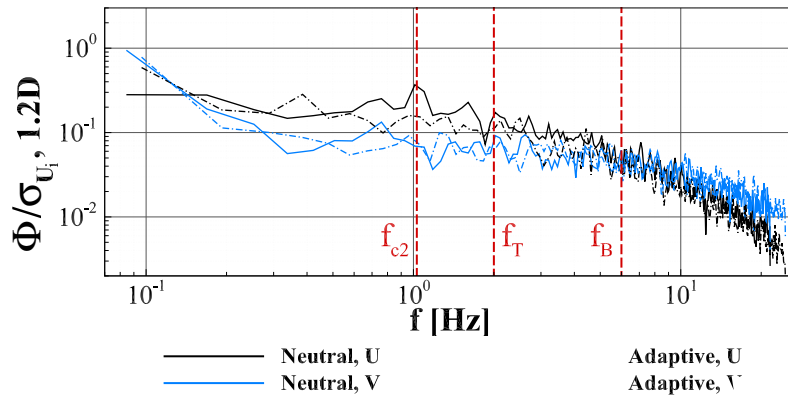
(c) Case T2

Figure 8.6: Spectral analysis of downstream streamwise and cross-stream velocities measured at hub height at 1.2D, aligned with blade tip.

blade design, it is also important to characterize the wake recovery. For that purpose, Figure 8.7 shows the mean streamwise velocity measured at the same point in the wake (1.2D downstream of the turbine, at hub height, aligned with the blade tip). In this figure, the influence of the adaptive pitch mechanism on wake recovery is shown to be highly significant. For the neutral blades, mean streamwise wake velocity decreases significantly with increasing tip speed ratio. This is in part due to the wake expansion at higher tip speed ratios, and also to the higher momentum extraction. However, the decrease of mean wake velocity with λ is much less extreme with the adaptive blades over all three cases, and in fact there is no mean wake decrease in the highest turbulence case. As λ increases, the neutral blade turbine shows a slower wake recovery and more accentuated tip vortex signature, while the adaptive blades show better recovery and less impact from the tip vortex. The presence of the von Kármán vortices in the T1 and T2 cases also induce more mixing and therefore improve wake recovery. As with previous figures, the blades behave in a similar fashion at lower tip speed ratios; the effect of the adaptive mechanism increases with increasing λ.

Finally, Figure 8.8 shows the mean turbulence intensity for each case. Again, the influence of the adaptive mechanism is significant, and increases with tip speed ratio. The neutral blades show increasing turbulence intensity with higher rotational speeds, though the trend is slight in the T0 case of no added turbulence. And in the T0 case, the adaptive blade system performs similarly to the neutral blade design. However, as added turbulence increases, the adaptive blade system shows a much different behavior pattern. In the T1 case, there is only a slight increase of turbulence intensity with λ, and in the highest turbulence case the adaptive blade mechanism decreases turbulence intensity at higher rotational speeds. The ability to effectively maintain initial turbulence levels can be related to the fact that the adaptive mechanism filters out load variations by automatically adjusting the blade geometry, as seen in Figure 8.3.
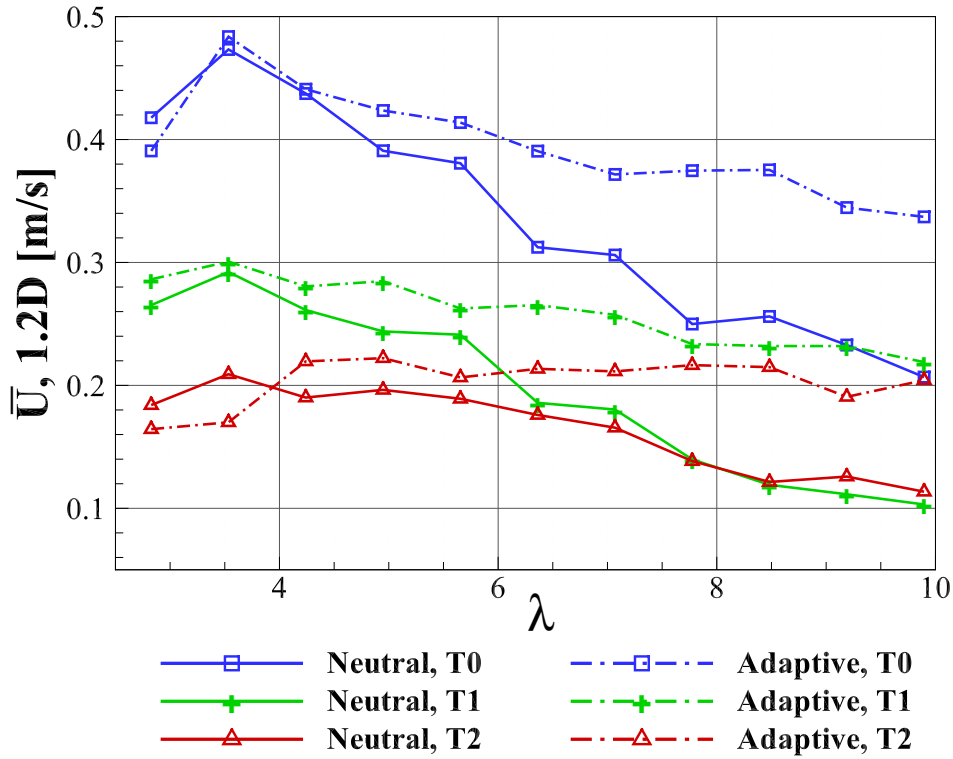
Figure 8.7: Mean hub-height streamwise velocity measured at hub height at 1.2D, aligned with blade tip.

Results of the wake analysis indicate that the use of adaptive blades could add value in this region as well. The capability of the adaptive blade turbine to accelerate the recovery of the mean wake velocity while preventing an increase in turbulence intensity downstream of the turbine introduces the possibility of decreasing the spacing between turbines and could be highly valuable in designing turbine arrays.
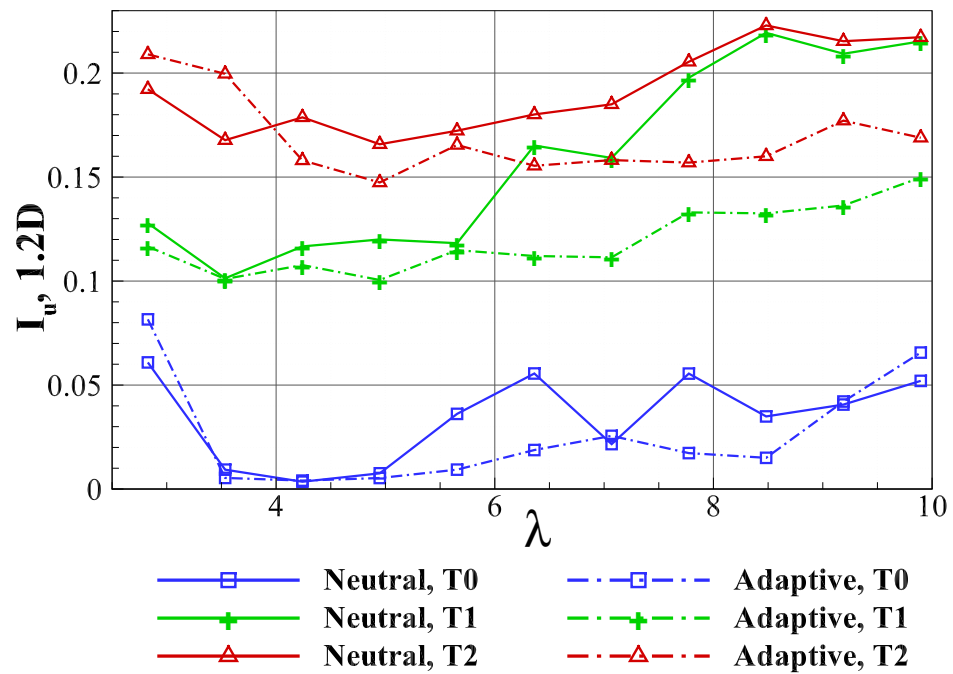
Figure 8.8: Turbulence intensity measured at hub height at 1.2D, aligned with blade tip.

Chapter 9

CONCLUSIONS AND FURTHER DIRECTIONS

The research program presented in this work was undertaken with the goals of developing a numerical strategy to predict the performance and structural response of adaptive composite MHK tidal turbine blades, further exploring the potential of these blades with flume-scale experimental tests, and assessing the potential benefits to be gained with the use of adaptive blades in MHK turbine systems. This chapter will briefly summarize the results and major findings of each research phase, synthesize the knowledge gained, and present directions for future research with the objective of further evolving adaptive blade technology.

9.1 Summary and Major Findings

9.1.1 Numerical Research

The first half of this research was spent developing a numerical strategy for predicting the performance and structural response of adaptive pitch marine turbine blades. A fully coupled 3-D BEM-FEM FSI solver was used to model a two-bladed axial-flow MHK turbine under both steady and cavitating operating conditions; the system was modeled with adaptive pitch to feather, pitch to stall, and non-adaptive composite blades. Each blade design used an equivalent unidirectional fiber angle to facilitate computationally efficient modeling. The load-dependent nature of the adaptive pitch mechanism requires fully dimensional site-specific design; thus, the velocity range and inflow profile used for the fluid modeling was informed by current data from a local tidal energy study collected in Admiralty Inlet in Puget Sound, WA. The predicted performance and structural response of both adaptive blade strategies were compared to the behavior of a non-adaptive composite design; results suggest that numerous advantages can be obtained with the use of adaptive blades in MHK turbines.

Nonuniform Inflow

The adaptive and non-adaptive blade designs were first modeled as operating in a steady, nonuniform inflow profile where boundary layer effects were approximated in order to capture the impact of variable amplitude loading on an MHK turbine blade. The analysis consisted of two sets of three adaptive blades each designed respectively to pitch to feather or pitch to stall in varying degree, which were compared with a non-adaptive reference blade. The blades designed to pitch to feather were shown to increase blade pitch and therefore decrease angle of attack, effectively reducing lift and drag and the corresponding power and thrust coefficients. Conversely, the pitch to stall blades decreased blade pitch and increased angle of attack, increasing lift and drag and therefore power and thrust. An increasing rate of pitch change was observed for the adaptive pitch to stall blades as loading increased, due to the load-dependent nature of the load-capturing pitch to stall mechanism. This self-reinforcing behavior was highlighted as an area of concern due to the possibility of static or dynamic divergence. Conversely, the load-shedding capabilities of the pitch to feather blade design lead to a decreased rate of pitch change at higher inflow velocities. It was noted that the non-adaptive blades also experienced a slight positive pitch change at higher loading conditions, due to the flexibility inherent in the material and the bias of the geometry. This emphasizes the importance of including detailed structural modeling in all marine turbine blade analyses.

The same trends were seen within one rotation of a blade in nonuniform inflow. Loads were found to be largest at the point in rotation closest to the free surface and lowest near the sea floor, corresponding to the nonuniform velocity profile used to model boundary layer effects. Thus, the load-dependent behavior of the adaptive mechanisms caused increased pitch change at the areas of higher velocity relative to the areas of lower velocity, allowing the blades to passively adjust to the incident inflow even within one rotation.

In a structural analysis of the blade designs, the relative thrust on the blades was found to be a good indicator of bending stresses. Bending stresses were found to be higher on the adaptive pitch to stall designs than on the neutral blade, while the pitch to feather blades showed the lowest bending stresses due to the lower thrust on the blades. The orientation

of the maximum stress areas on each blade were found to mirror the dominant fiber angle in the adaptive blades, reflecting the difference in the bending behavior. Conversely, shear stresses were found to be an order of magnitude larger on both the adaptive blade designs compared to the non-adaptive blade. The shear stresses in the pitch to feather and pitch to stall designs were similar in magnitude but opposite in direction, due to the difference in the direction of blade twist induced by the adaptive pitch mechanisms.

A failure analysis examined several of the most common methods of composite analysis to determine the likely modes of failure. The fiber-matrix maximum shear failure mode was found to control over the tensile and compressive modes for both the adaptive blades. This was noted as an important design consideration, as adaptive blades designed to meet structural safety requirements determined for rigid or non-adaptive blades may fail unexpectedly in shear, even in the load-shedding pitch to feather design, if proper consideration for the additional flexibility of the passive pitch mechanism is not taken.

Cavitation

Following the steady nonuniform flow analysis, the onset of cavitation on an MHK turbine blade was studied. The structural response of the blades and the full turbine system under cavitating conditions were investigated. Numerical results suggested that passively adaptive pitch to feather blades can be used both to delay cavitation inception and to reduce cavitation volume over the blade surface. An analysis using a nonuniform inflow representative of the inflow in Admiralty Inlet, WA predicted cavitating conditions at well within the range of normal operating conditions and demonstrated the importance of cavitation analysis and design in MHK turbine development.

After the onset of cavitation, all three blade designs in this study exhibited a similar structural response. A blade at the onset of cavitation will start to experience oscillations in thrust and therefore the resulting deformations. As the cavitation volume increases, stronger fluctuations in the blade displacement are found. A harmonic analysis of each blade reflects this fluttering, showing high-frequency harmonic excitation in a cavitating blade that is not present in an equivalent fully wetted blade. The fluctuations in deformation combined with

the higher mode excitation will increase the rate of fatigue on the system and could lead to unanticipated failures if proper cavitation analysis is not integral to the design process.

Because the structural response to cavitation is identical regardless of material orientation, in order to reduce the negative effects of cavitation it is necessary to design a system that will avoid cavitation over as much of the normal operating range as possible. The benefit found in the passively adaptive pitch to feather blade in this study is in its ability to both delay the onset of cavitation and to maintain a reduced cavity volume after that point, allowing the system a greater amount of time spent operating smoothly and decreasing the exposure to fatigue-inducing oscillations. The results of this research suggest that an adaptive blade, designed carefully for site-specific parameters, could push the onset of cavitating conditions beyond the range of normal operation and effectively avoid the effects of cavitation in all but the most extreme conditions.

9.1.2   Experimental Research

In order to experimentally compare the behavior of the adaptive pitch designs to non-adaptive and rigid blade systems, a series of flume tests were conducted. In these tests, a three-bladed axial-flow hydrokinetic turbine was used to evaluate the effect of various blade designs. Two sets of adaptive composite blades, a pitch to feather and a pitch to stall design, were compared to a non-adaptive composite set and a set of aluminum blades. The non-adaptive composite blades provided a baseline with identical composite fabrication to the adaptive blade designs but no designed material bend-twist coupling, while the aluminum set was assumed to be effectively rigid, allowing further comparison between rigid and flexible blades. Static load-deformation testing was performed on all four blade sets to verify adaptive behavior and develop empirical bend-twist models for each blade design; results of the load-deformation tests showed good agreement with design goals and behavior predictions.

Steady Inflow

To gather baseline data, initial flume tests were performed under steady, uniform flow conditions at the Bamfield Marine Sciences Center flume. In these tests, instantaneous forces and moments were recorded on the turbine system and on one of the three blades during operation at varying rotational speeds and inflow velocities. Combined with the instantaneous fluid velocity measurements, this data was used to quantify blade forces and moments as a function of tip speed ratio as well as overall system performance curves at several inflow velocities.

During dynamic testing of the adaptive turbine systems, the pitch to feather and pitch to stall behaviors seen numerically and under static conditions successfully adjusted the loading on the turbine blades as designed. The results of these tests showed that, in general, the pitch to stall blades experienced increased forces and moments compared to the neutral pitch and aluminum blades. This translated to increased power generation for the pitch to stall design at low dimensional loads, but under higher loading conditions caused excessive out of plane deformation, potential stall, and blade failure. On the opposite side of the spectrum, the pitch to feather systems demonstrated significantly lower blade loads and system thrust, with a relatively small decrease in power capture capabilities. Though an apparent benefit was found in power generation with the load-capturing pitch to stall strategy, such a system would need to be carefully designed in order to avoid flow separation and stall and minimize the risk of failure due to the divergent behavior of the pitch to stall mechanism.

In addition to analyzing blade load and performance, Particle Image Velocimetry (PIV) was used to characterize the wake of the turbine rotor under different tip speed ratios and Reynolds numbers. Overall, the PIV wake characterization of the flow around the rigid and adaptive blade systems supported previous results of the blade loads and performance analyses; the adaptive pitch to stall blade design was seen to capture higher loads than the neutral blades, while the pitch to feather blades shed the excess loading.

Turbulent Inflow

Following the steady inflow tests, an additional flume-scale experimental study was performed at the Tyler flume at the University of Washington. The behavior of the axial-flow hydrokinetic turbine with adaptive pitch to feather blades was compared to the same turbine with non-adaptive composite blades in various states of turbulence. Blade loading, performance, and wake characterization between the two systems were analyzed in order to evaluate the potential benefits of the use of adaptive pitch turbine blades in turbulent flow.

Results indicate that the adaptive pitch mechanism could be employed to reduce the effect of turbulent flow fluctuations on a marine hydrokinetic turbine in several areas. The use of adaptive pitch blades was shown to lead to a reduction in both mean streamwise blade loading and load variation; this is significant to the lifetime robustness of a marine hydrokinetic turbine, as these reductions would lead to improved fatigue behavior and lower extreme loads, increasing structural reliability of the turbine. Additionally, the adaptive blades were able to decrease the impact of flow fluctuations on system performance at turbulent length scales on the order of the blade.

The impact of the adaptive mechanism in the wake region was also considered. Though the spectral content of the wake in each case appeared to be little affected by blade design, the influence of the adaptive pitch mechanism on wake recovery is shown to be highly significant. Wake characterization indicates that the use of adaptive blades could accelerate the recovery of the mean wake velocity while preventing an increase in turbulence intensity downstream of the turbine. This introduces the possibility of decreasing the spacing between turbines and could be highly valuable in formulating turbine arrays.

9.1.3 Conclusions

Throughout this work, numerical and experimental modeling of adaptive pitch MHK blades is undertaken to develop greater insight into the potential benefits to be gained by the use of an adaptive pitch system. The effect of two adaptive pitch strategies on blade and system loading, turbine performance, structural response, and wake recovery is studied and presented. The knowledge gained over the course of this work suggests the following

conclusions.

The adaptive pitch to stall design was shown to have the capability of increasing power generation; however, the possibility of static or dynamic divergence in the load-capturing adaptive mechanism was determined to be detrimental to the structural health and longevity of a hydrokinetic marine turbine blade. Though careful design can be employed to reduce the chances of failure, a pitch to stall adaptive blade will experience not only higher loads and material stresses but also a greater susceptibility to cavitation, leading to increased harmonic excitation in the blades and rotor hub and advanced rates of fatigue. Due to the high level of uncertainty involved in the operation of a hydrokinetic turbine in the harsh marine environment and the difficulty in accessing these turbines for maintenance and repair, the potential gain in power capture possible via the use of a pitch to stall adaptive mechanism is likely not worth the associated risk of increased stresses and fatigue.

Conversely, the pitch to feather adaptive mechanism was shown to provide numerous benefits to a marine hydrokinetic turbine. This blade design was shown to significantly reduce blade loads, system thrust, susceptibility to cavitation, and the impact of flow fluctuations on the blade, turbine system, and wake region. The load-shedding system was able to drastically reduce the thrust on the system while maintaining a power coefficient similar to the non-adaptive designs up to the peak of the performance curve. This ability to shed excess loading while maintaining power production could be a highly desirable characteristic for a marine hydrokinetic turbine blade. Moreover, because of the load-dependent nature of the adaptive mechanism, these designs are less sensitive to changes in force under high loading conditions. Thus, the pitch to feather design strategy is considerably more robust in extreme conditions. Going forward, this research recommends the pitch to feather design as a promising strategy to improve the structural integrity of marine hydrokinetic turbines.

9.2   Future Research Directions

Though the results of this work are promising, additional research will aid in further evolving adaptive blade technology. There are several avenues for future work that would improve the feasibility of adaptive blades for MHK turbines; notably research at the material level, the blade level, and the level of the full turbine system.

On the material level, further study into the details of the adaptive pitch mechanism could be beneficial. Scaling of composite models is notoriously difficult, and scaling of the adaptive mechanism especially will be an important area of research for the development of field- and full-scale turbines. The research presented here focused on equivalent fiber angle models and unidirectional composite spars; however, larger blades will require more complex material layups. Moving from a unidirectional fiber composite to a multi-layer model for both numerical and experimental work will be necessary to evaluate larger-scale blades but will add further complexity to the analysis of those blades. Of high concern are the evolution of stress concentrations and inter-laminar failure modes with increasing length scale. A high-fidelity structural model will be needed to more fully evaluate the potential for fatigue and failure.

Moving to a larger-scale blade will also require a deeper investigation into blade manufacture. The strategy used for the experimental work in this research was necessary to finely control the adaptive behavior of a flume-scale blade, but it is not practical for the higher dimensional loads associated with larger-scale testing. Also on the blade level of future research is the need for a parametric investigation into the interaction between blade geometry and the adaptive pitch mechanism. The geometries used in this work were informed by previous or continuing studies of rigid blades to facilitate comparison; however, a study on the impact of various geometric parameters on the bend-twist coupling of an adaptive mechanism as well as a more thorough exploration into the optimal pitch distribution as a function of inflow velocity could reveal further benefits to be gained from the use of an adaptive pitch blade. With a further focus on geometry should come more complete harmonic analyses of the blades and turbine system as well.

Finally, on the level of the full MHK turbine, a complete control strategy is still needed. Adaptive pitch control is shown here to be a promising improvement to the technology; however, control of the rotational speed of the turbine in this research allowed further benefits to be gained. The addition of a variable speed control scheme to create a fully integrated passive pitch-active speed control system will increase the applicability of the adaptive blades in MHK turbines and play a large part in further evolving adaptive blade technology.

BIBLIOGRAPHY

[1] ABAQUS. *ABAQUS Version 12.3 Documentation.* ABAQUS, Inc., 2012.

[2] Advanced Composites Manufacturing Centre. Composite design and manufacture. `http://www.tech.plym.ac.uk/sme/MATS324/MATS324A4\%20fracture.htm`, 2014.

[3] T.D. Ashwill. Passive load control for large wind turbines. In *51st AIAA/ASME/ASCE/AHS/ASC Structures, Structural Dynamics, and Materials Conference*, April 2010.

[4] A.S. Bahaj, W.M.J. Batten, and G. McCann. Experimental verifications of numerical predictions for the hydrodynamic performance of horizontal axis marine current turbines. *Renewable Energy*, 32:2479–2490, 2007.

[5] A.S. Bahaj and L.E. Myers. Fundamentals applicable to the utilisation of marine current turbines for energy production. *Renewable Energy*, 28:2205–2211, 2003.

[6] R.B. Barber. Passive pitch control in marine hydrokinetic turbine blades. Master's thesis, University of Washington, 2014.

[7] R.B. Barber, C.S. Hill, P. Babuska, M.R. Motley, A. Aliseda, and R. Wiebe. Flume-scale testing of an adaptive pitch marine hydrokinetic turbine. *Composite Structures*, 168:465–473, 2017.

[8] R.B. Barber, C.S. Hill, P.F. Babuska, A. Aliseda, and M.R. Motley. Performance of an adaptive pitch marine hydrokinetic turbine in turbulent inflow. In *12th European Wave and Tidal Energy Conference*, Cork, Ireland, August 2017.

[9] R.B. Barber, C.S. Hill, P.F. Babuska, M. Somoano, R. Wiebe, A. Aliseda, and M.R. Motley. Adaptive pitch marine hydrokinetic turbine blades: Experimental loading, performance, and wake imaging. In *Marine Energy Technology Symposium*, Washington D.C., May 2017.

[10] R.B. Barber, C.S. Hill, P.F. Babuska, R. Wiebe, A. Aliseda, and M.R. Motley. Adaptive composites for load control in marine turbine blades. In *36th International Conference on Ocean, Offshore and Arctic Engineering*, Trondheim, Norway, June 2017.

[11] R.B. Barber and M.R. Motley. A numerical study of the effect of passive control on cavitation for marine hydrokinetic turbines. In *11th European Wave and Tidal Energy Conference*, Nantes, France, September 2015.

[12] R.B. Barber and M.R. Motley. Cavitating response of passively controlled tidal turbines. *Journal of Fluids and Structures*, 66:462–475, 2016.

[13] N. Barltrop, K.S. Varyant, A. Grant, D. Clelland, and X. Pham. Wave-current interactions in marine current turbines. In *Proceedings of the Institution of Mechanical Engineers, Part M: Journal of Engineering for the Maritime Environment*, 2006.

[14] W.M.J. Batten, A.S. Bahaj, A.F. Molland, and J.R. Chaplin. Hydrodynamics of marine current turbines. *Renewable Energy*, 31:249–256, 2006.

[15] W.M.J. Batten, A.S. Bahaj, A.F. Molland, and J.R. Chaplin. Experimentally validated numerical method for the hydrodynamic design of horizontal axis tidal turbines. *Ocean Engineering*, 34:1013–1020, 2007.

[16] W.M.J. Batten, A.S. Bahaj, A.F. Molland, and J.R. Chaplin. The prediction of the hydrodynamic performance of marine current turbines. *Renewable Energy*, 33:1085–1096, 2008.

[17] S.E. Ben Elghali, M.E.H. Benbouzid, and J.F. Charpentier. Marine tidal current electric power generation technology: state of the art and current status. In *Electric Machines & Drives Conference*, pages 1407–1412, 2007.

[18] A. Beyene and J. Peffley. Constructual theory, adaptive motion, and their theoretical application to low-speed turbine design. *Journal of Energy Engineering*, pages 112–118, December 2009.

[19] G.S. Bir, M.J. Lawson, and Y. Li. Structural design of a horizontal-axis tidal current turbine composite blade. In *International Conference on Ocean, Offshore and Arctic Engineering*, June 2011.

[20] T. Blackmore, B. Gaurier, L. Myers, G. Germain, and A.S. Bahaj. The effect of freestream turbulence on tidal turbines. In *European Wave and Tidal Energy Conference*, Nantes, France, September 2015.

[21] T. Blackmore, L. Myers, and A.S. Bahaj. Effects of turbulence on tidal turbines: Implications to performance, blade loads, and condition monitoring. *International Journal of Marine Energy*, 14:1–26, 2016.

[22] J.P. Blasques, C. Berggreen, and P. Andersen. Hydro-elastic analysis and optimization of a composite marine propeller. *Marine Structures*, 23:22–38, 2010.

[23] L.S. Blunden and A.S. Bahaj. Tidal energy resource assessment for tidal stream generators. *Journal of Power and Energy*, 221(2):137–146, 2007.

[24] C. E. Brennen. *Cavitation and Bubble Dynamics*. Oxford University Press, 1995.

[25] I. Bryden and G.T. Melville. Choosing and evaluating sites for tidal current development. *Journal of Power and Energy*, 218, 2004.

[26] I.G. Bryden and S.J. Couch. Me1 - marine energy extraction: tidal resource analysis. *Renewable Energy*, 31:133–139, 2006.

[27] P. Camanho and M. Lambert. A design methodology for mechanically fastened joints in laminated composite materials. *Composites Science and Technology*, 66:3004–3020, 2006.

[28] J.S. Carlton. *Marine Propellers and Propulsion*. Elsevier, 2nd edition, 2007.

[29] L.P. Chamorro, C. Hill, S. Morton, C. Ellis, R.E.A. Arndt, and F. Sotiropoulos. On the interaction between a turbulent open channel flow and an axial-flow turbine. *Journal of Fluid Mechanics*, 716:658–670, 2013.

[30] L.P. Chamorro, C. Hill, V.S. Neary, B. Gunawan, R.E.A. Arndt, and F. Sotiropoulos. Effects of energetic coherent motions on the power and wake of an axial-flow turbine. *Physics of Fluids*, 27:055104, 2015.

[31] B. Chen, S. Neely, T. Michael, S. Gowing, R. Szwerc, D. Buchler, and R. Schult. Design, fabrication and testing of pitch-adapting (flexible) composite propellers. In *The SNAME Propellers/Shafting Symposium '06*, Virginia Beach, VA, 2006.

[32] P. Davies, G. Germain, B. Gaurier, A. Boisseau, and D. Perreux. Evaluation of the durability of composite tidal turbine blades. *Philosophical Transactions of the Royal Society A*, 371(1985), 2013.

[33] W.C. de Goeij, M.J.L. van Tooren, and A. Beukers. Implementation of bending-torsion coupling in the design of a wind-turbine rotor-blade. *Applied Energy*, 63:191–207, 1999.

[34] R.H. Dieck, W.G. Steele, and G. Osolsobe. Test uncertainty. In *ASME PTC 19.1-2005*. American Society of Mechanical Engineers, New York, NY, 2005.

[35] I. Dincer, C.O. Colpan, O. Kizilkan, and M.A. Ezan. *Progress in Clean Energy, Volume 1: Analysis and Modeling*. Springer, 2015.

[36] E. Fernandez-Rodriguez, T.J. Stallard, and P.K. Stansby. Experimental study of extreme thrust on a tidal stream rotor due to turbulent flow and with opposing waves. *Journal of Fluids and Structures*, 51:354–361, 2014.

[37] P.L. Fraenkel. Power from marine currents. *Journal of Power and Energy*, 216, 2002.

[38] P.L. Fraenkel. Marine current turbines: Pioneering the development of marine kinetic energy converters. In *Proceedings of the Institution of Mechanical Engineers, Part A: Journal of Power and Energy*, volume 221, pages 159–169, 2007.

[39] P.P. Friedmann, C. Venkatesan, and K. Yuan. Development of a structural optimization capability for the aeroelastic tailoring of composite rotor blades with straight and swept tips. In *4th AIAA Symposium on Multidisciplinary Analysis and Optimization*, Cleveland, OH, 1992.

[40] R. Ganguli and I. Chopra. Aeroelastic optimization of a composite helicopter rotor. In *4th AIAA Symposium on Multidisciplinary Analysis and Optimization*, Cleveland, OH, 1992.

[41] R. Ganguli and I. Chopra. Aeroelastic tailoring of composite couplings and blade geometry of a helicopter rotor using optimization methods. *Journal of American Helicopter Society*, 42(3):218–228, 1997.

[42] B. Glaz, P. Friedmann, and L. Lu. Helicopter vibration reduction throughout the entire flight envelope using surrogate-based optimization. *Journal of American Helicopter Society*, 54(1):012007, 2009.

[43] S. Gowing, P. Coffin, and C. Dai. Hydrofoil cavitation improvements with elastically coupled composite materials. In *Proceeding of 25th American Towing Tank Conference*, Iowa City, IA, 1998.

[44] L. Greco, S. Leone, C. Testa, F. Salvatore, and S. Mauro. Theoretical and numerical hydromechanics analysis of self-pitching propellers. In *2nd International Symposium on Marine Propulsors*, Hamburg, Germany, June 2011.

[45] D. Griffin. Evaluation of design concepts for adaptive wind turbines, SAND REPORT 2002-2424. Technical report, Sandia National Laboratories, USA, 2002.

[46] D.M. Grogan, S.B. Leen, C.R. Kennedy, and C.M. Ó Brádaigh. Design of composite tidal turbine blades. *Renewable Energy*, 57:151–162, 2013.

[47] D.H. Hammond, M.F. Amateau, and R.A. Queeney. Cavitation erosion performance of fiber reinforced composites. *Journal of Composite Materials*, 27(16):1522–1544, 1993.

[48] C.M. Harwood and Y.L. Young. A physics-based gap-flow model for potential flow solvers. *Ocean Engineering*, 88:578–587, 2014.

[49] Z. Hashin. Failure criteria for unidirectional fiber composites. *Journal of Applied Mechanics*, 47(2):329–334, 1980.

[50] Z. Hashin and A. Rotem. A fatigue failure criterion for fiber reinforced materials. *Journal of Composite Materials*, 7(4):448–464, 1973.

[51] L. He, W. Xu, and S.A. Kinnas. Numerical methods for the prediction of unsteady performance of marine propellers and turbines. In *International Society of Offshore and Polar Engineers Conference*, Maui, HI, June 2011.

[52] P. Jeffcoate, R. Starzmann, B. Elsaesser, S. Scholl, and S. Bischoff. Field measurements of a full scale tidal turbine. *International Journal of Marine Energy*, 2015.

[53] C.H. Jo, D.Y. Kim, S.J. Hwang, and K.H. Lee. Effects of blade deflection on the horizontal axis tidal turbine performance. In *11th European Wave and Tidal Energy Conference*, Nantes, France, September 2015.

[54] N.M. Karaolis, P.J. Mussgrove, and G. Jeronimidis. Active and passive aeroelastic power control using asymmetric fibre reinforced laminates for wind turbine blades. In *10th British Wind Energy Conference*, London, 1988.

[55] J.E. Kerwin. Marine propellers. *Annual Review of Fluid Mechanics*, 18(1):367–403, 1986.

[56] B.S. Kim, S.Y Bae, W.J. Kim, S.L. Lee, and M.K. Kim. A study on the design assessment of a 50kW ocean current turbine using fluid structure interaction analysis. In *26th IAHR Symposium on Hydraulic Machinery and Systems*, 2012.

[57] S.A. Kinnas and N.E. Fine. A numerical nonlinear analysis of the flow around two- and three-dimensional partially cavitating hydrofoils. *Journal of Fluid Mechanics*, 254:151–181, 1993.

[58] S.A. Kinnas, H. Lee, and Y.L. Young. Modeling of unsteady sheet cavitation on marine propeller blades. *International Journal of Rotating Machinery*, 9(4):263–277, 2003.

[59] S.A. Kinnas, W. Xu, Y.-H. Yu, and L. He. Computational methods for the design

and prediction of performance of tidal turbines. *Journal of Offshore Mechanics and Arctic Engineering*, 134(1):011101, 2012.

[60] P. Kumar and R.P. Saini. Study of cavitation in hydro turbines - a review. *Renewable and Sustainable Energy Reviews*, 14:374–383, 2010.

[61] M.J. Lawson, Y. Li, and D.C. Sale. Development and verification of a computational fluid dynamics model of a horizontal-axis tidal current turbine. In *30th International Conference on Ocean, Offshore, and Arctic Engineering*, June 2011.

[62] A.T. Lee and R.G.J. Flay. Compliant blades for passive power control of wind turbines. *Wind Engineering*, 24:3–11, 2000.

[63] H. Lee, M.-C. Song, J.-C. Suh, and B.-J. Chang. Hydro-elastic analysis of marine propellers based on a BEM-FEM coupled FSI algorithm. *International Journal of Naval Architecture and Ocean Engineering*, 6(3):562–577, 2014.

[64] J.H. Lee, S. Park, D.H. Kim, S.H. Rhee, and M.-C. Kim. Computational methods for performance analysis of horizontal axis tidal stream turbines. *Applied Energy*, 98:512–523, 2012.

[65] Y.J. Lee and C.C. Lin. Optimized design of composite propeller. *Mechanics of Advanced Materials and Structures*, 11:17–30, 2004.

[66] C.C. Lin and Y.J. Lee. Stacking sequence optimization of laminated composite structures using genetic algorithm with local improvement. *Composite Structures*, 63:339–345, 2004.

[67] C.C. Lin, Y.J. Lee, and C.S. Hung. Optimization and experiment of composite marine propellers. *Composite Structures*, 89:206–215, 2009.

[68] W. Liu and J. Gong. Adaptive bend-torsional coupling wind turbine blade design imitating the topology structure of natural plant leaves. In Dr. Ibrahim Al-Bahadly, editor, *Wind Turbines*. InTech, 2011.

141

[69] Z. Liu and Y.L. Young. Utilization of bending-twisting coupling effects for performance enhancement of composite marine propellers. *Journal of Fluids and Structures*, 25:1102–1116, 2009.

[70] D.W. Lobitz and P.S. Veers. Aeroelastic behavior of twist-coupled HAWT blades. In *1998 ASME Wind Energy Symposium at 36th AIAA Aerospace Sciences Meeting and Exhibition*, Reno, NV, 1998.

[71] D.W. Lobitz and P.S. Veers. Load mitigation with bending/twist-coupled blades on rotors using modern control strategies. *Wind Energy*, 6:105–117, 2003.

[72] D.W. Lobitz, P.S. Veers, G.R. Eisler, D.J. Laino, P.G. Migliore, and G. Bir. The use of twist-coupled blades to enhance the performance of horizontal axis wind turbines. Technical report, Sandia National Laboratories, 2001.

[73] D.W. Lobitz, P.S. Veers, and P.G. Migliore. Enhanced performance of hawts using adaptive blades. Technical report, Sandia Report 2004, Sandia National Laboratories, 2004.

[74] I. Masters, J.C. Chapman, M.R. Willis, and J.A.C. Orme. A robust blade element momentum theory model for tidal stream turbines including tip and hub loss corrections. *Journal of Marine Engineering & Technology*, 10(1):25–35, 2011.

[75] D.H. Menéndez Arán and S.A. Kinnas. On fully aligned lifting line model for propellers: An assessment of betz condition. *Journal of Ship Research*, 58(3):130–145, 2014.

[76] I.A. Milne, R.N. Sharma, R.G.J. Flay, and S. Bickerton. The role of onset turbulence on tidal turbine blade loads. In *17th Australasian Fluid Mechanics Conference*, 2010.

[77] I.A. Milne, R.N. Sharman, R.G.J.Flay, and S. Bickerton. A preliminary analysis of the effect of the onset flow structure on tidal turbine blade loads, 2010.

[78] M. Mohan. The advantages of composite material in marine renewable energy structures. In *RINA Marine Renewable Energy Conference*, 2008.

[79] A.F. Molland. *Maritime Engineering Reference Book - A Guide to Ship Design, Construction and Operation.* Elsevier, 2008.

[80] A.F. Molland and S.R Turnock. *Marine Rudders and Control Surfaces: Principles, Data, Design and Applications.* Butterworth-Heinemann, 2007.

[81] P.J. Moriarty and A.C. Hansen. *AeroDyn Theory Manual.* National Renewable Energy Laboratory, Golden, Colorado, 2005.

[82] M.R. Motley and R.B. Barber. Passive control of marine hydrokinetic turbine blades. *Composite Structures*, 110:133–139, 2014.

[83] M.R. Motley and R.B. Barber. Passive pitch control of horizontal axis marine hydrokinetic turbine blades. In *33rd International Conference on Ocean, Offshore and Arctic Engineering*, 2014.

[84] M.R. Motley, Z. Liu, and Y.L. Young. Utilizing fluid-structure interactions to improve energy efficiency of composite marine propellers in specially varying wake. *Composite Structures*, 90(3):304–313, 2009.

[85] M.R. Motley and Y.L. Young. Influence of uncertainties on the response and reliability of self-adaptive composite rotors. *Composite Structures*, 94(1):114–120, 2011.

[86] M.R. Motley and Y.L. Young. Performance-based design and analysis of flexible composite propulsors. *Journal of Fluids and Structures*, 27(8):1310–1325, 2011.

[87] M.R. Motley and Y.L. Young. Scaling of the transient hydroelastic response and failure mechanisms of self-adaptive composite marine propellers. *International Journal of Rotating Machinery*, 2012, 2012.

[88] M.R. Motley, Y.L. Young, and Z. Liu. Three-dimensional underwater shock response of composite marine structures. *Journal of Applied Mechanics*, 78:061013, 2011.

[89] R.E. Murray, D.A. Doman, M.J Pegg, T. Nevalainen, K. Gracie, and C.M. Johnstone. Design tool for passively adaptive tidal turbine blades. In *11th European Wave and Tidal Energy Conference*, Nantes, France, September 2015.

[90] R.E. Murray, K. Gracie, D.A. Doman, M.J Pegg, and C.M. Johnstone. Design of a passively adaptive rotor blade for optimized performance of a horizontal-axis tidal turbine. In *10th European Wave and Tidal Energy Conference*, Aalborg, Denmark, September 2013.

[91] R.E. Murray, T. Nevalainen, K. Gracie-Orr, D.A. Doman, M.J. Pegg, and C.M. Johnstone. Passively adaptive tidal turbine blades: Design tool development and initial verification. *International Journal of Marine Energy*, 14:101–124, 2016.

[92] P. Mycek, B. Gaurier, G. Germain, G. Pinon, and E. Rivoalen. Experimental study of the turbulence intensity effects on marine current turbines behaviour. Part I: One single turbine. *Renewable Energy*, 66:729–746, 2014.

[93] R.F. Nicholls-Lee, S.W. Boyd, and S.R. Turnock. Development of high performance composite bend-twist coupled blades for a horizontal axis tidal turbine, 2009.

[94] R.F. Nicholls-Lee, S.W. Boyd, and S.R. Turnock. A method for analyzing fluid structure interactions on a horizontal axis tidal turbine, 2011.

[95] R.F. Nicholls-Lee and S.R. Turnock. The use of computational fluid dynamics in the optimisation of marine current turbines. In *10th Numerical Towing Tank Symposium*, Hamburg, Germany, 2007.

[96] R.F. Nicholls-Lee, S.R. Turnock, and S.W. Boyd. Performance prediction of a free stream tidal turbine with composite bend-twist coupled blades. In *2nd International Conference on Ocean Energy*, October 2008.

[97] R.F. Nicholls-Lee, S.R. Turnock, and S.W. Boyd. Simulation based optimisation of marine current turbine blades. In *7th International Conference on Computer and IT Applications in the Maritime Industries*, Liège, Belgium, 2008.

[98] R.F. Nicholls-Lee, S.R. Turnock, and S.W. Boyd. Application of bend-twist coupled blades for horizontal axis tidal turbines. *Renewable Energy*, 50:541–550, 2013.

144

[99] Northwestern University. Composite materials program. `http://www.tam.northwestern.edu/research/composites.html`.

[100] A.C. Orifici, I. Herszerg, and R.S. Thomson. Review of methodologies for composite material modelling incorporating failure. *Composite Structures*, 86:194–210, 2008.

[101] A.B. Phillips, S.R. Turnock, and M. Furlong. Evaluation of manoeuvring coefficients of a self-propelled ship using blade element momentum propeller model coupled to a reynolds averaged navier stokes flow solver. *Ocean Engineering*, 36:1217–1225, 2009.

[102] B. Polagye and J. Thomson. Tidal energy resource characterization: Methodology and field study in Admiralty Inlet, Puget Sound, US. *Proceedings of the Institution of Mechanical Engineers, Part A: Journal of Power and Energy*, 227(3):352–367, 2013.

[103] D. Sale, A. Aliseda, and M. Motley. Structural optimization of composite blades for wind and hydrokinetic turbines. In *1st Marine Energy Technology Symposium*, April 2013.

[104] O. Soykasap and D.H. Hodges. Performance enhancement of a composite tilt-rotor using aeroelastic tailoring. *Journal of Aircraft*, 37:850–858, 2000.

[105] R. Starzmann, M. Baldus, E. Groh, N. Hirsch, N.A. Lange, and S. Scholl. A stepwise approach towards the development and full-scale testing of a marine hydrokinetic turbine. In *1st Marine Energy Technology Symposium*, Washington, D.C., April 2013.

[106] R. Starzmann, P. Jeffcaote, S. Scholl, S. Bischoff, and B. Elsaesser. Field testing a full-scale tidal turbine. In *11th European Wave and Tidal Energy Conference*, Nantes, France, September 2015.

[107] Strategic Initiative for Ocean Energy. *Ocean energy: State of the art*, 2013.

[108] Strategic Initiative for Ocean Energy. *Ocean energy technology: Gaps and barriers*, 2013.

[109] Strategic Initiative for Ocean Energy. *Wave and tidal energy strategic technology agenda*, 2014.

[110] J. Thomson, B. Polagye, V. Durgesh, and M.C. Richmond. Measurements of turbulence at two tidal energy sites in Puget Sound, WA. *IEEE Journal of Oceanic Engineering*, 37(3):363–374, 2012.

[111] P. Veers, G. Bir, and D. Lobitz. Aeroelastic tailoring in wind-turbine blade applications. In *Windpower '98, American Wind Energy Association Meeting and Exhibition*, Bakersfield, California, 1998.

[112] J. Wang, J. Piechna, and N. Müller. A novel design and preliminary investigation of composite material marine current turbine. *The Archive of Mechanical Engineering*, 58(4):355–366, 2011.

[113] B. Whitby and C.E. Ugalde-Loo. Performance of pitch and stall regulated tidal stream turbines. *IEEE Transactions on Sustainable Energy*, 5(1):64–72, January 2014.

[114] A.L. Winter. Differences in fundamental design drivers for wind and tidal turbines. In *OCEANS, 2011 IEEE*, 2011.

[115] R.J.K. Wood, A.S. Bahaj, S.R. Turnock, L. Wang, and M. Evans. Tribological design constraints of marine renewable energy systems. *Philosophical Transactions of the Royal Society A*, 368:4807–4827, 2010.

[116] T. Yamatogi, H. Murayama, K. Uzawa, K. Kageyama, and N. Watanabe. Study on cavitation erosion of composite materials for marine propeller. In *Proceedings of the Seventeenth International Conference on Composite Materials, ICCM17*, 2009.

[117] Y.L. Young. Time-dependent hydroelastic analysis of cavitating propulsors. *Journal of Fluids and Structures*, 23:269–295, 2007.

[118] Y.L. Young. Fluid-structure interaction analysis of flexible composite marine propellers. *Journal of Fluids and Structures*, 24:799–818, 2008.

[119] Y.L. Young and S.A. Kinnas. A BEM for the prediction of unsteady midchord face and/or back propeller cavitation. *Journal of Fluids Engineering*, 123:311–319, 2001.

[120] Y.L. Young and S.A. Kinnas. Analysis of supercavitating and surface-piercing propeller flows via BEM. *Computational Mechanics*, 32:269–280, 2003.

[121] Y.L. Young and S.A. Kinnas. Numerical modeling of supercavitating propeller flows. *Journal of Ship Research*, 47:48–62, 2003.

[122] Y.L. Young and S.A. Kinnas. Performance prediction of surface-piercing propellers. *Journal of Ship Research*, 28(4):288–305, 2004.

[123] Y.L. Young and Z. Liu. *HE PROPCAV User's manual and documentation*, 2.0 edition, 2008.

[124] Y.L. Young and Z. Liu. Performance prediction of Newton-Rader propellers. *Journal of Ship Research*, 52(2):124–145, 2008.

[125] Y.L. Young, Z. Liu, and M. Motley. Influence of material anisotropy on the hydroelastic behaviors of composite marine propellers. In *ONR NH Symposium on Naval Hydrodynamics*, October 2008.

[126] Y.L. Young, T.J. Michael, M. Seaver, and S.T. Trickey. Numerical and experimental investigations of composite marine propellers. In *26th Symposium on Naval Hydrodynamics*, Rome, Italy, September 2006.

[127] Y.L. Young and M.R. Motley. Influence of material and loading uncertainties on the hydroelastic performance of advanced material propellers. In *Second International Symposium on Marine Propulors*, June 2011.

[128] Y.L. Young, M.R. Motley, R.B. Barber, E.J. Chae, and N. Garg. Adaptive composite marine propulsors and turbines: Progress and challenges. *Applied Mechanics Reviews*, 68(6):060803, 2016.

[129] Y.L. Young, M.R. Motley, and R.W. Yeung. Hydroelastic response of wind or tidal turbines. In *28th International Conference on Ocean, Offshore and Arctic Engineering*, 2009.

[130] Y.L. Young, M.R. Motley, and R.W. Yeung. Three-dimensional numerical modeling of the transient fluid-structure interaction response of tidal turbines. *Journal of Offshore Mechanics and Arctic Engineering*, 132:011101, 2010.